Improvements to the cirrus radiative properties parameterization in the Fu-Liou Radiation Model and an evaluation of its dependence on ice crystal shape

Steven S. Robinson

A thesis
submitted in partial fulfillment of the
requirements for the degree of

Master of Science

University of Washington

2007

Program Authorized to Offer Degree:
Atmospheric Sciences

University of Washington
Graduate School

This is to certify that I have examined this copy of a master's thesis by

Steven S. Robinson

and have found that it is complete and satisfactory in all respects,
and that any and all revisions required by the final
examining committee have been made.

Committee Members:

_____
Qiang Fu

_____
Stephen G. Warren

_____
Thomas P. Ackerman

Date: _____

Signature: _____

Date: _____

TABLE OF CONTENTS

LIST OF FIGURES

LIST OF TABLES

ACKNOWLEDGEMENTS

I wish to thank several people who made this thesis possible:

My advisor, Qiang Fu, for his excellent guidance on this project and radiation theory in general

Our Boeing collaborators, Michael Danilin and Steve Baughcum, for useful discussions and insights that helped guide this work

My thesis committee members, Tom Ackerman and Stephen Warren, for providing helpful feedback on the draft

My past and present officemates Celeste Johanson, Qiong Yang, and Shawn Hollars for many insightful and entertaining conversations that were always a welcome break from research

My family, especially my sister, Jen, and my parents for their constant encouragement and support

CHAPTER 1: INTRODUCTION

It is a well-known fact that the treatment of cirrus clouds can introduce significant uncertainties in global model simulations of the climate system (Liou 1986; Stephens et al. 1990). All cirrus clouds have varying size and shape distributions of ice particles making accurate radiative model calculations difficult (Fu 1996). Yet, even if cirrus cloud composition could be accurately quantified through observations, the computation requirements for explicitly calculating the interaction of radiation with ice particles of various shapes are extremely large. It is for this reason that parameterizations are heavily relied upon in cloud radiative modeling. The biggest challenge in the formation of parameterizations is to capture the crucial physics that provide the foundations of accurate calculations without making the scheme too computationally intensive. The compromise between accuracy and simplicity is one that varies greatly based on the requirements and constraints of a given modeling application. It would therefore be convenient to have a parameterization with multiple levels of complexity, each with a known level of accuracy.

A widely-used cirrus radiative properties parameterization is that developed by Fu (1996) for the solar spectral region and Fu et al. (1998) for the infrared spectral region, both of which assume the presence of randomly-oriented solid hexagonal column ice crystals. Its original purpose was to provide a simple way to parameterize the radiative effects of cirrus clouds that would be insensitive to the assumed ice particle shape. This was achieved by introducing a generalized mean effective size (D_{ge}) along with ice water content (IWC) to represent the ice particle size distributions and provide a basis for the parameterization of the single-scattering properties (SSPs). The ice particle extinction coefficient and single-scattering albedo were theoretically linked to D_{ge} and IWC. However, the solar parameterizations of the asymmetry factor and delta-function transmission in terms of D_{ge} still strongly depended on ice particle shape.

An attempt to mitigate this shape-dependency was made in Fu (2007) by introducing the mean effective aspect ratio as a way to generalize the parameterization of the asymmetry factor and delta-function transmission so that they can be applied to cirrus clouds containing any ice crystal shape. This added much-needed flexibility to the model, but its accuracy is dependent on the aspect ratio of each shape fully defining the shape differences using only these two key SSPs. All other SSP parameterizations are still based on one ice particle shape (i.e., solid hexagonal ice particles) and their accuracy in modeling cirrus with other ice particle shapes is not fully tested. In order to test the accuracy of the Fu (1996), Fu et al. (1998), and Fu (2007) parameterizations in their ability to model cirrus clouds with diverse ice crystal shapes, new parameterizations that explicitly model major ice crystal shapes are needed as a basis of comparison.

Detailed SSP calculations for aggregates, bullet rosettes, hollow hexagonal columns, hexagonal plates, and solid hexagonal columns were developed in Yang et al. (2000) and Yang et al. (2005). In this work, these calculations are used to develop a similar set of parameterizations to those currently used in the Fu-Liou Radiation Model (Fu and Liou 1992, 1993; Fu 1996; Fu et al. 1998; Fu 2007). Through the consideration of two types of cirrus clouds, these new parameterizations are used to evaluate the cirrus radiative forcing accuracy of the current model parameterizations, which are derived from solid hexagonal column shapes.

Chapter 2 reviews the Fu (1996), Fu et al. (1998), and Fu (2007) parameterizations along with recent improvements from Robinson and Fu (2006) that allow the modeling of smaller ice particles. Chapter 3 presents the shape-explicit calculations of SSPs for aggregates, bullet rosettes, hollow hexagonal columns, hexagonal plates, and solid hexagonal columns from Yang et al. (2000) and Yang et al. (2005). It is shown how these calculations were used to form new shape-explicit parameterizations for the Fu-Liou Radiative Transfer Model. The parameterizations themselves are also presented and interpreted. Chapter 4 applies the new parameterizations to two cirrus cloud simulations to evaluate the accuracy of cirrus

radiative forcing calculated using the original and modified model parameterizations when compared to the new shape-explicit parameterizations. Finally, Chapter 5 provides conclusions on the relative accuracy of each set of parameterizations as well as insights into important issues that remain unresolved.

CHAPTER 2: A REVIEW OF THE CIRRUS RADIATIVE PROPERTIES PARAMETERIZATION IN THE FU-LIOU RADIATION MODEL

2.1. Single-scattering properties

Interactions of radiation with particles can be described with single-scattering properties (SSPs) that quantify extinction, scattering or absorption, and the phase function. Extinction is the amount of radiation removed from the incident radiation by scattering plus absorption as it travels through a particle. Its most general form is the extinction efficiency, Q_e, or the fraction of the geometric cross-sectional area of energy removed from the incident radiation. It can also be expressed as the extinction cross-section, σ_e, the cross-sectional area of energy removed from the incident radiation or as an extinction coefficient, β_e, the cross-section per unit volume of energy removed from the incident radiation. An increase in extinction means an increase in the amount of incident radiation that is scattered or absorbed by a particle.

Along with extinction, either scattering or absorption must be quantified. The probability of scattering can be described by the single-scattering albedo, $\tilde{\omega}$, or the fraction of radiation scattered compared to the radiation extincted. A $\tilde{\omega}$ value of 1 denotes a particle only scattering radiation and 0 is a purely absorbing particle. It can be represented in several forms:

$$\tilde{\omega} = \text{Scattering} / \text{Extinction} \qquad [2.1]$$

$$\text{Co-albedo} = 1 - \tilde{\omega} \qquad [2.2]$$

$$\text{Absorption} = (\text{Co-albedo}) * \text{Extinction} \qquad [2.3]$$

Scattering is the dominant mechanism of extinction in the solar spectral region, while neither scattering nor absorption is dominant in the infrared region. Single-scattering albedo is typically used to quantify the transfer of solar radiation, while an absorption quantity is typically used to quantify the transfer of infrared radiation.

The phase function quantifies the probability distribution of scattering angle of radiation that is incident to a particle. A common approximation of the phase function is the use of the first moment of the Legendre polynomial expansion of the phase

function. This is known as the asymmetry factor, g, where (1+g)/2 represents the total fraction of incident radiation that is scattered in the forward direction by the particle. A value of 1 means that all radiation is scattered by the particle in the same direction as the incident radiation, while a value of 0 means that all radiation interacting with the particle is scattered equally in the forward and backward directions. The asymmetry factor is highly dependent on particle shape, which will be demonstrated in subsequent chapters.

The phase function often has a strong peak of forward scattered radiation. When the phase function is approximated, especially with just its first moment, this peak is not taken into account. In order to mitigate this inaccuracy, the forward peak can be truncated and that fraction of radiation can be considered to be transmitted in the forward direction. The forward peak can be defined as

$$f = \frac{1}{2\tilde{\omega}} + f_{\delta} \qquad [2.4]$$

where the first term is the forward scattered radiation due to diffraction and the second term is the delta-function transmission, or the forward scattered radiation due to reflection and refraction. By using the asymmetry factor along with the delta-function transmission diffracted fraction, the radiative transfer calculations become more accurate than if asymmetry factor is used alone. The delta-function transmission is directly related to particle shape and smoothness. Smooth particles will allow more radiation to be scattered in the forward direction, which increases the quantity. Rough particles cause the opposite effect and a very rough particle may not require the delta-function transmission for accurate results.

2.2. Single-scattering properties parameterization

The cirrus solar parameterization, outlined in Fu (1996), assumes randomly-oriented solid hexagonal columns ranging in size from 8.75 to 3,100 μm. The extinction coefficient, single-scattering albedo, asymmetry factor, and delta-function transmission are parameterized as functions of mean particle size or mean particle size

and ice water content of the cloud. Reference calculations of extinction efficiency and single-scattering albedo were calculated using the conventional geometric ray-tracing technique for size parameters larger than 200 and the improved geometric ray-tracing technique for all other size parameters. The asymmetry factor and delta-function transmission were calculated using the conventional technique. The size parameter is a dimensionless quantity that defines the ratio of the circumference of a particle to the wavelength of incident radiation

$$x = 2\pi r / \lambda \qquad [2.5]$$

where r is the equivalent spherical particle radius and λ is the radiation wavelength. It is useful for quantifying the effect of scattering on particle size and it is used above as a cutoff point above which the calculation can be deemed accurate.

The cirrus infrared parameterization, outlined in Fu et al. (1998), assumes randomly-oriented solid hexagonal columns ranging in size from 2 to 3,100 μm. The extinction coefficient, absorption coefficient, and asymmetry factor are parameterized as functions of mean particle size or mean particle size and ice water content of the cloud. An accurate method for calculating the SSPs is the finite difference time domain (FDTD), but it is too computationally-intensive to run for particles with large size parameters. It can, however, be used for particles with small size parameters. Geometric ray tracing is only accurate for large size parameters. Composite methods were defined using empirical combinations of Mie, anomalous diffraction theory (ADT), and the geometric optics method (GOM) calculations to interpolate results between the FDTD and geometric ray tracing calculations. The extinction efficiency was calculated using the mean of the ADT and Mie volume and projected area-equivalent spheres results. Absorption efficiency was calculated with a linear combination of the GOM and Mie volume and/or projected area-equivalent spheres results. The asymmetry factor was calculated with Mie volume-equivalent spheres for size parameters less than 10 and with the GOM for all other size parameters.

The preceding parameterizations are not a function of single particle sizes, but rather a mean effective size based on a distribution of particle sizes. A total of 28

observed size distributions, both from tropical and midlatitude origins were used to calculate a collection of physically-based effective sizes of ice particles (Fu 1996). This quantity is known as the generalized effective size (D_{ge}). The density of ice within these size distributions can also be quantified. This quantity is known as the ice water content (IWC). These parameters are shown below

$$D_{ge} = \frac{2\sqrt{3}}{3} \frac{\int_{L_{min}}^{L_{max}} V(L)n(L)\, dL}{\int_{L_{min}}^{L_{max}} P(L)n(L)\, dL} \qquad [2.6]$$

$$IWC = \rho_i \int_{L_{min}}^{L_{max}} V(L)n(L)\, dL \qquad [2.7]$$

where V is the particle volume, P is the particle projected area, L is the maximum particle length, n is the particle size distribution, and ρ_i is the ice density. D_{ge} and IWC form the basis of the parameterization definition. By establishing a physical relationship between these quantities and the SSPs, parameterizations were developed in Fu (1996).

The solid hexagonal projected area and volume are given as

$$P = \frac{3}{4} D \left[\frac{\sqrt{3}}{4} D + L \right] \qquad [2.8]$$

$$V = \frac{3\sqrt{3}}{8} D^2 L \qquad [2.9]$$

where D is the particle diameter. Using the expressions for D_{ge} and IWC (Equations [2.6] and [2.7]), D_{ge} can equivalently be expressed as

$$D_{ge} = \frac{2\sqrt{3}}{3\rho_i} \frac{IWC}{A_c} \qquad [2.10]$$

where $A_c = \beta_e/Q_e$ is the total projected area of ice particles per volume. In the geometric optics limit (size parameter >> 1), Q_e is 2. Thus, $\beta_e = 2A_c$. By substituting

A_c into Equation [2.10] and solving for β_e, the following relationship between it and D_{ge} and IWC is formed:

$$\beta_e = \frac{4\sqrt{3}}{3\rho_i}\frac{IWC}{D_{ge}} \quad [2.11]$$

The single-scattering co-albedo for the particle distribution is defined as

$$1-\tilde{\omega} = \frac{\beta_a}{\beta_e} \quad [2.12]$$

where the absorption coefficient, β_a, is defined in terms of the absorption cross-section:

$$\beta_a = \int_{L_{\min}}^{L_{\max}} \sigma_a(L) n(L)\, dL \quad [2.13]$$

At the weak absorption limit, the absorption cross-section is defined as

$$\sigma_a = \frac{4\pi m_i(\lambda)}{\lambda} V(L) \quad \text{(weak absorption limit)} \quad [2.14]$$

where m_i is the imaginary part of the refractive index. At the strong absorption limit, the absorption is defined as:

$$\sigma_a = P(L) \quad \text{(strong absorption limit)} \quad [2.15]$$

In order to derive a relationship between the single-scattering co-albedo and D_{ge} and IWC under the geometric optics limit, Equations [2.11], [2.6], and [2.7] are substituted into Equation [2.12] along with Equation [2.14] for the weak absorption limit and [2.15] for the strong absorption limit. These relationships are shown below:

$$\begin{aligned} 1-\tilde{\omega} &= \frac{\pi\sqrt{3}}{\lambda} m_i D_{ge} \quad \text{(weak absorption limit)} \\ 1-\tilde{\omega} &= \frac{1}{2} \quad \text{(strong absorption limit)} \end{aligned} \quad [2.16]$$

Based on these theoretical relationships, the extinction coefficient is parameterized as a function of D_{ge} and IWC and the single-scattering co-albedo, $1-\tilde{\omega}$, is parameterized as a function of D_{ge}. The asymmetry factor, g, and delta-function transmission, f_δ, were also parameterized as a function of D_{ge}, although there was no

theoretical basis to do so. This is addressed in later improvements to the g and f_δ parameterizations. Since Equations [2.11] and [2.16] are independent of ice particle shape, it is believed that the parameterization of the extinction coefficient and the single-scattering albedo in terms of IWC and D_{ge} can be properly applied to cirrus clouds that contain various nonspherical particles (Fu 1996; Fu et al. 1998).

The extinction, β_e, and absorption, β_a, coefficients, both functions of wavelength, λ, are calculated from the extinction, Q_e, and absorption, Q_a, efficiencies in the following forms:

$$\beta_e(\lambda) = \int_{L_{\min}}^{L_{\max}} Q_e(L,\lambda) P(L) n(L)\, dL \qquad [2.17]$$

$$\beta_a(\lambda) = \int_{L_{\min}}^{L_{\max}} Q_a(L,\lambda) P(L) n(L)\, dL \qquad [2.18]$$

The single-scattering albedo for a single particle can be calculated from the extinction and scattering efficiencies

$$\tilde{\omega}(L,\lambda) = \frac{Q_s(L,\lambda)}{Q_e(L,\lambda)} \qquad [2.19]$$

where $Q_s = Q_e - Q_a$. It, along with the asymmetry factor and the delta-function transmission, are averaged over all particles sizes, weighted against the extinction or scattering efficiency, particle projected area, and the particle size distributions as

$$X(\lambda) = \frac{\int_{L_{\min}}^{L_{\max}} X(L,\lambda) Q_x(L,\lambda) P(L) n(L)\, dL}{\int_{L_{\min}}^{L_{\max}} Q_x(L,\lambda) P(L) n(L)\, dL} \qquad [2.20]$$

where X equals $\tilde{\omega}$, g, or f_δ and Q_x equals Q_e for $\tilde{\omega}$ and Q_s for g and f_δ.

All SSPs explained thus far have been a function of single wavelength values. However, in order to use them as a parameterization in the Fu-Liou Radiation Model, the SSPs within each band limit must be averaged in order to form SSP parameterizations for 18 spectral bands used in the model. There are 6 solar spectrum

bands with wavelengths ranging from 0.25 to 4.00 μm and 12 infrared spectrum bands with wavelengths ranging from 4.55 to 99.9 μm. The band limits are shown in Table 2.1. Solar band means are weighted by solar irradiance and infrared band means are weighted by the Planck function at a temperature of -40 °C, a typical temperature of cirrus clouds. The mathematical representation of the band means for the extinction and absorption coefficients is shown below

$$\overline{Y} = \frac{\int_{\lambda_{min}}^{\lambda_{max}} Y(\lambda) S(\lambda)\, d\lambda}{\int_{\lambda_{min}}^{\lambda_{max}} S(\lambda)\, d\lambda} \qquad [2.21]$$

where Y equals β_e or β_a and $S(\lambda)$ is the solar irradiance or the Planck function, depending on whether it is a solar or infrared band mean. The band mean of the

Table 2.1: Cirrus parameterization band limits for the Fu-Liou Radiation Model
Spectral band limits for the cirrus parameterization in the Fu-Liou Radiation Model. Bands 1-6 are in terms of wavelength (μm) and bands 7-18 are in terms of wavelength (μm) and wavenumber (cm^{-1}), which is the inverse of wavelength.

Band #	Spectral Interval
1	0.25 - 0.70 μm
2	0.70 - 1.41 μm
3	1.41 - 1.90 μm
4	1.90 - 2.50 μm
5	2.50 - 3.50 μm
6	3.50 - 4.00 μm
7	4.55 - 5.26 μm (2200 - 1900 cm^{-1})
8	5.26 - 5.88 μm (1900 - 1700 cm^{-1})
9	5.88 - 7.14 μm (1700 - 1400 cm^{-1})
10	7.14 - 8.00 μm (1400 - 1250 cm^{-1})
11	8.00 - 9.09 μm (1250 - 1100 cm^{-1})
12	9.09 - 10.2 μm (1100 - 980 cm^{-1})
13	10.2 - 12.5 μm (980 - 800 cm^{-1})
14	12.5 - 14.9 μm (800 - 670 cm^{-1})
15	14.9 - 18.5 μm (670 - 540 cm^{-1})
16	18.5 - 25.0 μm (540 - 400 cm^{-1})
17	25.0 - 35.7 μm (400 - 280 cm^{-1})
18	35.7 - 99.9 μm (280 - 100 cm^{-1})

single-scattering albedo is additionally weighted against the extinction coefficient, as shown below:

$$\bar{\tilde{\omega}} = \frac{\int_{\lambda_{\min}}^{\lambda_{\max}} \tilde{\omega}(\lambda)\beta_e(\lambda)S(\lambda)\, d\lambda}{\int_{\lambda_{\min}}^{\lambda_{\max}} \beta_e(\lambda)S(\lambda)\, d\lambda} \qquad [2.22]$$

For the spectral intervals 1.41-1.53-1.64-2.13-2.38, a composite of the linear band mean in Equation [2.22] and a nonlinear band mean following Fu (1996)

$$\bar{\tilde{\omega}}_{NL} = 1 - \frac{1}{\bar{\beta}_e} \exp\left\{ \frac{\int_{\lambda_{\min}}^{\lambda_{\max}} S(\lambda) \ln[(1-\omega(\lambda))\beta_e(\lambda)]\, d\lambda}{\int_{\lambda_{\min}}^{\lambda_{\max}} S(\lambda)\, d\lambda} \right\} \qquad [2.23]$$

are averaged to create a modified band mean calculation shown below:

$$\bar{\tilde{\omega}}_c = \frac{1}{2}[\bar{\tilde{\omega}} + \bar{\tilde{\omega}}_{NL}] \qquad [2.24]$$

The asymmetry factor and delta-function transmission band means are calculated in the same manner as Equation [2.22], except they are weighted against scattering instead of extinction

$$\bar{Z} = \frac{\int_{\lambda_{\min}}^{\lambda_{\max}} Z(\lambda)\beta_s(\lambda)S(\lambda)\, d\lambda}{\int_{\lambda_{\min}}^{\lambda_{\max}} \beta_s(\lambda)S(\lambda)\, d\lambda} \qquad [2.25]$$

where Z equals g or f_δ, β_s is the scattering coefficient, and again $S(\lambda)$ is the solar irradiance or the Planck function, depending on whether it is a solar or infrared band mean. Once the band means are performed, there are 28 data points per SSP for each band, one from each of the size distributions. These can be fit to polynomials to create parameterizations as a function of D_{ge} or D_{ge} and IWC as follows

$$\frac{\beta_e D_{ge}}{IWC} = a_0 D_{ge} + a_1 \qquad [2.26]$$

$$1-\tilde{\omega}=b_0+b_1D_{ge}+b_2D_{ge}^2+b_3D_{ge}^3 \quad [2.27]$$

$$g=c_0+c_1D_{ge}+c_2D_{ge}^2+c_3D_{ge}^3 \quad [2.28]$$

$$f_\delta=d_0+d_1D_{ge}+d_2D_{ge}^2+d_3D_{ge}^3 \quad [2.29]$$

$$\frac{\beta_e D_{ge}}{IWC}=a_0D_{ge}+a_1+\frac{a_2}{D_{ge}} \quad [2.30]$$

$$\frac{\beta_a D_{ge}}{IWC}=b_0+b_1D_{ge}+b_2D_{ge}^2+b_3D_{ge}^3 \quad [2.31]$$

$$g=c_0+c_1D_{ge}+c_2D_{ge}^2+c_3D_{ge}^3 \quad [2.32]$$

where a, b, c, and d are the regression coefficients. Equations [2.26], [2.27], [2.28], and [2.29] are the regression equations for the solar bands and Equations [2.30], [2.31] , and [2.32] are the regression equations for infrared bands.

2.3. Improvement of the asymmetry factor and delta-function transmission parameterizations

It has been substantiated in Fu (2007) that the asymmetry factor and the delta-function transmission are more suitably related to the ice particle aspect ratio. For this reason, these two SSPs have been parameterized as a function of the mean effective aspect ratio

$$AR=\frac{\int_{L_{\min}}^{L_{\max}}\frac{D}{L'}P(L)n(L)\,dL}{\int_{L_{\min}}^{L_{\max}}P(L)n(L)\,dL} \quad [2.33]$$

where L' is the particle length, not to be confused with the maximum particle dimension, L. Fu 2007 shows that the dependence of g on L is largely through the dependence of $\tilde{\omega}$ on L. To isolate this dependency, the fraction of diffracted rays, $1/(2\tilde{\omega})$, is separated from the total asymmetry factor as follows

$$g=\frac{1}{2\tilde{\omega}}+\left(1-\frac{1}{2\tilde{\omega}}\right)g'=\frac{1-g'}{2\tilde{\omega}}+g' \quad [2.34]$$

where g' is the asymmetry factor associated with geometric reflection and refraction. The g' value was parameterized for two different aspect ratio domains and for smooth and rough particles. For $0.1 \le AR \le 1.0$, g' is parameterized in the form

$$g'_s = c_{s0} + c_{s1}AR + c_{s2}AR^2 \quad [2.35]$$

$$g'_r = c_{r0} + c_{r1}AR + c_{r2}AR^2 \quad [2.36]$$

where Equation [2.35] is for smooth particles and Equation [2.36] is for rough particles. For $1.0 \le AR \le 20$, g' is parameterized as

$$g'_s = p_{s0} + p_{s1}\ln(AR) + p_{s2}\ln^2(AR) \quad [2.37]$$

$$g'_r = p_{r0} + p_{r1}\ln(AR) + p_{r2}\ln^2(AR) \quad [2.38]$$

where Equation [2.37] is for smooth particles and Equation [2.38] is for rough particles. The g' parameterizations are then related back to the total asymmetry factor by Equation [2.34]. The delta-function transmission for smooth particles is parameterized for $0.1 \le AR \le 1.0$ by:

$$\begin{aligned} f_\delta &= d_{c0}(\Upsilon(AR))\exp(d_{c1}D_{ge}) \\ \Upsilon(AR) &= 4.844102\text{E-}2AR^2 - 1.156668\text{E-}1AR + 1.886680\text{E-}1 \end{aligned} \quad [2.39]$$

and for $1.0 \le AR \le 20$ by:

$$\begin{aligned} f_\delta &= d_{p0}[\Psi(AR)]\exp(d_{p1}D_{ge}) \\ \Psi(AR) &= -1.650551\text{E-}4\ln^2(AR) + 9.739614\text{E-}2\ln(AR) + 1.060183\text{E-}1 \end{aligned} \quad [2.40]$$

For rough particles, f_δ is assumed to be zero, which is a reasonable approximation since the forward scattering peak in the phase function due to reflection and refraction is small.

2.4. Parameterization of cirrus infrared radiative properties for small ice particles

The cirrus infrared radiative properties parameterization developed by Fu et al. (1998) can only be applied to cirrus with D_{ge} larger than about 10 μm. It is possible to extend the solar parameterization down to smaller D_{ge} values with minimal issues

involving nonphysical values. However, this is not the case for the infrared parameterization.

In Robinson and Fu (2006), a small D_{ge} parameterization was developed as an augmentation to the existing infrared parameterization in order to more effectively model radiative forcing of contrail cirrus and tropical tropopause subvisible cirrus, which have small D_{ge}. Using the Fu (1996) particle geometry and particle size range of 2 to 3,100 μm, small D_{ge} values cannot be produced. Small D_{ge} values were approximated by assuming smaller upper limits on L, with the understanding that as the upper limit on L decreases, so too does the calculated D_{ge}. Instead of the standard infrared size range of 2 to 3,100 μm (38 bins), the upper limit was truncated to 37.5 μm (10 bins), 25 μm (9 bins), 20 μm (8 bins), 16 μm (7 bins), 12 μm (6 bins), 10 μm (5 bins), 8 μm (4 bins), 6 μm (3 bins), 4 μm (2 bins), and 2 μm (1 bin) in order to produce several sets of small D_{ge} values. The SSPs were then calculated using each set of approximated D_{ge} values in the same manner as outlined in Fu et al. (1998). The regression equations used for the small D_{ge} parameterizations are shown below:

$$\beta_e = \frac{IWC}{D_{ge}}(a_0 + a_1 D_{ge} + a_2 D_{ge}^2 + a_3 D_{ge}^3 + a_4 D_{ge}^4) \quad [2.41]$$

$$\beta_a = \frac{IWC}{D_{ge}}(b_0 + b_1 D_{ge} + b_2 D_{ge}^2 + b_3 D_{ge}^3 + b_4 D_{ge}^4) \quad [2.42]$$

$$g = c_0 + c_1 D_{ge} + c_2 D_{ge}^2 + c_3 D_{ge}^3 + c_4 D_{ge}^4 \quad [2.43]$$

The regression coefficients are given in Table A.1 through Table A.3 in Appendix A.

2.5. Discussion

Fu (1996) demonstrated that the extinction and absorption coefficients are functions of D_{ge} and IWC, while the single-scattering co-albedo is a function of D_{ge}. Fu (2007) has shown that the asymmetry factor and delta-function transmission have a significant dependency on AR. Parameterizations based on these relationships should, theoretically speaking, not depend on ice particle shape. An ice particle distribution

with one particular shape would have different D_{ge}, IWC, and AR values, but once these values are determined for a particular shape distribution and inputted into the parameterization, they should produce accurate cirrus radiative budget results for that shape. It is for this reason that these parameterizations are considered generalized for all particle shapes. However, this assertion has not been fully tested. It is possible that other shape dependencies exist that are not taken into account by the current parameterization configurations. The accuracy of cirrus radiative budget calculations performed by the Fu (1996), Fu et al. (1998), and Fu (2007) parameterizations will be tested against calculations by new parameterizations based on Yang et al. (2000) and Yang et al. (2005) that explicitly model major ice crystal shapes.

CHAPTER 3: DEVELOPMENT OF A CIRRUS RADIATIVE PROPERTIES PARAMETERIZATION WITH EXPLICIT CONSIDERATION OF ICE PARTICLE SHAPE

3.1. Development of the parameterizations

In order to test the accuracy of the Fu (1996), Fu et al. (1998), and Fu (2007) parameterizations of cirrus radiative properties when applying to cirrus with different ice particle shapes, we develop parameterizations that explicitly consider the SSPs of aggregate, bullet rosette, hollow hexagonal column, hexagonal plate, and solid hexagonal column ice crystal shapes.

We use the SSPs derived for these shapes from Yang et al. (2000) for solar wavelengths and from Yang et al. (2005) for infrared wavelengths. The authors used the same methods for calculating the SSPs that were employed in Fu (1996) and Fu et al. (1998). These SSPs were also calculated over similar particle size ranges. It is therefore possible to calculate the cirrus SSP parameterizations using the same set of 28 size distributions and parameterize them using the same regression equations (i.e., Equations [2.26]-[2.32]). The differences between these parameterizations compared to those in Fu (1996) and Fu et al. (1998) should be largely due to the differences in the simulated ice particle shape. Small D_{ge} versions of the parameterizations were also developed for all infrared SSPs by Equations [2.41]-[2.43] for each ice particle shape. The resulting solar and infrared parameterization coefficients, including those for the small D_{ge} parameterizations, are presented in Table B.1 through Table B.10 in Appendix B.

The reference calculations and parameterizations of the SSPs for cirrus clouds using different ice particle shapes are shown as a function of D_{ge} for all 18 Fu-Liou Radiation Model spectral bands in Figure 3.1 through Figure 3.18. Figure 3.1 through Figure 3.6 show all four solar SSPs, extinction coefficient*IWC/D_{ge}, single-scattering co-albedo, asymmetry factor, and delta-function transmission, for each of 6 spectral bands with wavelengths ranging from 0.25 to 4.00 μm. The parameterizations from

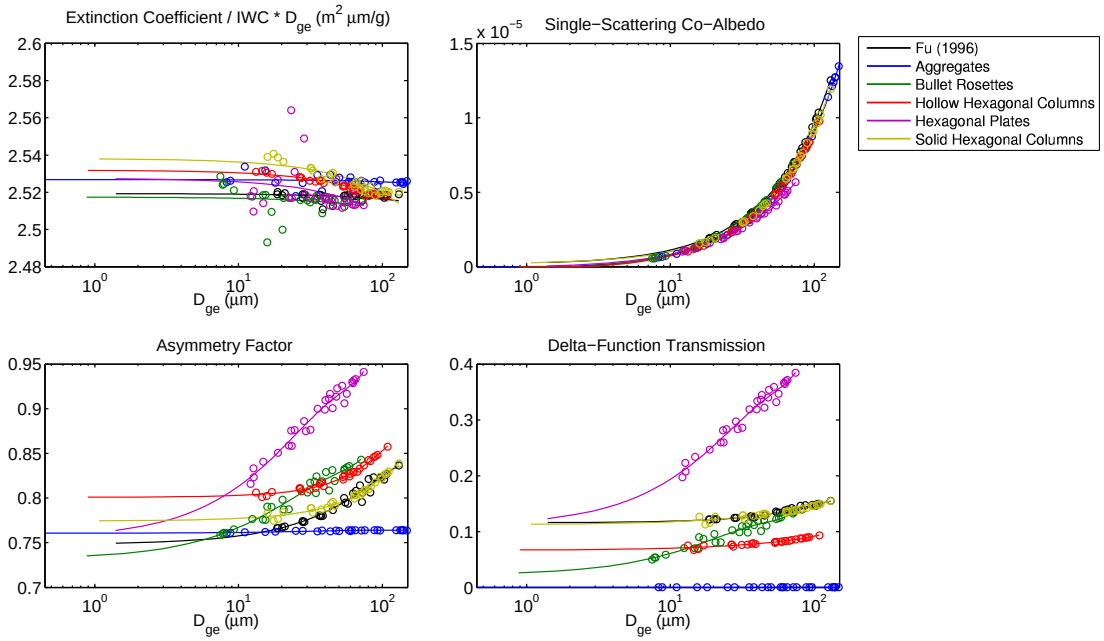

Figure 3.1: Band 1 parameterizations
Reference calculations (circles) and parameterizations (solid lines) of the cirrus single-scattering properties in Band 1 (0.25 - 0.70 µm) for each ice particle shape as a function of the generalized effective size (D_{ge}). The reference calculations and parameterizations from Fu (1996) are shown for comparison purposes.

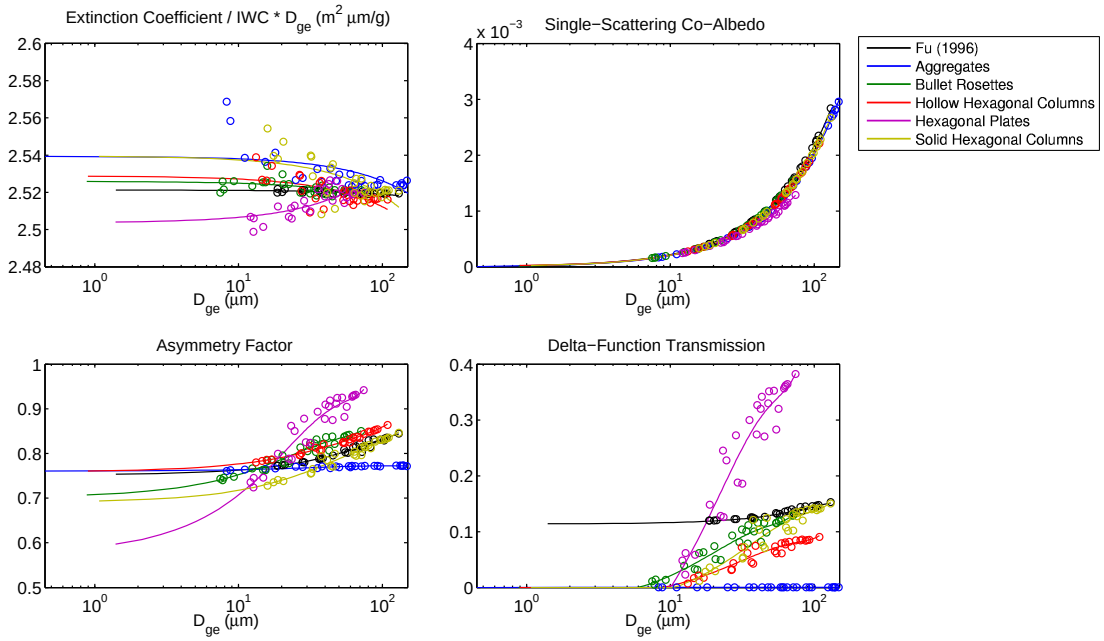

Figure 3.2: Band 2 parameterizations
Same as Figure 3.1, except for Band 2 (0.70 - 1.41 µm).

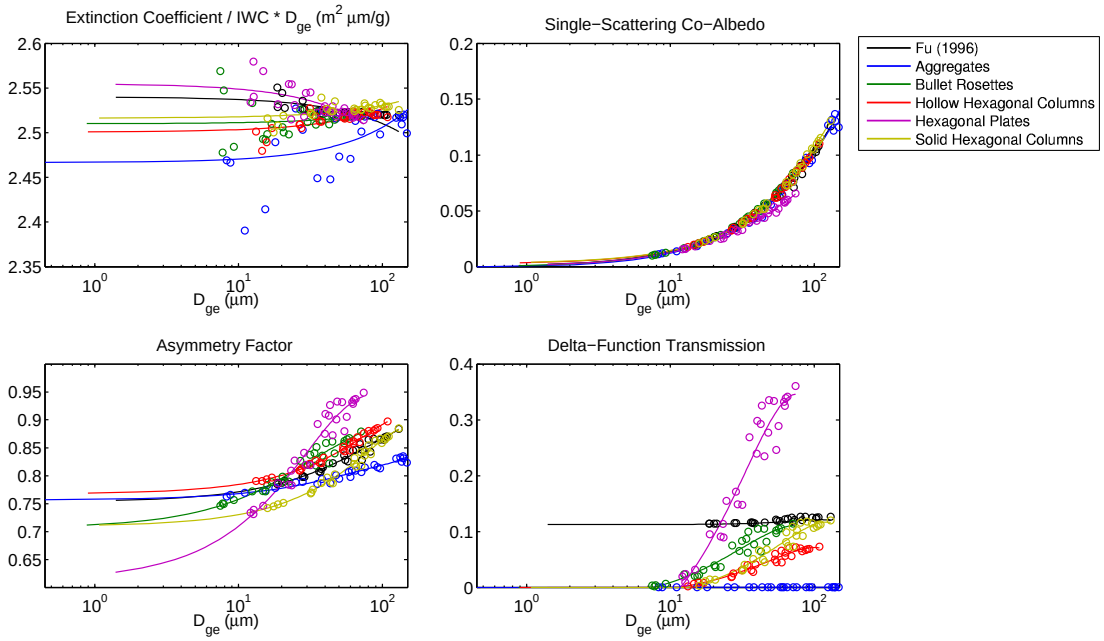

Figure 3.3: Band 3 parameterizations
Same as Figure 3.1, except for Band 3 (1.41 - 1.90 µm).

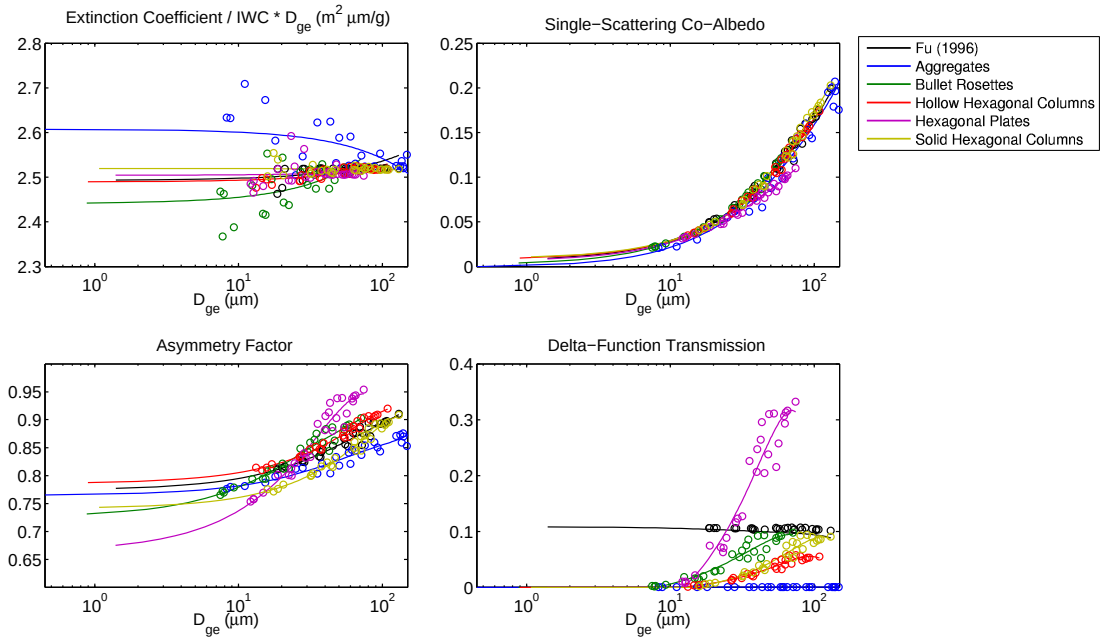

Figure 3.4: Band 4 parameterizations
Same as Figure 3.1, except for Band 4 (1.90 - 2.50 µm).

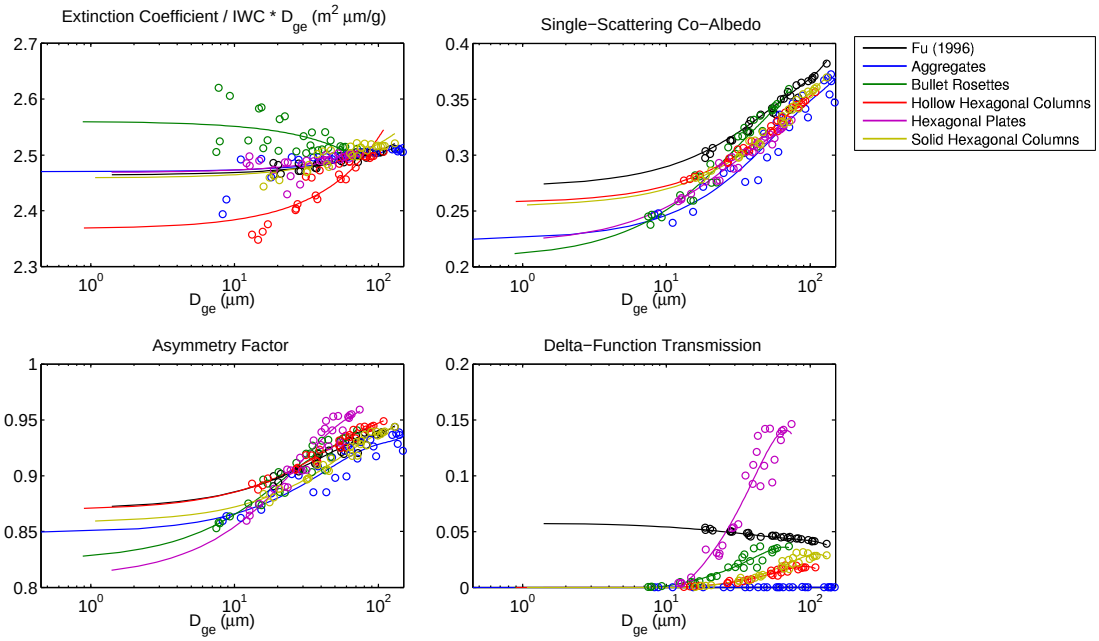

Figure 3.5: Band 5 parameterizations
Same as Figure 3.1, except for Band 5 (2.50 - 3.50 µm).

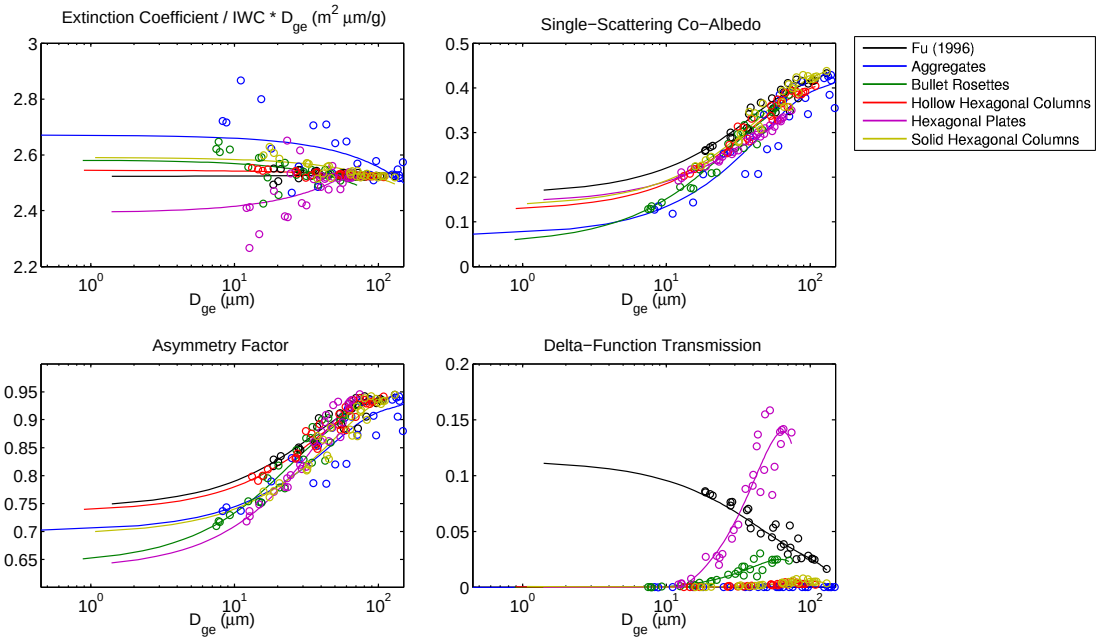

Figure 3.6: Band 6 parameterizations
Same as Figure 3.1, except for Band 6 (3.50 - 4.00 µm).

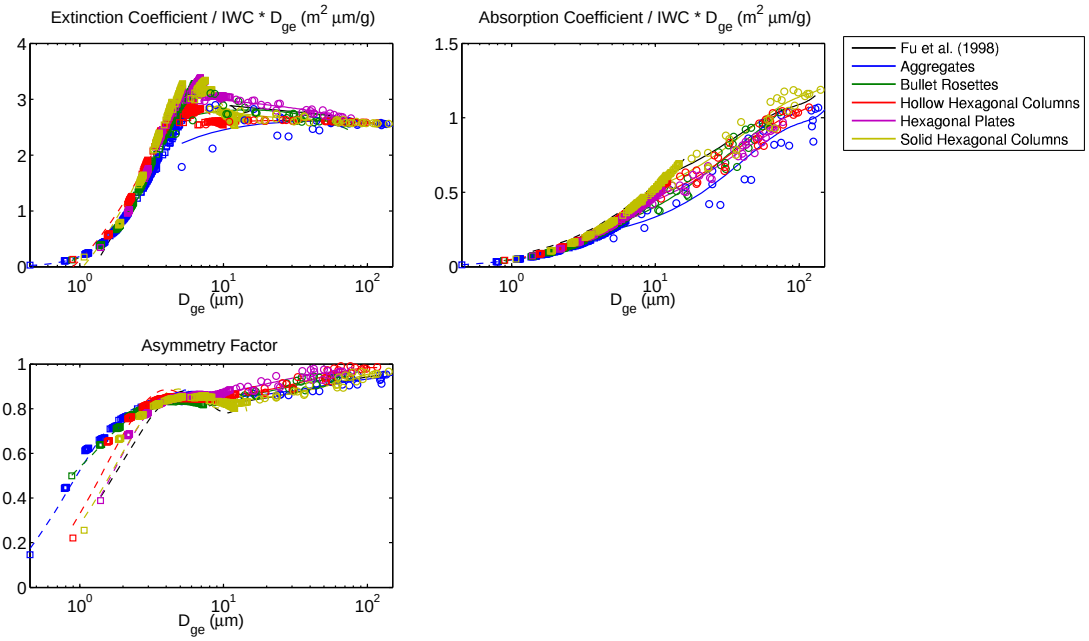

Figure 3.7: Band 7 parameterizations
Reference calculations (circles) and parameterizations (solid lines) of the cirrus single-scattering properties in Band 7 (4.55 - 5.26 µm) for each ice particle shape as a function of the generalized effective size (D_{ge}). The small D_{ge} reference calculations (squares) and parameterizations (dashed lines) are also shown. The parameterizations from Fu et al. (1998) are shown for comparison purposes.

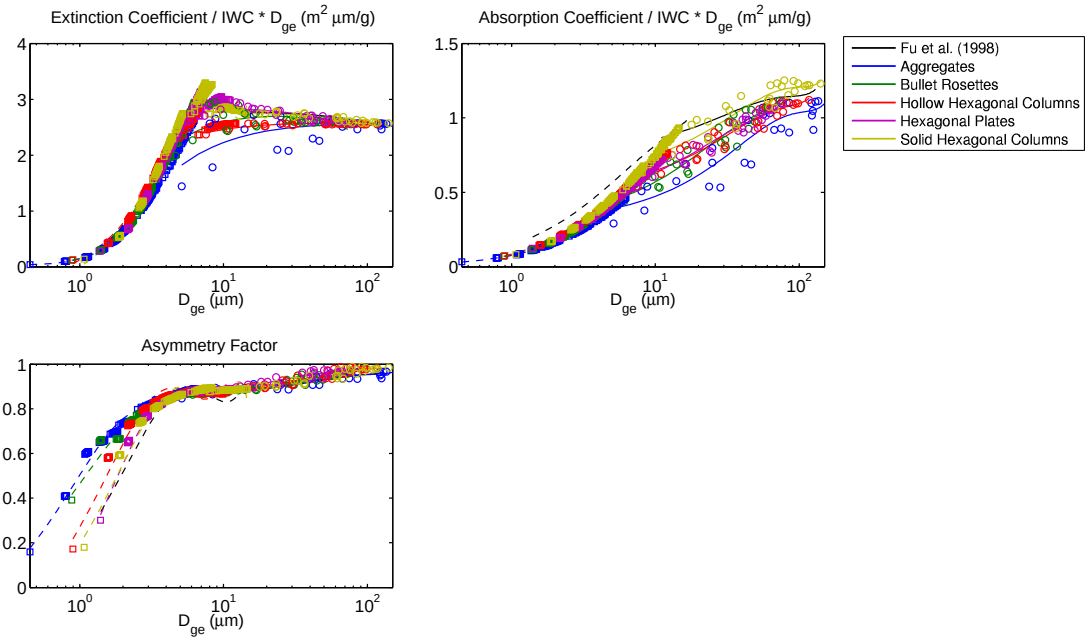

Figure 3.8: Band 8 parameterizations
Same as Figure 3.7, except for Band 8 (5.26 - 5.88 µm).

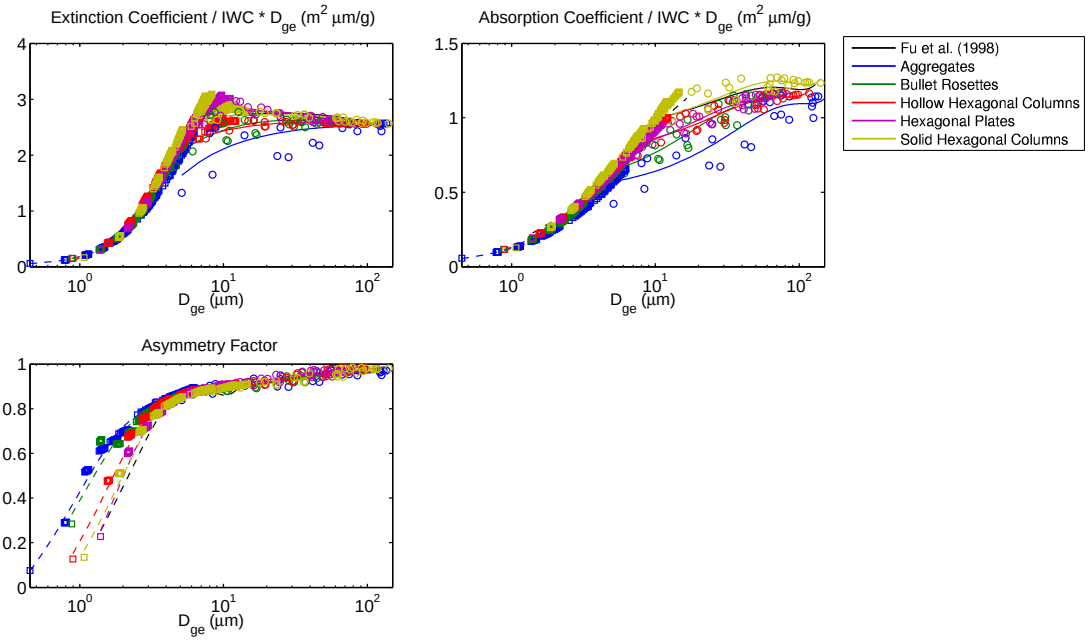

Figure 3.9: Band 9 parameterizations
Same as Figure 3.7, except for Band 9 (5.88 - 7.14 μm).

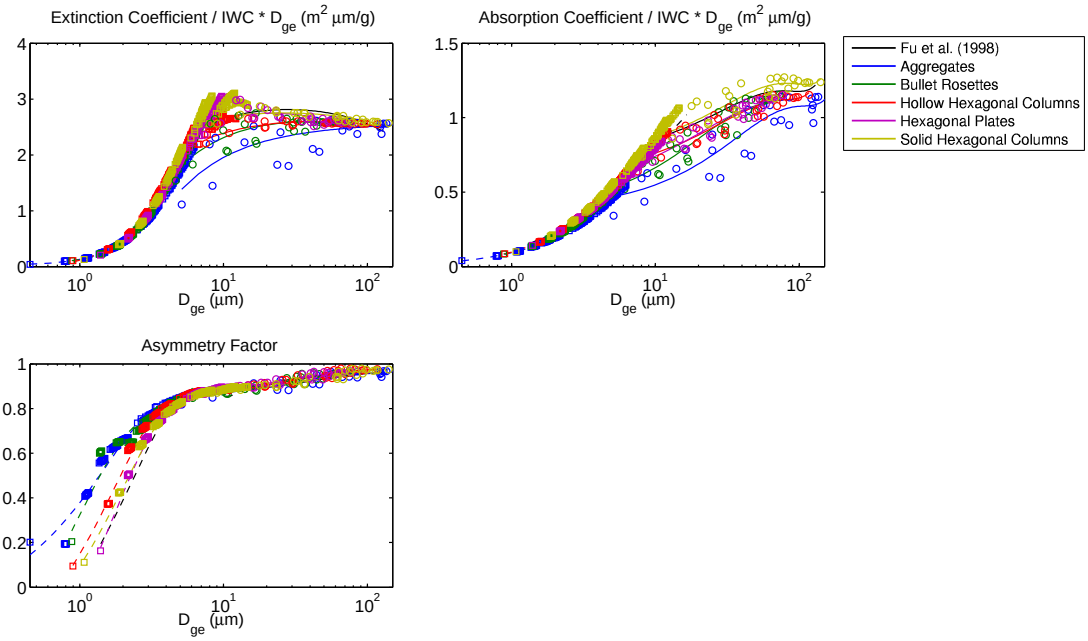

Figure 3.10: Band 10 parameterizations
Same as Figure 3.7, except for Band 10 (7.14 - 8.00 μm).

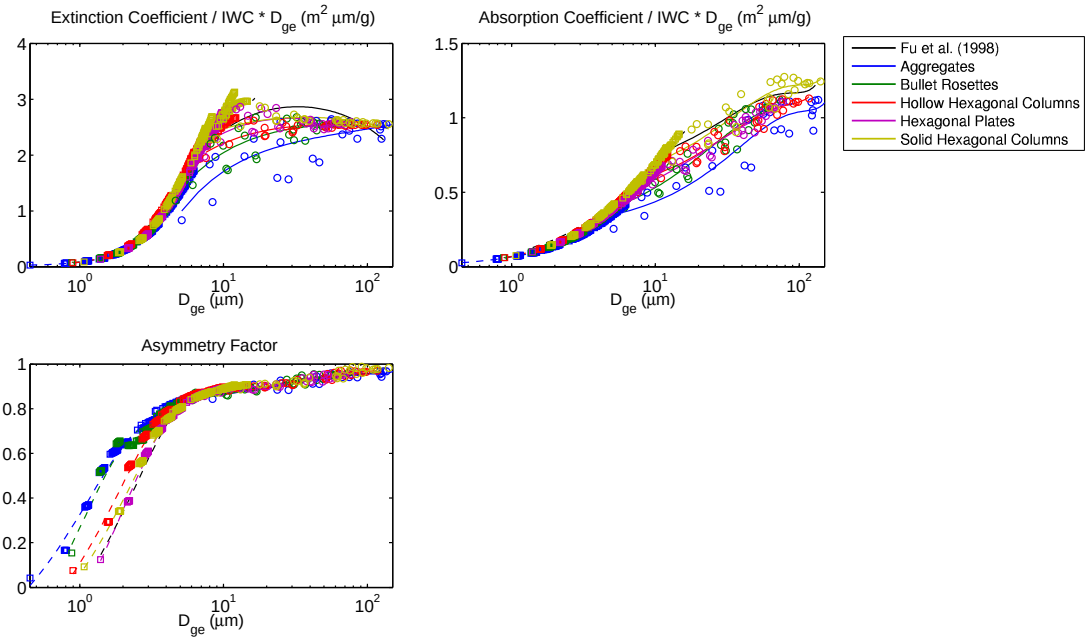

Figure 3.11: Band 11 parameterizations
Same as Figure 3.7, except for Band 11 (8.00 - 9.09 μm).

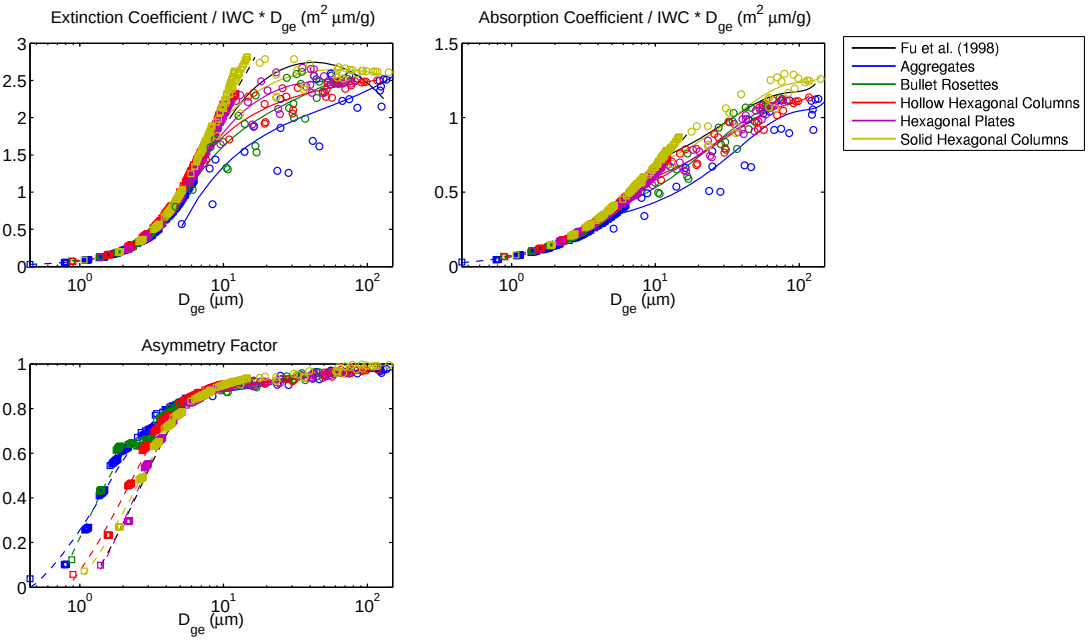

Figure 3.12: Band 12 parameterizations
Same as Figure 3.7, except for Band 12 (9.09 - 10.2 μm).

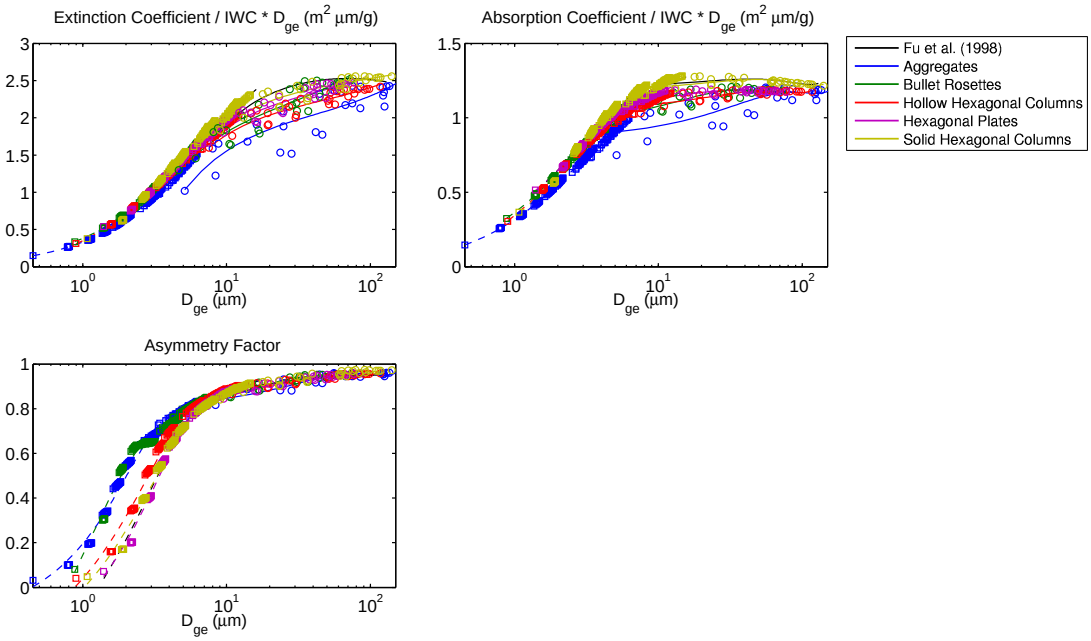

Figure 3.13: Band 13 parameterizations
Same as Figure 3.7, except for Band 13 (10.2 - 12.5 µm).

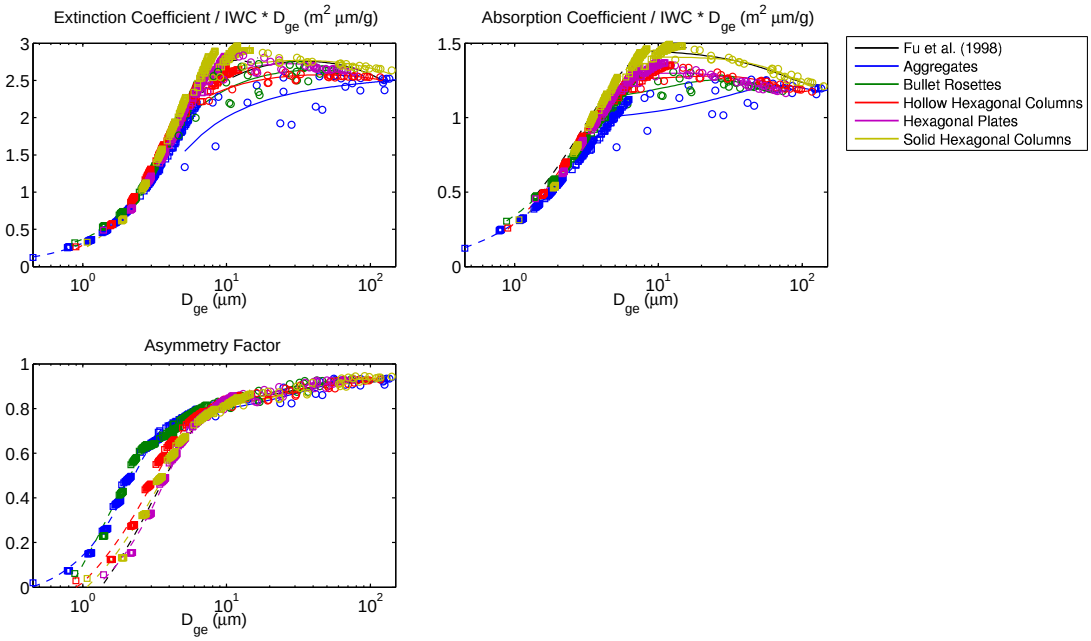

Figure 3.14: Band 14 parameterizations
Same as Figure 3.7, except for Band 14 (12.5 - 14.9 µm).

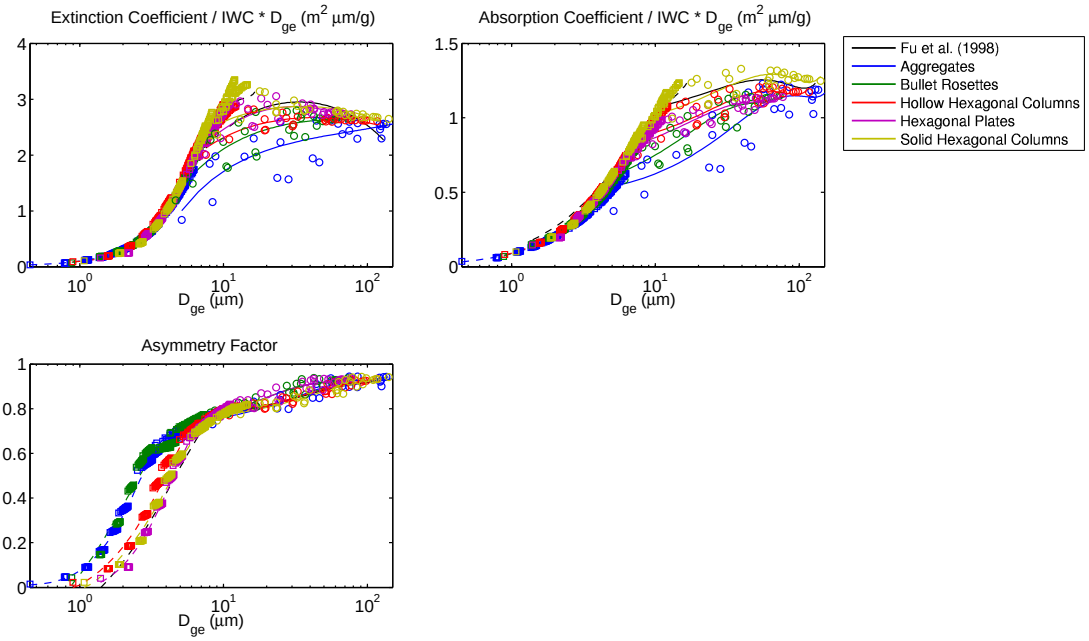

Figure 3.15: Band 15 parameterizations
Same as Figure 3.7, except for Band 15 (14.9 - 18.5 μm).

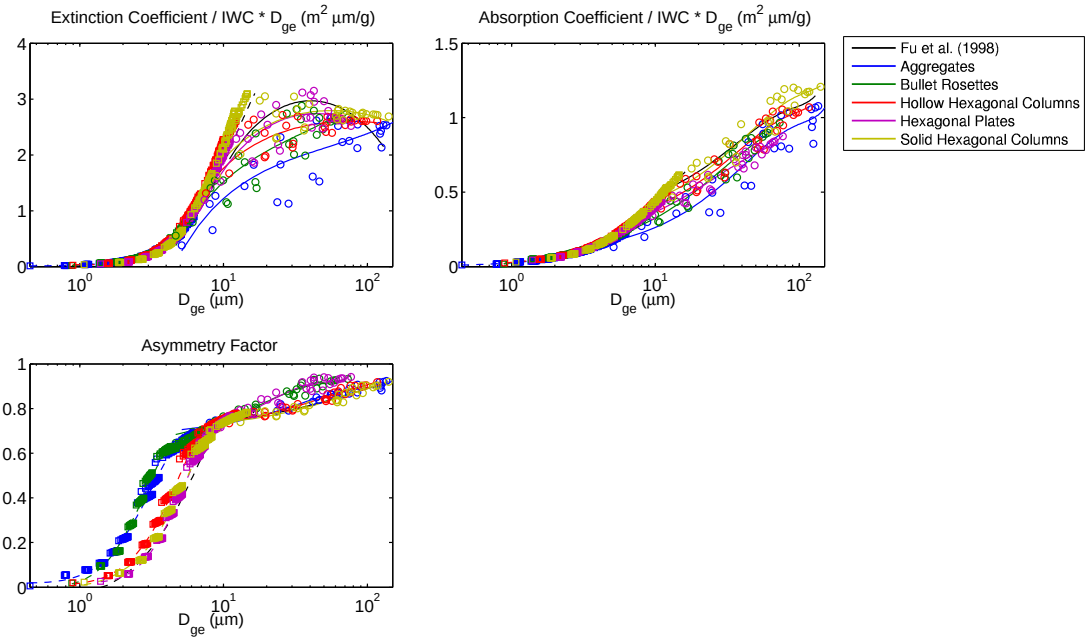

Figure 3.16: Band 16 parameterizations
Same as Figure 3.7, except for Band 16 (18.5 - 25.0 μm).

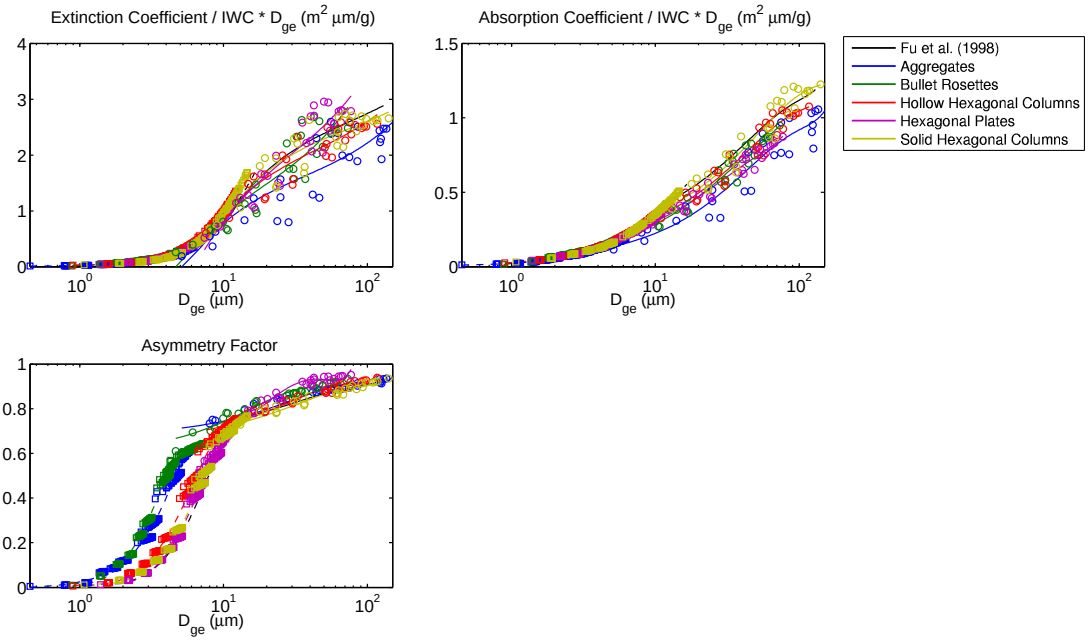

Figure 3.17: Band 17 parameterizations
Same as Figure 3.7, except for Band 17 (25.0 - 35.7 µm).

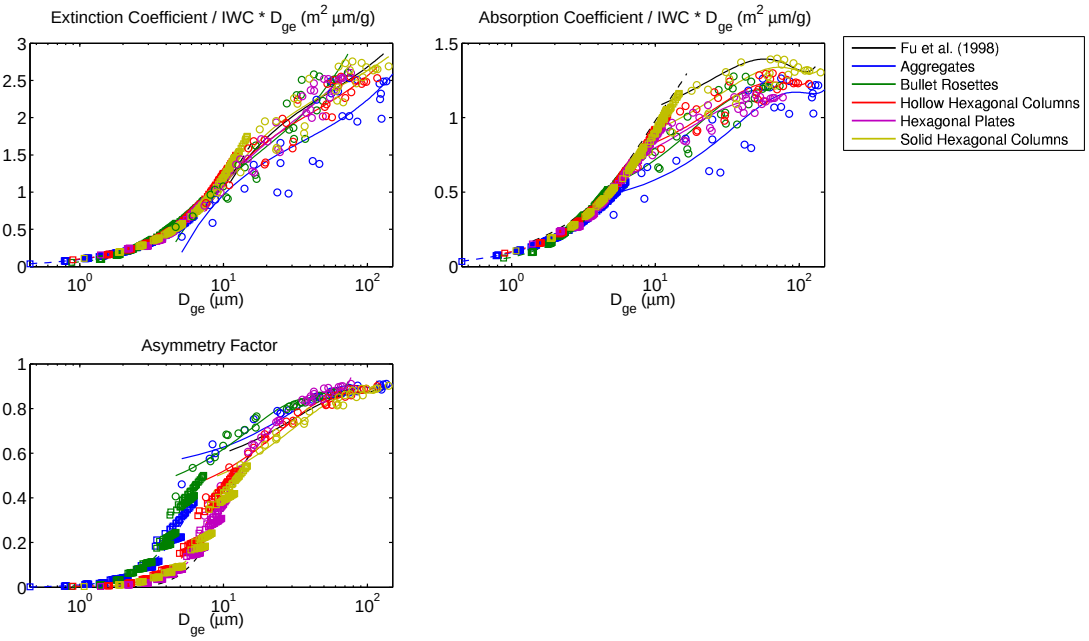

Figure 3.18: Band 18 parameterizations
Same as Figure 3.7, except for Band 18 (35.7 - 99.9 µm).

Fu (1996) are shown for comparison purposes. Figure 3.7 through Figure 3.18 show all three infrared SSPs, extinction coefficient*IWC/D_{ge}, absorption coefficient*IWC/D_{ge}, and asymmetry factor, for each of 12 spectral bands with wavelengths ranging from 4.55 to 99.9 μm. The parameterization for cirrus clouds with small D_{ge} are also shown for each shape. The parameterizations from Fu et al. (1998) and the corresponding small D_{ge} parameterizations from Robinson and Fu (2006) are shown for comparison purposes.

A few physical, common-sense checks can be applied to these parameterizations in order to evaluate their validity. In the geometric optics limit, i.e., when the ice particle size is much larger than the wavelength, Equation [2.11] is exactly valid. Therefore, the theoretical relationship between β_e, D_{ge}, and IWC as shown in Equation [2.11], requires that $(\beta_e D_{ge})$/IWC approach the value 2.52 as D_{ge} gets large when the wavelength is small. All bands show this relationship well for all shapes. The first two bands show that $(\beta_e D_{ge})$/IWC is very close to 2.52, while the remaining solar bands are within 0.22 of this value. The $(\beta_e D_{ge})$/IWC values for infrared bands are not close to 2.52, which is logical since their wavelengths are too long for the given particle size range to fall under the geometric optics limit. The weak absorption limit for single-scattering co-albedo, Equation [2.16], shows a directly linear dependence on D_{ge} and all shapes match this relationship very well, especially in the first two bands. Delta-function transmission increases with particle smoothness so it is not surprising that the rough aggregate values are the smallest, the hexagonal plates are the largest, and the bullet rosettes and columns are in the middle.

The main purpose for producing the solid hexagonal column parameterization from Yang et al. (2000) and Yang et al. (2005) was to compare it to the Fu (1996) and Fu et al. (1998) parameterizations, which are based on the solid hexagonal column shape. There is good agreement between the parameterizations throughout, with some exceptions. The asymmetry factor parameterizations are believed to have differences due to different prescribed aspect ratios, especially for small D_{ge} values. The smaller values of delta-function transmission from Yang et al. (2000) are likely due, in part, to

the fact that values below an unknown small size parameter threshold were set to zero. When integrating over the size distribution, this would serve to decrease the overall delta-function transmission values for small D_{ge}.

3.2. Aspect ratio definitions

The asymmetry factor and delta-function transmission parameterizations developed in Fu (2007), were designed to be used for cirrus clouds containing different particle shapes. However, its accuracy is only as good as the mean effective aspect ratio input. Therefore, particle aspect ratios, or the ratio of the diameter to the length, were carefully defined for each shape. The geometry for aggregates was defined in Yang and Liou (1998). It consists of a collection of 8 hexagonal elements, each with relative semi-widths, lengths, and orientations defined. In order to derive a mean aspect ratio for the entire particle, the aspect ratio of each element was calculated and weighted based on that element's projected area. The result was a mean effective aspect ratio of 0.67529 for all sizes.

The aspect ratios for the solid hexagonal columns in Fu (1996) are defined differently than those in Yang et al. (2000). The aspect ratio for the Fu (1996) solid hexagonal columns is defined as

$$\frac{D}{L} = \begin{cases} 1.00 & 0 < L \le 30\,\mu m \\ 0.80 & 30 < L \le 80\,\mu m \\ 0.50 & 80 < L \le 200\,\mu m \\ 0.34 & 200 < L \le 500\,\mu m \\ 0.22 & L > 500\,\mu m \end{cases} \qquad [3.1]$$

while the diameter for the solid hexagonal columns from Yang et al. (2000), following Mitchell and Arnott (1994), is defined as

$$D = \begin{cases} 0.70L & L < 100\,\mu m \\ 6.96L^{0.5} & L \ge 100\,\mu m \end{cases} \qquad [3.2]$$

where D is the particle diameter and L is equal to the maximum particle dimension, L. For hollow hexagonal columns, the cavity depth is defined as

$$d_h = 2\xi\overline{d}_h \quad [3.3]$$

where $\overline{d}_h = 0.25L$ is the mean cavity depth and ξ is a uniformly-distributed random value from 0 to 1. This results in a cavity depth ranging between 0 and 0.50L with an average value of 0.25L.

In the case of hexagonal plates, the diameter, not the length, is the maximum dimension of the particle (L = D) so it is used to define the particle length, L'. The particle length is defined by the following relationship from Pruppacher and Klett (1978):

$$L' = 1.7915D^{0.474} \quad [3.4]$$

The bullet rosette shape consists of 2 to 6 randomly-determined hexagonal column branches, each with one pyramidal cap. Its length-to-diameter relationship is defined by results from Mitchell and Arnott (1994)

$$D = 2.3104\ell^{0.63} \quad [3.5]$$

where ℓ is the length of the hexagonal part of the branch. For our calculation, we neglect the pyramidal caps so $\ell = L/2$.

As shown above, diameter-to-length relationships were defined for hexagonal columns, hexagonal plates, and bullet rosettes in Yang et al. (2000). However, the values produced by the actual database of calculated results were not always consistent with these relationships. The database for each shape provided a spherical diameter with equivalent projected area, D_a, and a spherical diameter with equivalent volume, D_v. D_a and D_v can be used in the area and volume equations for a sphere, respectively, to find the projected area and volume of the nonspherical particle. For example, using a D_a value for a given L from the hollow or solid hexagonal columns database, the projected area of the equivalent sphere can be calculated. The resulting projected area value can be inputted into the equation for hexagonal column projected area and solved for D. This D value is the diameter for the hexagonal column with maximum particle size, L.

The diameter-to-length relationships for solid and hollow columns were consistent between the equations and the database, but the bullet rosettes and hexagonal plates were not. The bullet rosette database diameter calculations, had errors ranging from 50% for small particles to around 11% for large particles when compared to those calculated from the relationship in Equation [3.5]. Due to the difficulties in reproducing the geometry used for the bullet rosettes and in order to remain consistent with the bullet rosette shape calculations in Fu (2007), Equation [3.5] was used to define the bullet rosette diameter. The hexagonal plate database particle length calculations, were within 9% of those calculated from the relationship in Equation [3.4], implying that a small, undocumented adjustment might have been made to this calculation. For this reason, the database-derived values of length were used.

For each shape, the particle aspect ratio is defined as D/L', where L' = L for all shapes except hexagonal plates. This quantity can be used along with the particle size distribution and the particle projected area to calculate the mean effective aspect ratio, as shown in Equation [2.33]. The mean effective aspect ratios for each ice particle shape were parameterized as a function of D_{ge} in the form

$$AR = e_0 + e_1 D_{ge} + e_2 D_{ge}^2 + e_3 D_{ge}^3 \qquad [3.6]$$

where e represents the regression coefficients. These coefficients are shown in Table B.11 of Appendix B. Figure 3.19 shows AR as a function of D_{ge} and the parameterization for all five shapes along with the Fu (1996) hexagonal columns. The AR-to-D_{ge} relationship for Fu (1996), bullet rosette, hollow hexagonal column, and solid hexagonal column shapes display a non-linear, inverse relationship. In contrast, the hexagonal plate shape displays a directly linear relationship between AR and D_{ge}. The difference between the solid and hollow hexagonal columns and the Fu solid hexagonal columns are apparent, especially for AR values larger than 0.6.

Figure 3.20 through Figure 3.25 show the asymmetry factor and delta-function transmission for each shape plotted as a function of AR for all solar bands. Also

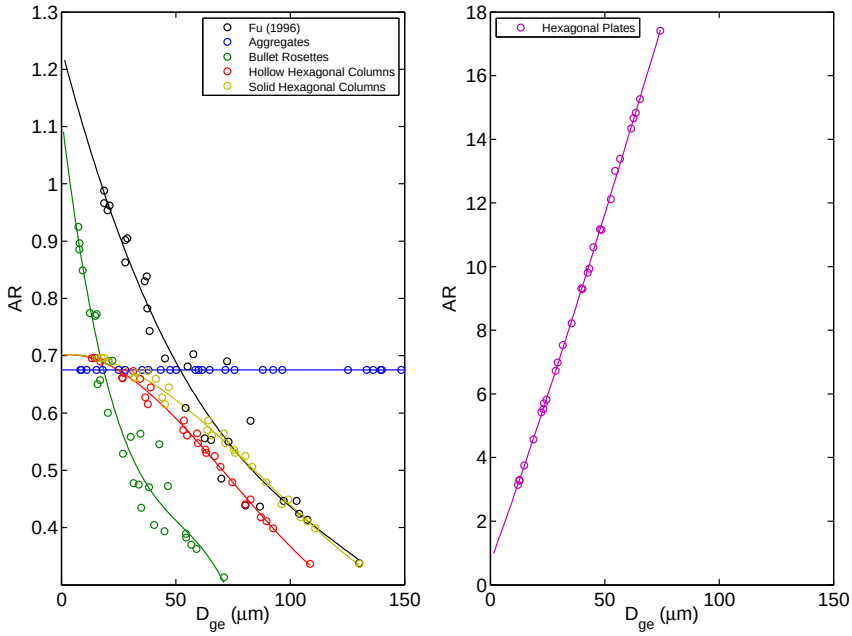

Figure 3.19: AR(D_{ge}) parameterizations
Reference calculations (circles) and parameterizations (solid lines) of the mean effective aspect ratio (AR) for each ice particle shape as a function of the generalized effective size (D_{ge}). The parameterizations from Fu (1996) are shown for comparison purposes.

plotted are the Fu (2007) parameterizations for comparison purposes. Notice that for bands 1 and 2 (Figure 3.20 and Figure 3.21), the asymmetry factor calculations for solid hexagonal columns, bullet rosettes, hexagonal plates, and, to some extent, hollow hexagonal columns line up well with the smooth asymmetry factor Fu (2007) parameterizations, while the aggregate calculations line up well with the rough Fu (2007) parameterizations. The solid hexagonal column and plate delta-function transmission calculations line up well with the Fu (2007) parameterizations, while the hollow hexagonal columns and bullet rosettes are smaller, yet still follow the approximate relationship. The aggregate delta-function transmission is equal to zero, as is expected for rough particles. For bands 3-6 (Figure 3.22 through Figure 3.25), the relationship between the shapes and the Fu (2007) parameterizations becomes increasingly poor. However, since only 15% of the solar energy lies within those bands and the scattering process is less important due to stronger absorption as the

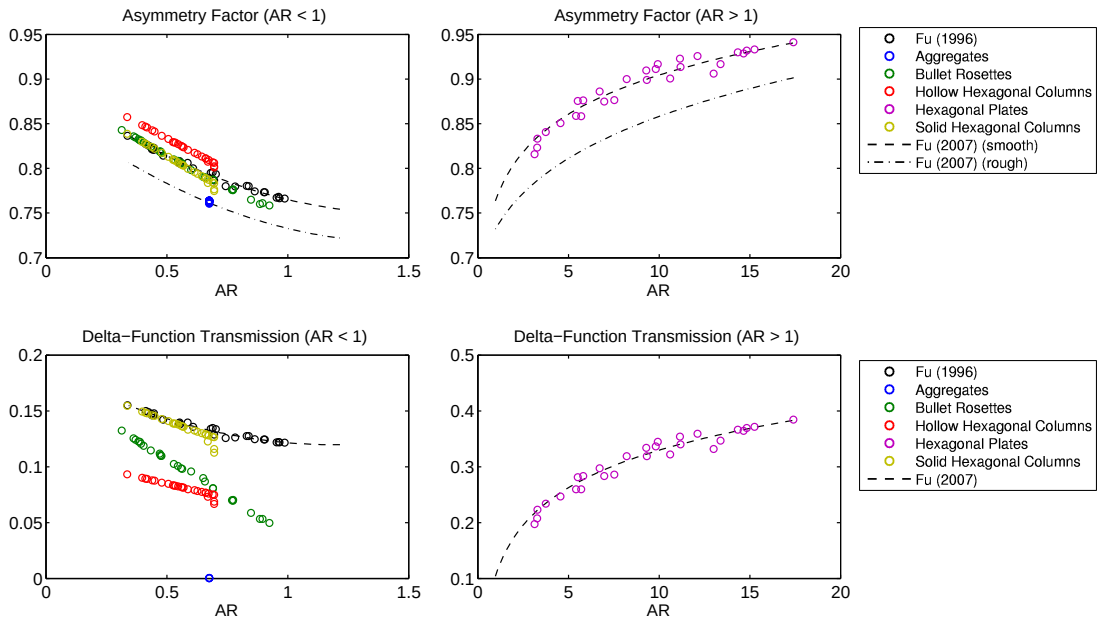

Figure 3.20: Band 1 g(AR) and f_δ(AR) parameterizations
Reference calculations (circles) and Fu (2007) parameterizations (dashed and dash-dotted lines) of the asymmetry factor and delta-function transmission in Band 1 (0.25 - 0.70 µm) for each shape as a function of the mean effective aspect ratio (AR). The reference calculations from Fu (1996) are shown for comparison purposes.

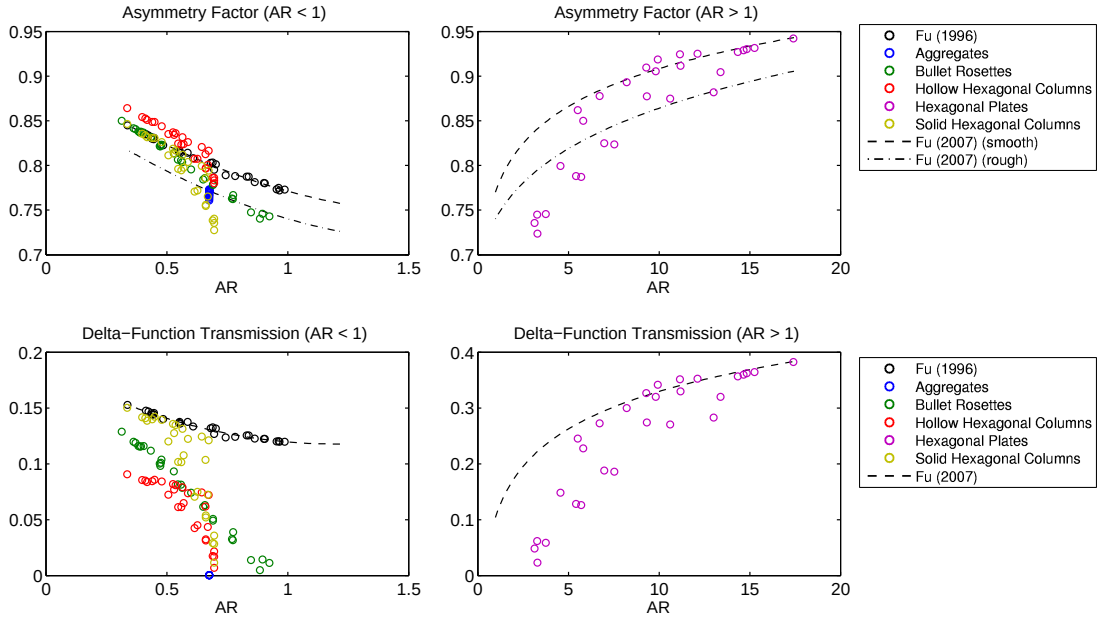

Figure 3.21: Band 2 g(AR) and f_δ(AR) parameterizations
Same as Figure 3.20, except for Band 2 (0.70 - 1.41 µm).

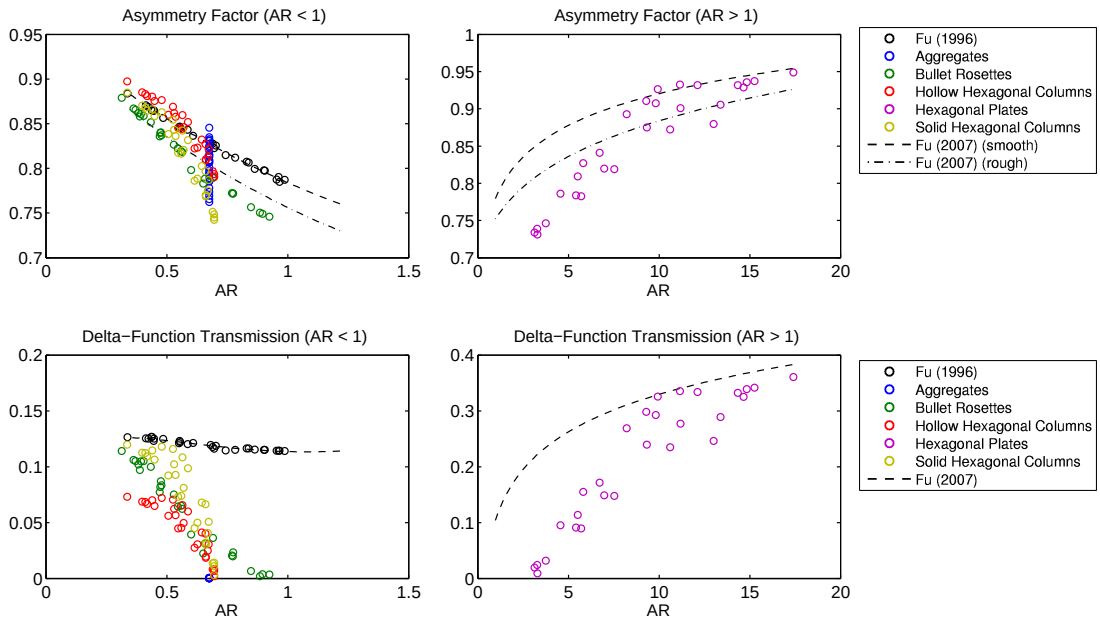

Figure 3.22: Band 3 g(AR) and f_δ(AR) parameterizations
Same as Figure 3.20, except for Band 3 (1.41 - 1.90 µm).

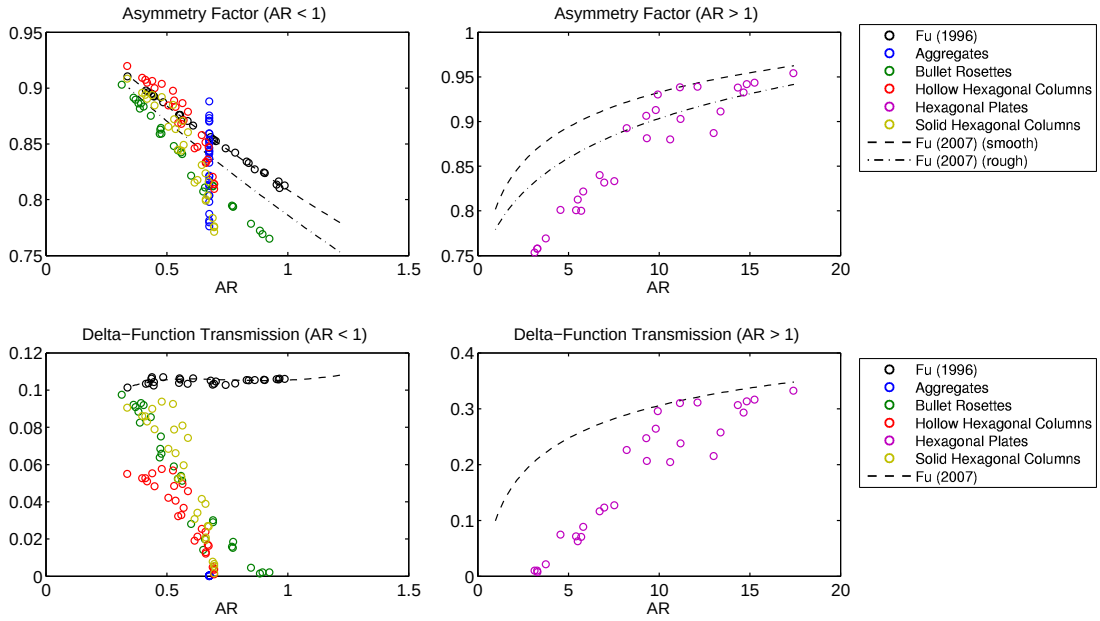

Figure 3.23: Band 4 g(AR) and f_δ(AR) parameterizations
Same as Figure 3.20, except for Band 4 (1.90 - 2.50 µm).

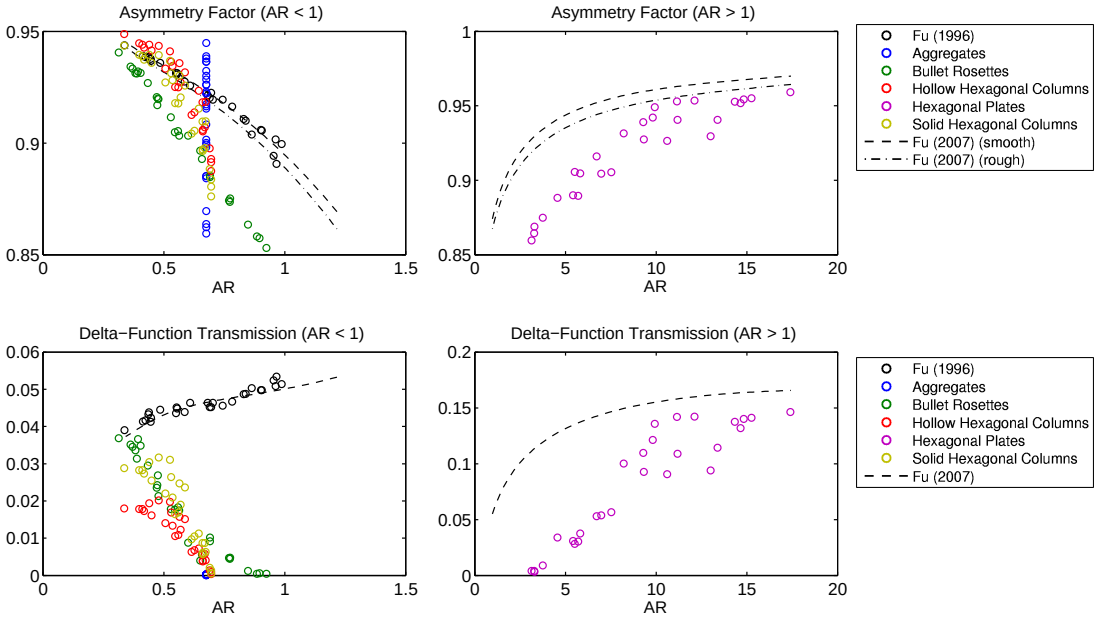

Figure 3.24: Band 5 g(AR) and f_δ(AR) parameterizations
Same as Figure 3.20, except for Band 5 (2.50 - 3.50 µm).

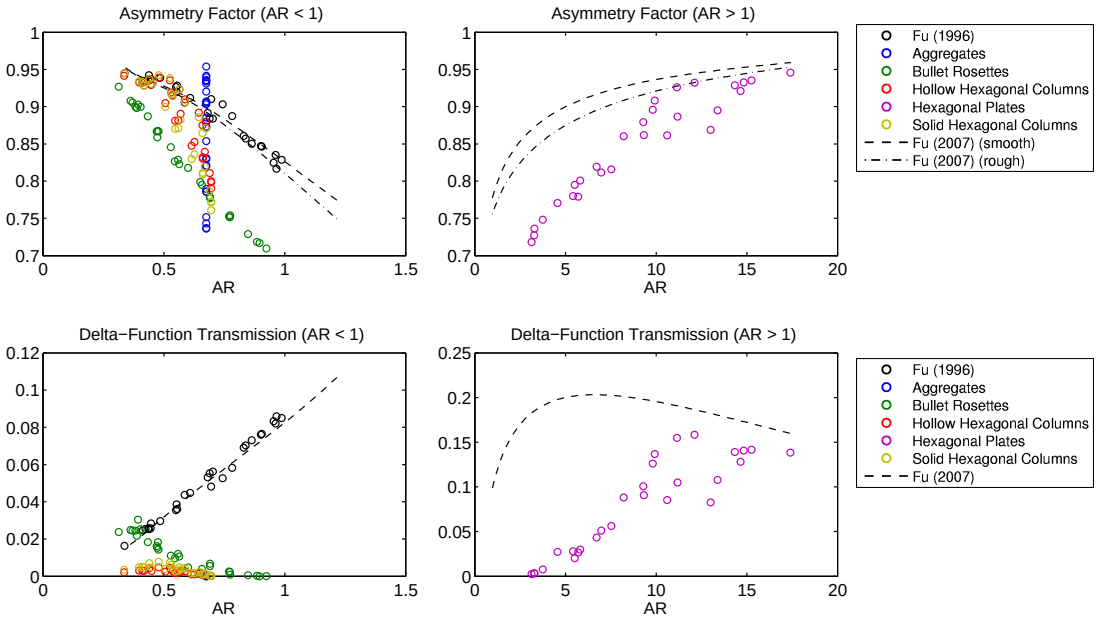

Figure 3.25: Band 6 g(AR) and f_δ(AR) parameterizations
Same as Figure 3.20, except for Band 6 (3.50 - 4.00 µm).

wavelength increases, this does not present a significant accuracy problem in the radiative energy budget simulation involving cirrus clouds.

3.3. The D_{ge} ranges for the parameterization

As with any parameterization, it is only sensible to use it within the bounds of the original calculations from which the parameterization was derived. Each shape has different D_{ge} ranges due to the parameter's dependency on particle volume and projected area, as shown in Equation [2.6]. Table 3.1 shows the D_{ge} ranges for the solar parameterizations and Table 3.2 shows the D_{ge} ranges for the infrared parameterizations. The smaller minimum D_{ge} values for the infrared calculations are due to the size distributions being interpolated to L values as small as 2 μm for infrared, while for the solar calculations, the smallest L value is 8.75 μm. The maximum L values are the same in both spectral regions, but integration over the different L ranges still results in different maximum D_{ge} values.

Table 3.3 shows the data extent for the small D_{ge} infrared parameterizations. For each shape parameterization, usable D_{ge} values range from the minimum small D_{ge} value to the maximum solar or infrared D_{ge} value, whichever is smaller. The shape distribution with the smallest overall range is that for bullet rosettes followed by hexagonal plates. The shape distribution with the largest overall range is that for

Table 3.1: Solar D_{ge} ranges
The range of D_{ge} values calculated from the 28 size distributions in Fu (1996) for each ice particle shape, as defined in the text. The shape "Fu Solid Hex. Cols." refers to the specific shape definition used in the Fu (1996) parameterizations.

Shape	D_{ge} (μm)
Fu Solid Hex. Cols.	18.63 - 130.24
Aggregates	8.29 - 166.79
Bullet Rosettes	7.46 - 71.09
Hollow Hex. Cols.	13.27 - 108.64
Hexagonal Plates	12.13 - 74.35
Solid Hex. Cols.	15.91 - 130.26

Table 3.2: Infrared D_{ge} ranges
Same as Table 3.1, except the 28 size distributions are from Fu et al. (1998), which were based upon those in Fu (1996), but interpolated to smaller ice particle sizes.

Shape	D_{ge} (μm)
Fu Solid Hex. Cols.	11.02 - 129.62
Aggregates	5.12 - 161.89
Bullet Rosettes	4.65 - 73.34
Hollow Hex. Cols.	7.54 - 117.33
Hexagonal Plates	7.39 - 77.18
Solid Hex. Cols.	9.04 - 140.70

aggregates followed by solid hexagonal columns, Fu solid hexagonal columns, and hollow hexagonal columns.

In order to use the added range of the infrared small D_{ge} parameterization, it is necessary to extend the solar parameterizations to the minimum values of the infrared small D_{ge} parameterizations. In doing so, some parameterization values became negative. This was especially an issue with the delta-function transmission parameterizations. If any SSP value is negative, it is non-physical. In this situation, the negative values were on the order of 0.1 or smaller so it was not unreasonable to set them to zero. This was done with logic code in the model and these changes are also reflected in the solar parameterization plots, Figure 3.1 through Figure 3.6. This change did not have a discernable impact on cirrus modeling results.

Since there is an overlap between the infrared and small D_{ge} infrared parameterizations, it is useful to determine an optimal transition point between the use of each set of parameterizations. This was determined quantitatively by testing several model runs with a thin cirrus case in order to minimize the jump in flux density values at the transition point. First, test D_{ge} cutoff values in 0.5 μm intervals within the range of each shape's overlap were chosen. Each one was used as the threshold between small D_{ge} infrared and infrared parameterizations. The model was then run twice, once at a D_{ge} value 0.01 μm smaller than the test cutoff value and once at a D_{ge} value 0.01 μm larger than the test cutoff value. This was repeated for all test cutoffs. The cutoff that yielded the smallest difference in flux density across the threshold was chosen as the optimal threshold for that shape. The threshold values are shown in Table 3.4. In the Fu-Liou Radiation Model, any D_{ge} value less than or equal to each threshold will result in the use of the small D_{ge} infrared parameterization and any D_{ge} value larger than the threshold will use the infrared parameterization.

Table 3.3: Infrared small D_{ge} ranges
The range of D_{ge} values calculated from several truncated versions of the 28 size distributions in Fu et al. (1998) for each ice particle shape, as defined in the text. The shape "Fu Solid Hex. Cols." refers to the specific shape definition used in the Fu (1996) parameterizations.

Shape	**D_{ge} (µm)**
Fu Solid Hex. Cols.	1.40 - 17.34
Aggregates	0.45 - 6.24
Bullet Rosettes	0.88 - 7.27
Hollow Hex. Cols.	0.90 - 12.21
Hexagonal Plates	1.40 - 11.11
Solid Hex. Cols.	1.07 - 14.64

Table 3.4: Small D_{ge} threshold values
Thresholds for each ice particle shape shape that determine at what point the small D_{ge} parameterizations are used. Values at our below the threshold use the small D_{ge} parameterizations, while values above that threshold use the regular infrared parameterization. The shape "Fu Solid Hex. Cols." refers to the threshold between the Fu et al. (1998) and Robinson and Fu (2006) parameterizations.

Shape	**D_{ge} (µm)**
Fu Solid Hex. Cols.	11.0
Aggregates	7.0
Bullet Rosettes	5.5
Hollow Hex. Cols.	7.5
Hexagonal Plates	7.5
Solid Hex. Cols.	9.0

CHAPTER 4: APPLICATION OF THE NEW PARAMETERIZATION TO EVALUATE THE CIRRUS RADIATIVE ENERGY BUDGET

The parameterizations discussed in Chapters 2 and 3 can now be used to test the impact of the cirrus SSP parameterization on the evaluation of the cirrus radiative energy budget. A recent version of the Fu-Liou Radiation Model produced by NASA Langley was used for these simulations. All shape-explicit parameterizations presented in Chapter 3 have been inserted into this model. Parameterizations from Fu (1996), Fu et al. (1998), and Fu (2007) are tested against these shape-explicit parameterizations by calculating two cirrus scenarios.

4.1. Fu-Liou Radiation Model

The Fu-Liou Radiation Model utilizes a delta-four stream radiative transfer scheme outlined in Liou et al. (1988) and Fu (1991). Gas absorption is parameterized by the correlated-k distribution method (Fu and Liou, 1992). In this study, the vertical resolution is 1 km from 0 to 8 km, 9 to 10 km, and 12 to 60 km. Additional levels at 8.8, 10.8, and 11.2 km allowed the modeling of thinner cirrus clouds in this and previous work. These intermediate levels locally increased the resolution to 800 or 200 m, depending on each level's proximity to the nearest kilometer. From 60 to 70 km, the resolution is 2 km. There are a total of 69 levels, which encompass 68 layers.

In our simulations, the atmosphere is modeled by profiles of temperature and height-dependent concentrations of H_2O, O_3, CH_4, and N_2O from Anderson et al. (1986) along with a height-independent concentration of CO_2. The Fu-Liou Radiation Model produces two principal outputs. One is flux density, the amount of energy impinging upon a unit area over a unit time (W m^{-2}). This is the fundamental quantity for radiative energy integrated over a hemispheric solid angle (Liou 2002). It is calculated for each model level. The flux density is given by the model in downward and upward solar and infrared quantities. Based on these quantities, net solar and net infrared flux densities can be defined as shown below:

$$\text{Net Solar} = \text{Downward Solar} - \text{Upward Solar} \quad [4.1]$$

$$\text{Net Infrared} = \text{Downward Infrared} - \text{Upward Infrared} \quad [4.2]$$

The other output is radiative heating rate, or the temperature change over a unit time due to absorbed radiation. It is mathematically defined as

$$\frac{dT}{dt} = \frac{1}{\rho c_p}\frac{dF}{dz} \quad [4.3]$$

where F is the net flux density, z is height from the surface, t is time, ρ is the air density, and c_p is the specific heat at constant pressure. This quantity is calculated for each model layer. Heating rate is given as solar, infrared, and total quantities.

In order to simplify the test and its explanation, the parameterizations have been grouped into three major configurations. The first one involves the use of the Fu (1996) parameterizations for solar SSPs and the Fu et al. (1998) parameterizations for the infrared SSPs. These will be referred to as the "original parameterizations". The original parameterizations produce one set of results since the parameterizations are solely based upon the solid hexagonal column geometry. The second one involves the use of the Fu (1996) parameterizations for the extinction coefficient and single-scattering co-albedo and the Fu (2007) parameterizations for the asymmetry factor and delta-function transmission along with the Fu et al. (1998) parameterizations for the infrared SSPs. These will be referred to as the "modified parameterizations". The modified parameterizations use shape-explicit AR values to calculate the solar asymmetry factor and delta-function transmission for each shape. Any shape dependencies that may exist from other SSPs are not taken into account. The last one involves the use of the five sets of shape-explicit parameterizations for aggregates, bullet rosettes, hollow hexagonal columns, hexagonal plates, and solid hexagonal columns, as developed in Chapter 3. The solid hexagonal shape parameterizations from Fu (1996) and Fu et al. (1998) are also included. These will be referred to as the "new parameterizations". This set is considered the most accurate since each shape is

explicitly defined within the radiative calculations from which the parameterizations were constructed.

4.2. Clear sky results

For the purposes of this work, the model was set to use a baseline atmosphere at 45°N during the summer solstice with a solar surface albedo of 0.3 and a constant CO_2 concentration of 380 ppmv. To facilitate a simulation of diurnal mean radiative response to the presence of cirrus clouds, a solar zenith angle of 60° and one half of the solar constant (1368.0/2 = 684 W m^{-2}) was used. Profiles of the clear sky net solar, net infrared, and net total flux density and solar, infrared, and total heating rate results are shown in Figure 4.1.

The net solar flux density is positive throughout the atmosphere, meaning there is net downward solar radiative energy at all levels. Solar radiation scattering increases as the density of the atmosphere increases, resulting in smaller net solar

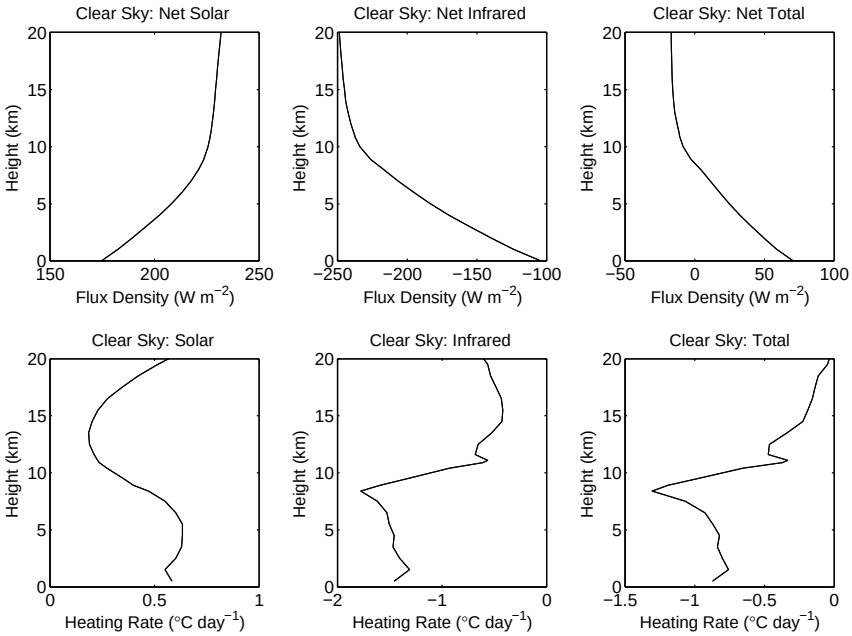

Figure 4.1: Clear sky net flux density and heating rate profiles
Clear sky radiative calculations at 45°N during the summer solstice with a solar surface albedo of 0.3 and a constant CO_2 concentration of 380 ppmv. The top row shows results in terms of flux density and the bottom row shows results in terms of heating rate.

values lower in the atmosphere with the change being greatest in the lowest 10 km. Above 10 km, the net solar flux density is around 224 W m^{-2}, while below it decreases to 175 W m^{-2}. The net infrared flux density is negative throughout the atmosphere, meaning there is net upward infrared radiative energy at all levels. As height increases, the air density decreases, which leads to fewer instances of absorption and emission and more infrared radiation predominantly traveling in the upward direction from lower levels. Above 10 km, the net infrared flux density is around -242 W m^{-2}, while below it decreases in magnitude to -104 W m^{-2}. The net flux density is the summation of the net solar and net infrared flux densities. At the surface, it is about 71 W m^{-2} and it decreases to 0 at approximately 8.8 km. Above that, the net flux density is around -14 W m^{-2}.

Heating rate increases with an increase of net flux density with height or a decrease of air density with height, as shown in Equation [4.3]. Solar radiation results in warming throughout the atmosphere with a local maximum of 0.6 °C day^{-1} at 5.5 km. Warming peaks around 14 °C day^{-1} outside of the plot domain at 48 km due to the low air density. At higher altitudes, the net solar flux density changes very little with height, causing a decrease in the heating rate despite the very low air density. Infrared radiation results in cooling throughout the atmosphere with a local maximum of -1.8 °C day^{-1} at 8.4 km. Cooling peaks around 12 °C day^{-1} outside of the plot domain at 51 km for the same reason as did warming. The net heating rate is the summation of the solar and infrared heating rates. Near the surface, it is about -0.9 °C day^{-1} and it increases to near 0 at approximately 20 km. Above that, it is near 0 or positive with a peak of 3.5 °C day^{-1} at 46 km.

There is a small infrared heating rate spike at 10.9 km, but its presence is understood. Emission is dependent on temperature so when the temperature profile transitions from a constant lapse rate below 11 km to an isothermal atmosphere at and above 11 km, the differing infrared emission above and below the layer encompassing the transition results in a heating rate spike. This occurs in the layer centered at 10.9 km. To assure this was the cause, the transition between the constant lapse rate and

isothermal conditions was temporarily moved to a new location. As a consequence, the spike moved to this new transition location as well. Removal or lessening of the spike would probably be possible with a more gradual temperature transition between the troposphere and the stratosphere, but since the 10.9 km heating rate with cirrus present is much larger than the spike, it is reasonable to leave it there.

4.3. Cirrus radiative forcing

Two different cirrus configurations were used to evaluate the importance of the shape dependence of SSP parameterizations in the cirrus radiative energy budget evaluation. One is that of a cirrostratus deck based on a size distribution from Heymsfield (1975). Cirrus is present from 9 to 11 km with an ice crystal size distribution characterized by a D_{ge} of 40 μm and IWC of 0.01 g m^{-3}, which implies a visible optical depth of 1.3. This cirrostratus scenario will be abbreviated as "CS". The second model scenario is a thin cirrus deck, which could also be used as a one-dimensional representation of a contrail. Cirrus is present from 10.8 to 11 km with an ice crystal size distribution characterized by a D_{ge} of 15 μm and IWC of 0.003 g m^{-3}, which implies a visible optical depth of 0.1 (Baughcum and Danilin, personal communication, 2006). This thin cirrus scenario will be abbreviated as "TC". The CS scenario represents a typical cirrus cloud, while the TC scenario represents a cirrus cloud that is much thinner, both optically and geometrically, and consists of relatively small ice crystals. By looking at both scenarios, conclusions will be made regarding the overall performance of the original and modified parameterizations compared to the new parameterizations.

One fundamental way of visualizing the radiative impact of cirrus clouds is by quantifying the difference between the results with the cirrus present and in clear sky conditions. This is typically referred to as cloud forcing, but we will refer to it more specifically as cirrus forcing (CF). It is defined mathematically below

$$CF = F - F_{\text{clear}} \qquad [4.4]$$

where F and F_{clear} are quantities of net solar, net infrared, or net total flux density or heating rate. F represents one of these quantities when cirrus is present, while F_{clear} represents the corresponding quantity for clear sky conditions. Positive cirrus forcing means that the presence of the cirrus cloud increases the net flux density at a given level or increases the heating rate within a given layer, while negative cirrus forcing implies the opposite effect.

Figure 4.2 shows the cirrus forcing for both scenarios in terms of flux density using the new parameterizations. Net solar quantities are negative throughout the atmosphere in both scenarios. The highest magnitude forcing occurs at the base of the cloud with a substantial decrease at the top of the cloud. Above the cloud in both cases, forcing values remain about equal with height, while below the cloud in both cases the magnitude of forcing decreases with decreasing height. The overall range of forcing for CS is roughly -20 to -54 W m^{-2}, while for TC it is -4 to -5.4 W m^{-2}. Hexagonal plates have the smallest forcing magnitude in both cases and it is much smaller relative to the other shapes in the CS scenario. Aggregates produce the largest

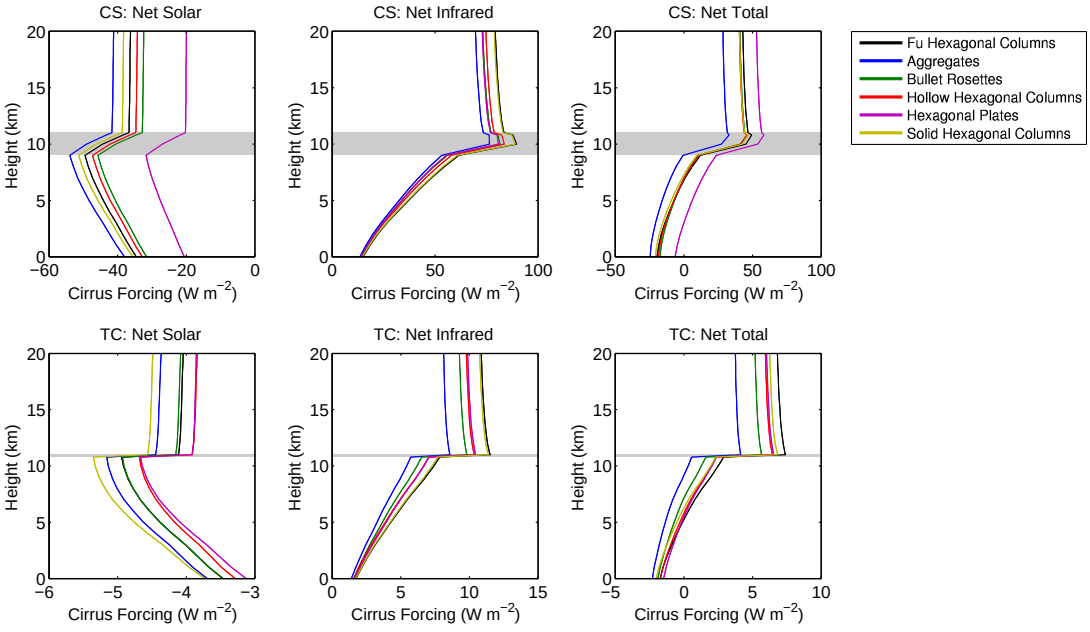

Figure 4.2: Cirrus forcing profiles in terms of net flux density
Cirrus forcing profiles in terms of net flux density using the new parameterizations. The top row shows results for the CS case and the bottom row shows results for the TC case.

magnitude of forcing in the CS case, but solid hexagonal columns exhibit the largest forcing in the TC case with aggregates not far behind. Net solar forcing by solid hexagonal columns and the Fu (1996) parameterization closely match in a relative sense for the CS case, but not the TC case. In an absolute sense, the variation between these two parameterizations based on solid hexagonal columns shapes is 2 W m^{-2} for CS and 0.5 W m^{-2} for TC.

Also shown in Figure 4.2 are the net infrared flux densities. This forcing is positive throughout the atmosphere in both scenarios. The largest forcing occurs in the middle of the cloud for CS and at the top of the cloud for TC. Much like the net solar forcing, infrared cirrus forcing values remain about equal with height above the cloud and it decreases with decreasing height below the cloud. The overall range of forcing for CS is roughly 14 to 90 W m^{-2}, while for TC it is only 1.4 to 11.5 W m^{-2}. Contrary to solar forcing, aggregates exhibit the smallest forcing, while solid hexagonal columns and Fu et al. (1998) exhibit the largest forcing for both cases. Net infrared forcing by solid hexagonal columns and the Fu (1996) parameterization closely match in a relative sense for both cloud cases and in an absolute sense, the variation is 0.8 W m^{-2} for CS and 2.9 W m^{-2} for TC. Overall, the relative forcing magnitudes are less sensitive to shape in the infrared than solar.

The net forcing, a summation of the solar and infrared forcing, is largest within the cloud and much like the solar and infrared forcing, values remain about equal with height above the cloud and it decreases with decreasing height below the cloud. The overall range of forcing for CS is roughly -24 to 59 W m^{-2}, while for TC it is -2.3 to 7.4 W m^{-2}. The transition between negative forcing near the surface and positive forcing above occurs between 4 km and near the base of the cloud in both cases.

Figure 4.3 shows the cirrus forcing for both scenarios in terms of heating rate using the new parameterizations. The solar heating rate forcing quantities are positive within the clouds and close to zero everywhere else. The largest forcing occurs near the top of the cloud for CS and somewhere within the cloud for TC. The forcing peaks at around 2 °C/day for CS and 1 °C/day for TC. The infrared forcing heating

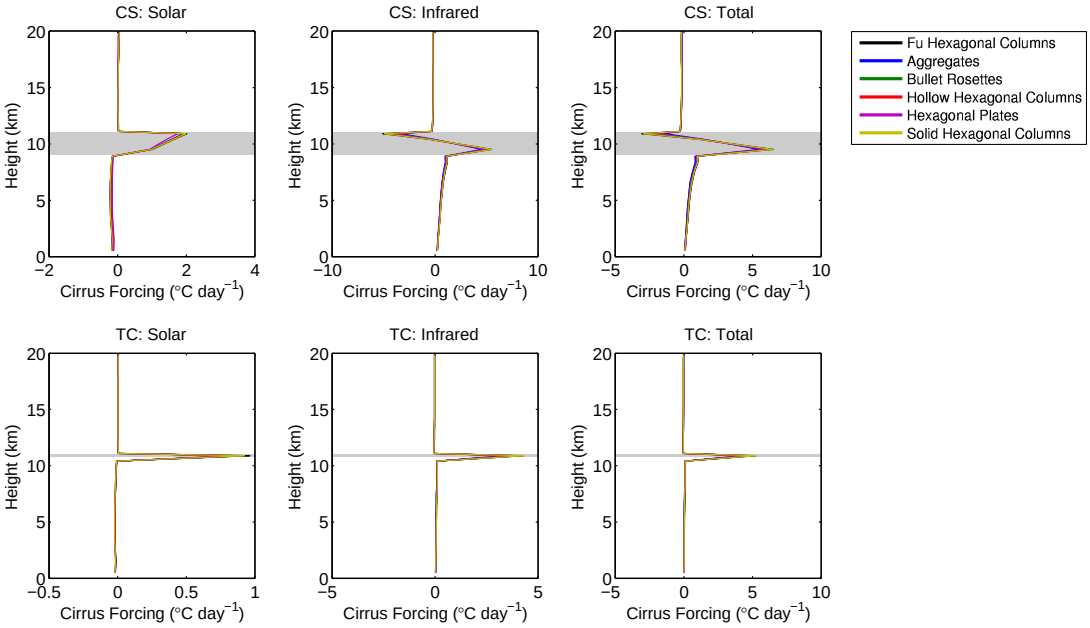

Figure 4.3: Cirrus forcing profiles in terms of heating rate
Same as Figure 4.2, but in terms of heating rate.

rates are positive within the cloud for TC, but for CS are positive in the lower part of the cloud and negative in the upper part of the cloud. This clearly demonstrates the opacity of the cloud to infrared radiation since much less of the higher energy surface radiation is reaching the upper part of the cloud. Above the cloud in both cases, the forcing is near zero. The heating rate peaks at around ±5 °C/day for CS and 5 °C/day for TC. In contrast to the forcing flux density, all shape parameterizations produce nearly identical net solar and net infrared heating rate cirrus forcing. The resulting net forcing within the cloud is -3 to 6.5 °C/day for CS and 5 °C/day for TC.

4.4. Cirrus shape errors

Figure 4.2 and Figure 4.3 represent the most accurate cirrus forcing currently possible by this model because all cirrus calculations use parameterizations that explicitly model each specific shape considered. By testing each new parameterization SSP individually with the remaining SSPs being modeled by the original or modified parameterizations, the relative shape dependence of each SSP can

be quantified based on how well it reproduces the new parameterization results. Since the accuracy of cirrus forcing is of paramount concern, the percentage error of cirrus forcing using a specific parameterization set with respect to the cirrus forcing produced using the new parameterizations can be used to quantify the error. This quantity will be called the "cirrus shape error" and it is defined mathematically below:

$$\text{Cirrus Shape Error} = \frac{CF - CF_{\text{new}}}{CF_{\text{new}}} * 100 \qquad [4.5]$$

CF is the net solar, net infrared, or net total flux density or heating rate cirrus forcing using a test set of parameterizations and CF_{new} is the corresponding quantity using only the new parameterizations.

Figure 4.4 shows the net solar flux density cirrus shape error for both cloud cases. The first two columns are the tests for CS and the last two are the tests for TC. The first test, dubbed "New: none" is simply a comparison between the original and new parameterizations. For CS, cirrus shape error is as high as 82% for plates, while other shapes range from -12% to 12%. For TC, cirrus shape error is between -10% and 11% for all shapes. Next, the original parameterization solar extinction coefficient is replaced by that from the new parameterization (New: β_e). In both cloud cases, the results are nearly identical to the previous set. This clearly shows a weak impact of particle shape dependence of the solar extinction coefficient parameterization on the cirrus radiative energy budget. The same conclusion can be made about the impact of the single-scattering co-albedo (New: ω). A test of the solar asymmetry factor (New: g) yields much smaller cirrus shape errors ranging from -6% to 12% for CS and -6% to 2% for TC. This clearly shows that the solar asymmetry factor is strongly dependent on particle shape. A test of the solar delta-function transmission (New: f_δ) also shows a decrease in the error, but not to a great extent. However, if the new solar asymmetry factor and delta-function transmission are used together along with the original parameterizations for all other SSPs (New: g, f_δ), the error is drastically reduced to ranging from -2% to 3% for CS and -1% to 2% for TC.

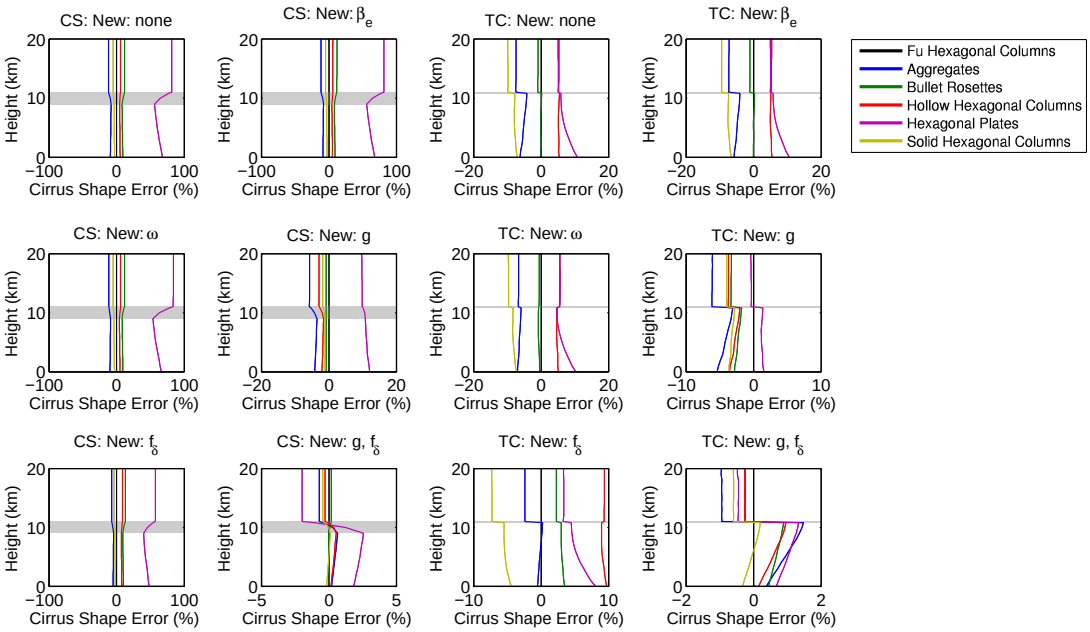

Figure 4.4: Net solar flux density cirrus shape error: original-to-new comparison
Cirrus shape error profiles in terms of net solar flux density cirrus forcing. In each test, the original parameterizations are used along with any new parameterization SSPs indicated by "New" above each plot. The cirrus forcing using each test set of parameterizations is compared to that using the new parameterizations. The first two columns show results for the CS case and the last two columns show results for the TC case.

The modified parameterization attempts to account for the shape dependence exhibited above by parameterizing solar asymmetry factor and delta-function transmission as a function of AR and using D_{ge}-to-AR parameterizations for each shape. Figure 4.5 shows the net solar flux density cirrus shape error for both cloud cases, but this time the starting point is the set of modified parameterizations instead of the original parameterizations. A direct comparison of the modified and new parameterizations (New: none) shows error values of -14% to 1% for CS and -32% to -1% for TC. When the extinction coefficient (New: β_e), single-scattering co-albedo (New: ω), or both (New: β_e, ω) are used from the new parameterizations, the error remains nearly the same. The plots "New: g, f_δ" from Figure 4.4 and "New: none" from Figure 4.5 use the identical parameterizations except g and f_δ are parameterized as a function of AR in Figure 4.5. The errors are much larger in Figure 4.5. These differences are likely due to the imperfect match of the asymmetry factor and delta-

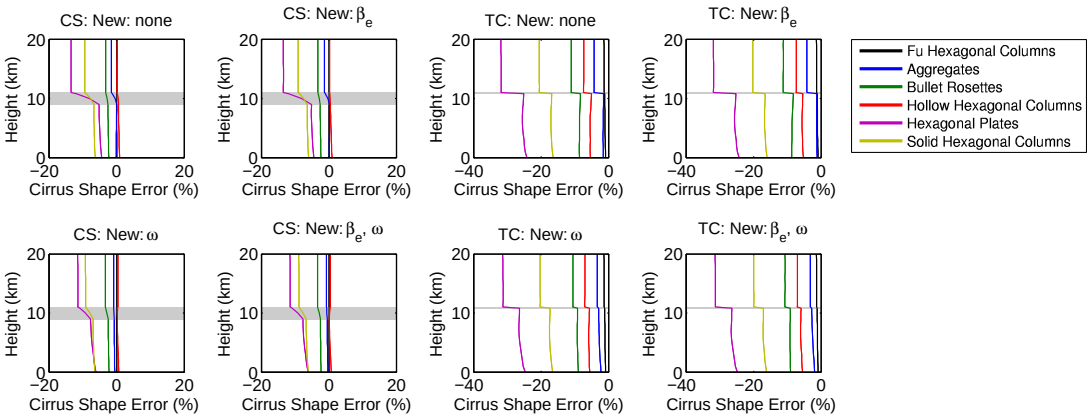

Figure 4.5: Net solar flux density cirrus shape error: modified-to-new comparison
Same as Figure 4.4, except that the cirrus shape error is based on the cirrus forcing from the *modified* parameterizations compared to that of the new parameterizations.

function transmission when compared to the corresponding Fu 2007 parameterizations, as shown in Figure 3.20 through Figure 3.25. Still, the modified parameterization can provide accuracy within 12% for CS and 32% for TC, which may be sufficiently accurate for some applications. The primary advantage of the modified parameterizations is that they do not require the use of a different set of parameterizations for each shape like the new parameterizations and can therefore be applied to any shape, provided that the aspect ratio is known. This is a much easier parameterization to implement. Also, it is more flexible since other shapes can be modeled as long as their aspect ratio is known.

Figure 4.6 shows the net infrared flux density cirrus shape error for both cloud cases. The comparison of results using the original parameterization to the new parameterization (New: none) shows errors less than 18% for CS and 38% for TC, although errors are within 21% for all shapes except aggregates. By using the new parameterization for β_e (New: β_e), the error drops to under 14% for CS and to less than 26% for TC. By using the new parameterization for β_a (New: β_a), the error drops to less than 7% for CS and 12% for TC. By using the new parameterizations for both β_e and β_a (New: β_e, β_a), both the CS and TC results are within ±5% of the new parameterization results. This shows a strong shape-dependence on the infrared absorption coefficient and, to a lesser extent, on the infrared extinction coefficient.

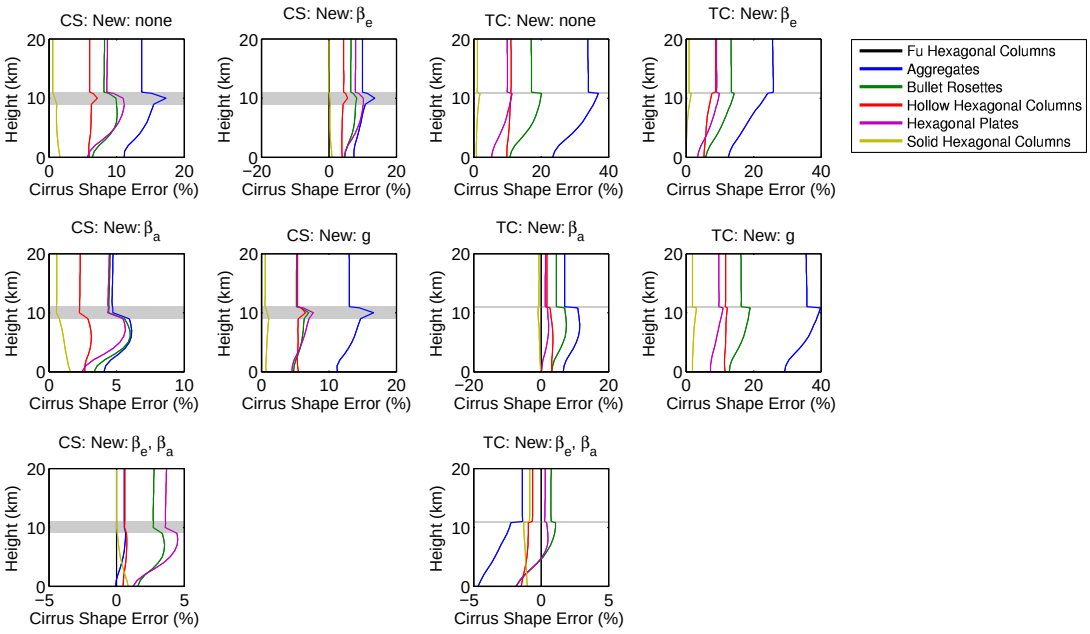

Figure 4.6: Net infrared flux density cirrus shape error: original-to-new comparison
Same as Figure 4.4, except that the cirrus shape error is based on net *infrared* flux density cirrus forcing.

Now, the cirrus shape error based on heating rate forcing by cirrus is examined. Figure 4.7 shows the same solar original-to-new parameterization comparison test as Figure 4.4, but in terms of the heating rate forcing. Before interpreting these results, it is important to remember that cirrus forcing in terms of heating rate outside of the clouds was nearly zero. Therefore, large percentage errors outside of the cloud do not correspond to large absolute changes in heating rate. It is for this reason that the results discussion will concentrate on errors within the cloud. The cirrus shape error within the cloud for the comparison of the original and new parameterizations (New: none) is between -3% and 16% for CS and -5% to 17% for TC. The use of the new parameterization for β_e (New: β_e) results in roughly similar error values. The use of the new co-albedo (New: ω) results in a decreased error of -2% to 4% for CS and -2% to 2% for TC. The use of the new asymmetry factor (New: g) results in a marginal decrease in the error to 1% to 14% for CS and 4% to17% for TC. The use of the new delta-function transmission (New: f_δ) resulted in marginal decreases in the error to -3% to 14% for CS and 4% to 17% for TC. The combined

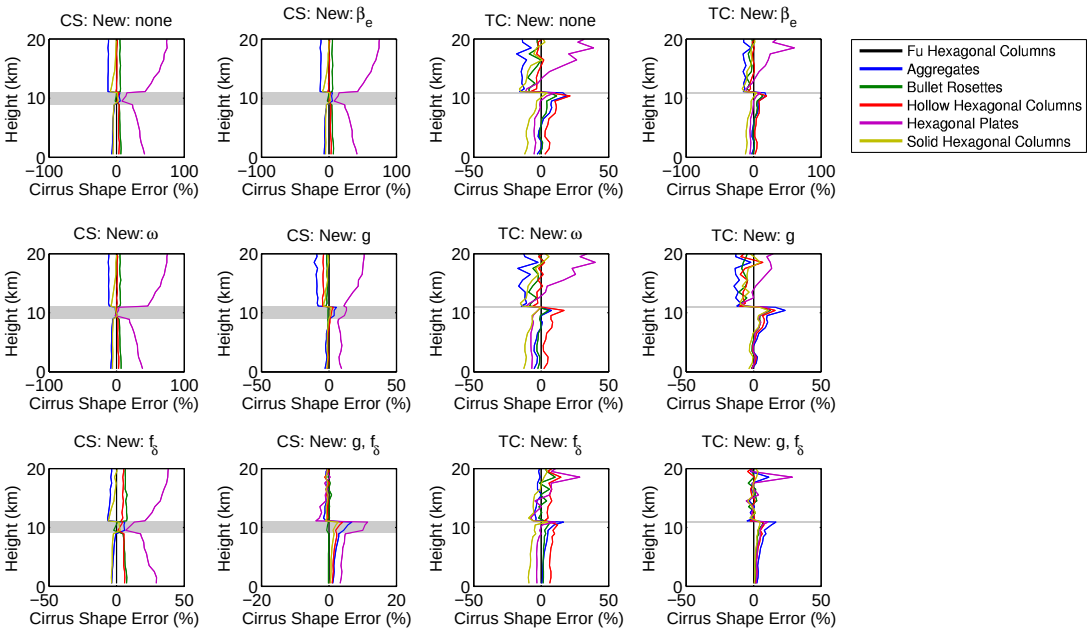

Figure 4.7: Solar heating rate cirrus shape error: original-to-new comparison
Same as Figure 4.4, except that the cirrus shape error is based on solar *heating rate* cirrus forcing.

use of the new g and f_δ (New: g, f_δ) resulted in errors ranging between -1% and 12% for CS and 4 and 17% for TC. Co-albedo seems to be the most shape-dependent SSP, especially for the TC case.

Figure 4.8 shows the same solar modified-to-new parameterization comparison test as Figure 4.5, but in terms of the heating rate. The cirrus shape error when comparing the modified and new parameterizations within the clouds ranges from -2% to 12% for CS and 5 to 17% for TC. The results are identical when using the new parameterization extinction coefficient (New: β_e). However, when using the new parameterization co-albedo (New: ω), the error within the cloud decreases to -3% to 2% for CS and -2% to 2% for TC. Again, the co-albedo is the most shape-dependent SSP for cirrus shape error in terms of heating rate.

Figure 4.9 shows the same infrared original-to-new parameterization comparison test as Figure 4.6, but in terms of the heating rate. The cirrus shape error when comparing the original and new parameterizations (New: none) within the clouds ranges from 10% to 860% for CS, the extreme outliner being the aggregate

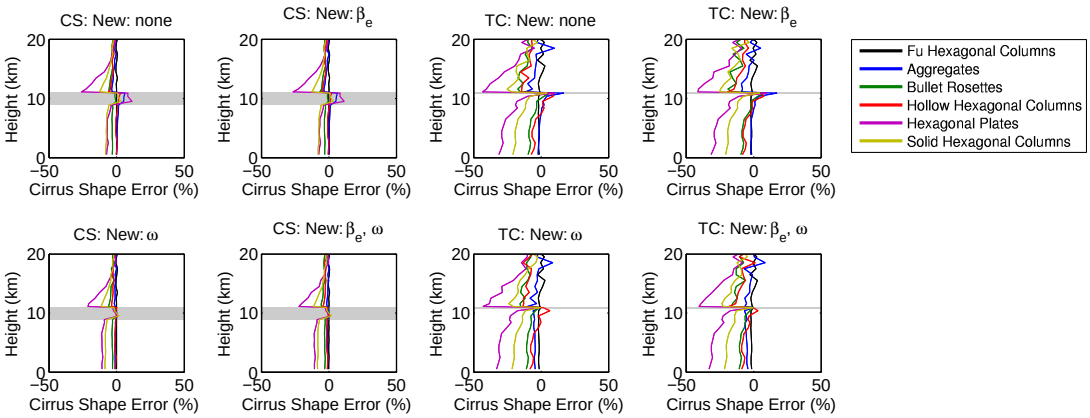

Figure 4.8: Solar heating rate cirrus shape error: modified-to-new comparison
Same as Figure 4.5, except that the cirrus shape error is based on solar *heating rate* cirrus forcing.

shape, and 7% to 29% for TC. The use of either the new extinction coefficient (New: β_e) or new asymmetry factor (New: g) results in hardly any error difference. The use of the new absorption coefficient (New: β_a) results in an error of -3% to 8% for CS and -0.7% to -0.1% for TC. When combining the use of the new β_e and β_a (New: β_e, β_a), the errors range from -4% to 1% for CS and from -0.1 to 0.4% for TC. As with cirrus shape error based on flux density, there is a strong shape-dependence on the infrared absorption coefficient and, to a lesser extent, on the infrared extinction coefficient.

4.5. Discussion

The most shape-dependent solar SSPs on cirrus forcing flux density results are the asymmetry factor, followed by the delta-function transmission. The use of both SSPs results in a nonlinear error reduction. For solar cirrus forcing in terms of heating rate, the strongest shape-dependence was on co-albedo. Based on the definition of heating rate, this was a test on the dependence of the change of flux density with height, not on the flux density itself. It is therefore reasonable that a different shape dependence occurred for heating rate results. The most shape-dependent infrared SSPs are the absorption coefficient, followed by the extinction coefficient. The use of both SSPs results in a nonlinear error reduction. Both flux density and heating rate

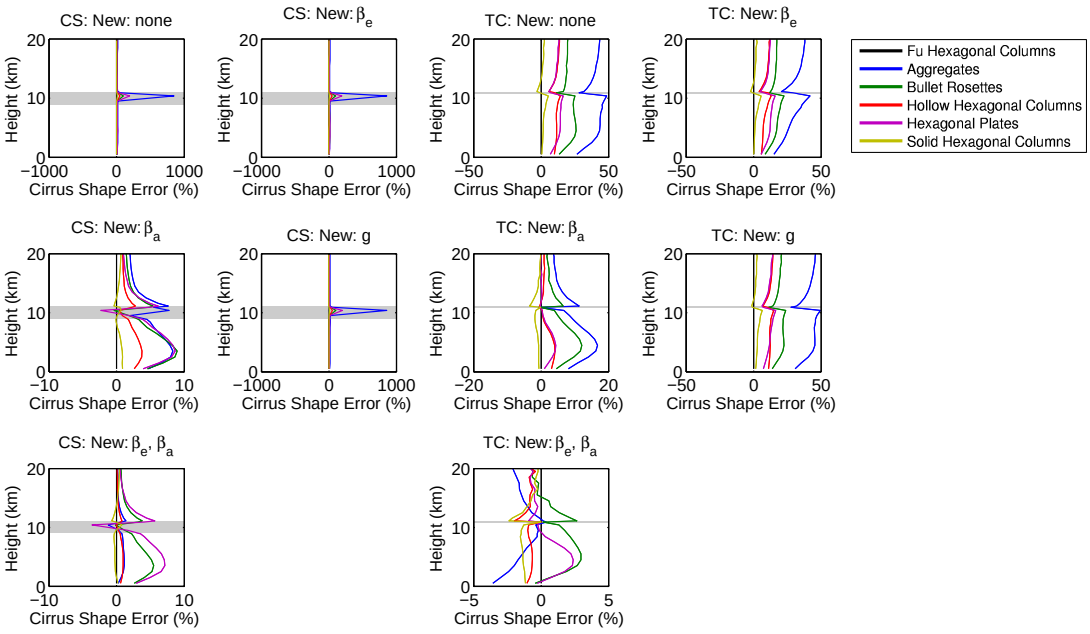

Figure 4.9: Infrared heating rate cirrus shape error: original-to-new comparison
Same as Figure 4.6, except that the cirrus shape error is based on infrared *heating rate* cirrus forcing.

cirrus shape errors adhered to this shape-dependence. It is important to explore why these shape dependencies exist.

Table 4.1 shows the surface (SFC) and top-of-the-atmosphere (TOA) cirrus shape error in terms of net solar flux density cirrus forcing for the CS case. The top part contains the original-to-new comparison results from Figure 4.4 and the bottom part contains the modified-to-new comparison results from Figure 4.5. Along with showing relative cirrus shape error, this table shows the actual differences in flux density cirrus forcing. Table 4.2 shows the same results, except for the TC scenario.

The Fu (1996) parameterization (shown as "Fu. Hex." in the table) results in an error of zero in the original-to-new comparisons because it is part of the new parameterizations. As was apparent in the solar original-to-new comparison of Figure 4.4, the tests of "New: none", "New: β_e", and "New: ω" yielded similar error results. For these tests, the largest error was for hexagonal plates at -13.6 to -16.5 W m^{-2} (66.4% to 84.2%) for CS and -0.2 to -0.3 W m^{-2} (4.5% to 10.8%). When looking at solar bands 1 and 2 (Figure 3.1 and Figure 3.2) of the test parameterizations, it is

obvious why. The asymmetry factor and delta-function transmission values are much different than for the Fu (1996) parameterization. This difference is also larger at a D_{ge} of 40 μm than at 15 μm so it explains the larger error for CS than for TC.

In contrast to the hexagonal plate shape, the solid and hollow hexagonal

Table 4.1: Net solar flux density cirrus shape error for the CS case
Surface (SFC) and top-of-the-atmosphere (TOA) cirrus shape error based on net solar flux density cirrus forcing for the CS cloud case. The first value is the absolute forcing in W m^{-2} and the value in parentheses is the relative forcing, which was shown in the Figure 4.4 and Figure 4.5. The SSPs indicated by "New" are from the new parameterizations, while the rest are from either the original parameterizations (Data from Figure 4.4) as shown in the top half of the table or from the modified parameterizations (Data from Figure 4.5) as shown in the bottom half.

	Fu Hex.	Aggr.	B. Ros.	H. Hex.	Plates	S. Hex.
CS Original (Data from Figure 4.4)						
New: none (SFC)	0.00E+00 (0.00E+00%)	3.47E+00 (-9.15E+00%)	-2.96E+00 (9.38E+00%)	-1.75E+00 (5.33E+00%)	-1.40E+01 (6.81E+01%)	1.03E+00 (-2.91E+00%)
New: none (TOA)	0.00E+00 (0.00E+00%)	4.82E+00 (-1.19E+01%)	-3.86E+00 (1.21E+01%)	-2.00E+00 (5.93E+00%)	-1.61E+01 (8.19E+01%)	1.98E+00 (-5.24E+00%)
New: β_e (SFC)	0.00E+00 (0.00E+00%)	3.38E+00 (-8.90E+00%)	-2.93E+00 (9.29E+00%)	-1.76E+00 (5.38E+00%)	-1.40E+01 (6.80E+01%)	9.28E-01 (-2.61E+00%)
New: β_e (TOA)	0.00E+00 (0.00E+00%)	4.75E+00 (-1.17E+01%)	-3.83E+00 (1.20E+01%)	-2.02E+00 (6.00E+00%)	-1.61E+01 (8.18E+01%)	1.87E+00 (-4.95E+00%)
New: ω (SFC)	0.00E+00 (0.00E+00%)	3.65E+00 (-9.62E+00%)	-2.97E+00 (9.43E+00%)	-1.68E+00 (5.13E+00%)	-1.36E+01 (6.64E+01%)	1.08E+00 (-3.05E+00%)
New: ω (TOA)	0.00E+00 (0.00E+00%)	4.62E+00 (-1.14E+01%)	-3.81E+00 (1.20E+01%)	-2.07E+00 (6.14E+00%)	-1.65E+01 (8.42E+01%)	1.92E+00 (-5.09E+00%)
New: g (SFC)	0.00E+00 (0.00E+00%)	1.60E+00 (-4.21E+00%)	2.46E-01 (-7.79E-01%)	6.70E-01 (-2.05E+00%)	-2.47E+00 (1.21E+01%)	4.02E-01 (-1.13E+00%)
New: g (TOA)	0.00E+00 (0.00E+00%)	2.31E+00 (-5.69E+00%)	2.51E-01 (-7.87E-01%)	9.76E-01 (-2.89E+00%)	-1.86E+00 (9.47E+00%)	6.95E-01 (-1.84E+00%)
New: f_δ (SFC)	0.00E+00 (0.00E+00%)	1.94E+00 (-5.11E+00%)	-3.26E+00 (1.03E+01%)	-2.56E+00 (7.83E+00%)	-9.94E+00 (4.84E+01%)	7.17E-01 (-2.02E+00%)
New: f_δ (TOA)	0.00E+00 (0.00E+00%)	3.00E+00 (-7.40E+00%)	-4.23E+00 (1.33E+01%)	-3.00E+00 (8.90E+00%)	-1.14E+01 (5.79E+01%)	1.51E+00 (-4.00E+00%)
New: g, f_δ (SFC)	0.00E+00 (0.00E+00%)	-7.55E-02 (1.99E-01%)	-9.41E-03 (2.98E-02%)	-5.12E-02 (1.56E-01%)	-3.74E-01 (1.82E+00%)	5.79E-02 (-1.63E-01%)
New: g, f_δ (TOA)	0.00E+00 (0.00E+00%)	2.92E-01 (-7.21E-01%)	-5.44E-02 (1.71E-01%)	1.00E-01 (-2.97E-01%)	3.96E-01 (-2.02E+00%)	1.69E-01 (-4.48E-01%)
CS Modified (Data from Figure 4.5)						
New: none (SFC)	-1.85E-02 (5.35E-02%)	4.50E-02 (-1.19E-01%)	7.21E-01 (-2.28E+00%)	-2.91E-01 (8.89E-01%)	8.96E-01 (-4.37E+00%)	2.24E+00 (-6.29E+00%)
New: none (TOA)	-2.09E-02 (5.85E-02%)	6.28E-01 (-1.55E+00%)	1.02E+00 (-3.21E+00%)	-5.51E-02 (1.63E-01%)	2.69E+00 (-1.37E+01%)	3.58E+00 (-9.50E+00%)
New: β_e (SFC)	-1.85E-02 (5.35E-02%)	-5.46E-02 (1.44E-01%)	7.46E-01 (-2.36E+00%)	-3.07E-01 (9.37E-01%)	9.08E-01 (-4.42E+00%)	2.13E+00 (-6.00E+00%)
New: β_e (TOA)	-2.09E-02 (5.85E-02%)	5.54E-01 (-1.37E+00%)	1.04E+00 (-3.28E+00%)	-8.17E-02 (2.42E-01%)	2.70E+00 (-1.38E+01%)	3.48E+00 (-9.22E+00%)
New: ω (SFC)	-1.85E-02 (5.35E-02%)	2.05E-01 (-5.39E-01%)	7.03E-01 (-2.23E+00%)	-2.32E-01 (7.08E-01%)	1.26E+00 (-6.12E+00%)	2.28E+00 (-6.42E+00%)
New: ω (TOA)	-2.09E-02 (5.85E-02%)	3.66E-01 (-9.03E-01%)	1.05E+00 (-3.30E+00%)	-1.52E-01 (4.49E-01%)	2.29E+00 (-1.17E+01%)	3.50E+00 (-9.29E+00%)
New: β_e, ω (SFC)	-1.85E-02 (5.35E-02%)	1.06E-01 (-2.79E-01%)	7.28E-01 (-2.31E+00%)	-2.48E-01 (7.56E-01%)	1.27E+00 (-6.18E+00%)	2.18E+00 (-6.13E+00%)
New: β_e, ω (TOA)	-2.09E-02 (5.85E-02%)	2.91E-01 (-7.16E-01%)	1.07E+00 (-3.37E+00%)	-1.81E-01 (5.38E-01%)	2.30E+00 (-1.17E+01%)	3.40E+00 (-9.01E+00%)

columns have errors ranging from 0.9 to -2.1 (-2.6% to 6.1%) for CS and 0.2 to 0.4 W m^{-2} (-1.0% to -10.0%). Their asymmetry factor and delta-function transmission values are the closest match to the Fu (1996) parameterization. This is not surprising since all three parameterizations share very similar shape definitions. The difference also happens to be smaller at a D_{ge} of 40 μm than at 15 μm, which explains the larger upper limit of error for the TC case. The remaining shapes have asymmetry factor and delta-function transmission parameterizations that exist between these two extremes and so

Table 4.2: Net solar flux density cirrus shape error for the TC case
Same as Table 4.1, except for the TC cloud case.

	Fu Hex.	Aggr.	B. Ros.	H. Hex.	Plates	S. Hex.
TC Original (Data from Figure 4.4)						
New: none (SFC)	0.00E+00 (0.00E+00%)	2.29E-01 (-6.21E+00%)	-1.28E-03 (3.70E-02%)	-1.76E-01 (5.37E+00%)	-3.38E-01 (1.08E+01%)	2.62E-01 (-7.04E+00%)
New: none (TOA)	0.00E+00 (0.00E+00%)	3.14E-01 (-7.32E+00%)	3.82E-02 (-9.51E-01%)	-2.03E-01 (5.38E+00%)	-1.75E-01 (4.61E+00%)	4.42E-01 (-1.00E+01%)
New: β_e (SFC)	0.00E+00 (0.00E+00%)	2.15E-01 (-5.82E+00%)	7.10E-04 (-2.05E-02%)	-1.81E-01 (5.50E+00%)	-3.34E-01 (1.07E+01%)	2.44E-01 (-6.55E+00%)
New: β_e (TOA)	0.00E+00 (0.00E+00%)	3.07E-01 (-7.16E+00%)	4.42E-02 (-1.10E+00%)	-2.07E-01 (5.48E+00%)	-1.70E-01 (4.48E+00%)	4.25E-01 (-9.61E+00%)
New: ω (SFC)	0.00E+00 (0.00E+00%)	2.58E-01 (-6.99E+00%)	1.21E-02 (-3.50E-01%)	-1.68E-01 (5.11E+00%)	-3.21E-01 (1.03E+01%)	2.69E-01 (-7.23E+00%)
New: ω (TOA)	0.00E+00 (0.00E+00%)	2.82E-01 (-6.56E+00%)	2.27E-02 (-5.66E-01%)	-2.12E-01 (5.62E+00%)	-1.95E-01 (5.13E+00%)	4.35E-01 (-9.83E+00%)
New: g (SFC)	0.00E+00 (0.00E+00%)	2.00E-01 (-5.42E+00%)	9.82E-02 (-2.84E+00%)	1.17E-01 (-3.57E+00%)	-4.78E-02 (1.53E+00%)	1.35E-01 (-3.62E+00%)
New: g (TOA)	0.00E+00 (0.00E+00%)	2.58E-01 (-6.01E+00%)	1.32E-01 (-3.29E+00%)	1.41E-01 (-3.73E+00%)	2.23E-02 (-5.87E-01%)	1.76E-01 (-3.99E+00%)
New: f_δ (SFC)	0.00E+00 (0.00E+00%)	1.90E-02 (-5.16E-01%)	-1.20E-01 (3.48E+00%)	-3.20E-01 (9.74E+00%)	-2.52E-01 (8.07E+00%)	1.64E-01 (-4.41E+00%)
New: f_δ (TOA)	0.00E+00 (0.00E+00%)	1.05E-01 (-2.45E+00%)	-8.78E-02 (2.18E+00%)	-3.55E-01 (9.40E+00%)	-1.21E-01 (3.19E+00%)	3.29E-01 (-7.44E+00%)
New: g, f_δ (SFC)	0.00E+00 (0.00E+00%)	-1.39E-02 (3.76E-01%)	-1.54E-02 (4.45E-01%)	-4.93E-03 (1.50E-01%)	-2.10E-02 (6.72E-01%)	1.23E-02 (-3.29E-01%)
New: g, f_δ (TOA)	0.00E+00 (0.00E+00%)	4.15E-02 (-9.66E-01%)	9.77E-03 (-2.43E-01%)	8.54E-03 (-2.26E-01%)	1.95E-02 (-5.14E-01%)	2.55E-02 (-5.77E-01%)
TC Modified (Data from Figure 4.5)						
New: none (SFC)	3.10E-02 (-8.94E-01%)	5.73E-02 (-1.55E+00%)	2.98E-01 (-8.61E+00%)	1.76E-01 (-5.35E+00%)	7.57E-01 (-2.42E+01%)	6.10E-01 (-1.64E+01%)
New: none (TOA)	5.25E-02 (-1.32E+00%)	1.91E-01 (-4.45E+00%)	4.48E-01 (-1.12E+01%)	2.77E-01 (-7.34E+00%)	1.23E+00 (-3.22E+01%)	9.18E-01 (-2.08E+01%)
New: β_e (SFC)	3.10E-02 (-8.94E-01%)	4.22E-02 (-1.14E+00%)	3.00E-01 (-8.66E+00%)	1.72E-01 (-5.24E+00%)	7.60E-01 (-2.43E+01%)	5.94E-01 (-1.59E+01%)
New: β_e (TOA)	5.25E-02 (-1.32E+00%)	1.83E-01 (-4.26E+00%)	4.54E-01 (-1.13E+01%)	2.77E-01 (-7.34E+00%)	1.22E+00 (-3.22E+01%)	9.00E-01 (-2.04E+01%)
New: ω (SFC)	3.10E-02 (-8.94E-01%)	8.34E-02 (-2.26E+00%)	3.10E-01 (-8.95E+00%)	1.84E-01 (-5.58E+00%)	7.73E-01 (-2.47E+01%)	6.17E-01 (-1.66E+01%)
New: ω (TOA)	5.25E-02 (-1.32E+00%)	1.49E-01 (-3.46E+00%)	4.28E-01 (-1.07E+01%)	2.65E-01 (-7.01E+00%)	1.21E+00 (-3.17E+01%)	9.07E-01 (-2.05E+01%)
New: β_e, ω (SFC)	3.10E-02 (-8.94E-01%)	6.89E-02 (-1.87E+00%)	3.12E-01 (-9.00E+00%)	1.80E-01 (-5.47E+00%)	7.76E-01 (-2.48E+01%)	6.00E-01 (-1.61E+01%)
New: β_e, ω (TOA)	5.25E-02 (-1.32E+00%)	1.40E-01 (-3.26E+00%)	4.33E-01 (-1.08E+01%)	2.64E-01 (-6.99E+00%)	1.20E+00 (-3.17E+01%)	8.89E-01 (-2.01E+01%)

too do their errors. When it is assumed that the Fu (1996) parameterization is sufficient for calculating SSP for a given shape, the accuracy is based upon the closeness of the individual shape parameterization to that of Fu (1996). Using only the original parameterizations, the absolute value of solar cirrus forcing error is approximately at or below 4.9 W m^{-2} (12%) for aggregates, 3.9 W m^{-2} (12%) for bullet rosettes, 2.1 W m^{-2} (7%) for hollow hexagonal columns, 17 W m^{-2} (85%) for hexagonal plates, and 2.0 W m^{-2} (6%) for solid hexagonal columns. This is the simplest set of parameterizations, but also the least accurate. However, errors are at or below 12% for all shapes except hexagonal plates.

When the hexagonal plate results are modeled using the hexagonal plate asymmetry factor (New: g), the error drops to -1.9 to -2.5 W m^{-2} (9.5% to 12.1%) for CS and -0.1 to -0.3 W m^{-2} (3.2% to 8.1%) for TC, which is a large improvement, especially for the CS case where errors were as high as 84%. The solid and hollow hexagonal column error drops to 0.4 to 1.0 W m^{-2} (-1.1% to -2.9%) for CS and 0.4 to 1.0 W m^{-2} (-1.1% to -2.9%) for TC, which is a more modest improvement over errors that originally did not exceed 10%.

The error decrease is not as large in the "New: f_δ" case. Recall that the delta-function transmission augments the accuracy of the asymmetry factor, which is especially necessary for smooth particles due to the large forward peaks in their phase functions. It is less effective when it is being used with an asymmetry factor derived from a different shape. That is why the "New: g, f_δ" test provides such accurate results. Using the new parameterizations for these two SSPs and the original parameterizations for all the rest, the absolute value of error is approximately at or below 0.3 (1.0%) for aggregates, 0.0 W m^{-2} (0.2%) for bullet rosettes, 0.1 W m^{-2} (0.3%) for hollow hexagonal columns, 0.4 W m^{-2} (2.0%) for hexagonal plates, and 0.2 W m^{-2} (0.6%) for solid hexagonal columns. This is the optimal combination of original and new parameterizations for solar that provides good accuracy, yet uses the fewest new SSPs possible.

As was apparent in the modified-to-new comparison of Figure 4.5, all the tests yielded similar error results for each shape. This is because the asymmetry factor and delta-function transmission were calculated by the Fu (2007) parameterizations as a function of AR, which varied for each shape. However, this is only effective if the calculated asymmetry factor and delta-function transmission correspond well with the Fu (2007) parameterizations for smooth shapes. Any deviation from the parameterization relationship will introduce error into the modified parameterizations for that shape. The Fu (1996) shape (Fu Hex.) has the smallest error by as much as an order of magnitude compared to the other shapes. This is expected since the asymmetry factor, delta-function transmission, and geometry calculations from Fu (1996) were used to construct the Fu (2007) parameterizations for smooth particles with AR less than 1. This close correspondence can be seen in the band 1 and 2 parameterization plots in Figure 3.20 and Figure 3.21. The aggregate shape also has small cirrus shape error and it corresponds well to the Fu (2007) asymmetry factor parameterization for rough shapes. Overall, the shapes do not match nearly as well to the Fu (2007) delta-function transmission parameterizations, yet it does not seem to create large cirrus shape errors. This again shows that the asymmetry factor is more of a factor in the cirrus shape error accuracy than the delta-function transmission.

The two shapes with the highest modified-to-new cirrus shape error are the hexagonal plates and the solid hexagonal columns. While a calculation of hexagonal plates aspect ratio was used in Fu (2007) to define the parameterizations for AR greater than 1, it is believed to be different than that calculated in Yang et al. (2000). They correspond well for band 1 asymmetry factor, but much worse for band 2, especially at small AR values less than 10. Figure 3.19 shows that the AR values defined for D_{ge} values of 15 μm and 40 μm are less than 10. The solid hexagonal column shape produces a large error due to the differences in the aspect ratio definition between Fu (1996) and Yang et al. (2000), which was shown in Equations [3.1] and [3.2]. The difference is especially large above an AR of 0.7, which translates to D_{ge} values below 50 μm.

Using only the modified parameterizations, the absolute value of solar cirrus forcing error is approximately at or below 0.6 W m^{-2} (4%) for aggregates, 1.0 W m^{-2} (12%) for bullet rosettes, 0.3 W m^{-2} (8%) for hollow hexagonal columns, 2.7 W m^{-2} (32%) for hexagonal plates, and 3.6 W m^{-2} (21%) for solid hexagonal columns. Since the two most shape-dependent parameterizations are defined by the aspect ratio of their respective shapes, it is no surprise that the errors are smaller than in the original-to-new comparison. Still, the inability for some shapes to match the Fu (2007) parameterization causes errors that make the modified parameterization less accurate than the new parameterization.

Table 4.3 shows the surface (SFC) and top-of-the-atmosphere (TOA) cirrus shape error in terms of net infrared flux density cirrus forcing for the CS case. Table 4.4 shows the same results, except for the TC scenario. The Fu et al. (1998) parameterization, shown as "Fu. Hex." in the table, results in an error of zero because it is modeled as part of the new parameterizations. As was apparent in the infrared original-to-new comparison of Figure 4.6, the tests of "New: none" and "New: g"

Table 4.3: Net infrared flux density cirrus shape error for the CS case
Surface (SFC) and top-of-the-atmosphere (TOA) cirrus shape error based on net infrared flux density cirrus forcing for the CS cloud case. The first value is the absolute forcing in W m^{-2} and the value in parentheses is the relative forcing, which was shown in Figure 4.6. The SSPs indicated by "New" are from the new parameterizations, while the rest are from the original parameterizations.

	Fu Hex.	Aggr.	B. Ros.	H. Hex.	Plates	S. Hex.
New: none (SFC)	0.00E+00 (0.00E+00%)	1.51E+00 (1.11E+01%)	9.09E-01 (6.42E+00%)	8.52E-01 (5.99E+00%)	8.12E-01 (5.70E+00%)	2.43E-01 (1.64E+00%)
New: none (TOA)	0.00E+00 (0.00E+00%)	9.39E+00 (1.37E+01%)	5.97E+00 (8.28E+00%)	4.44E+00 (6.03E+00%)	6.25E+00 (8.71E+00%)	4.60E-01 (5.93E-01%)
New: β_e (SFC)	0.00E+00 (0.00E+00%)	1.01E+00 (7.41E+00%)	6.70E-01 (4.73E+00%)	5.58E-01 (3.92E+00%)	6.45E-01 (4.52E+00%)	1.36E-01 (9.17E-01%)
New: β_e (TOA)	0.00E+00 (0.00E+00%)	6.77E+00 (9.87E+00%)	4.74E+00 (6.58E+00%)	3.22E+00 (4.38E+00%)	5.72E+00 (7.97E+00%)	-2.40E-03 (-3.09E-03%)
New: β_a (SFC)	0.00E+00 (0.00E+00%)	5.53E-01 (4.08E+00%)	4.73E-01 (3.34E+00%)	3.78E-01 (2.66E+00%)	3.49E-01 (2.45E+00%)	2.36E-01 (1.59E+00%)
New: β_a (TOA)	0.00E+00 (0.00E+00%)	3.29E+00 (4.79E+00%)	3.30E+00 (4.58E+00%)	1.72E+00 (2.34E+00%)	3.25E+00 (4.53E+00%)	4.56E-01 (5.88E-01%)
New: g (SFC)	0.00E+00 (0.00E+00%)	1.52E+00 (1.13E+01%)	6.75E-01 (4.77E+00%)	7.80E-01 (5.49E+00%)	6.46E-01 (4.53E+00%)	1.03E-01 (6.94E-01%)
New: g (TOA)	0.00E+00 (0.00E+00%)	8.91E+00 (1.30E+01%)	3.77E+00 (5.23E+00%)	3.94E+00 (5.35E+00%)	3.79E+00 (5.28E+00%)	4.56E-01 (5.88E-01%)
New: β_e, βa (SFC)	0.00E+00 (0.00E+00%)	-1.00E-02 (-7.38E-02%)	2.22E-01 (1.57E+00%)	6.85E-02 (4.82E-01%)	1.74E-01 (1.22E+00%)	1.29E-01 (8.68E-01%)
New: β_e, βa (TOA)	0.00E+00 (0.00E+00%)	3.99E-01 (5.81E-01%)	2.02E+00 (2.81E+00%)	4.63E-01 (6.29E-01%)	2.69E+00 (3.75E+00%)	-7.10E-03 (-9.15E-03%)

yielded similar error results in the CS case, while "New: g" actually produces worse results than "New: none" for the TC case. For the "New: none" test, the largest error was for aggregates at 1.5 to 9.4 W m^{-2} (11.1% to 13.7%) for CS and 0.3 to 2.7 W m^{-2} (23.4% to 33.7%). Several infrared bands (Figure 3.7 through Figure 3.18) of the test parameterizations show that the aggregate extinction and absorption coefficients are much different than the Fu et al. (1998) parameterizations.

In contrast to the aggregate shape, the solid hexagonal columns have errors ranging from 0.2 to 0.5 (0.6% to 1.6%) for CS and 0.0 to 0.1 W m^{-2} (0.9% to 1.1%) for TC. Its absorption and extinction coefficients match well with the Fu et al. (1998) parameterizations. Using only the original parameterizations, the absolute value of infrared cirrus forcing error is approximately at or below 9.4 W m^{-2} (34%) for aggregates, 6.0 W m^{-2} (18%) for bullet rosettes, 4.4 W m^{-2} (12%) for hollow hexagonal columns, 6.3 W m^{-2} (10%) for hexagonal plates, and 0.5 W m^{-2} (2%) for solid hexagonal columns. As is the case with the solar test, this is the simplest set of parameterizations, but also the least accurate. However, all errors remain at or below 35% for all shapes.

The use of the new parameterization absorption coefficient (New: β_a) has

Table 4.4: Net infrared flux density cirrus shape error for the TC case
Same as Table 4.3, except for the TC cloud case.

	Fu Hex.	Aggr.	B. Ros.	H. Hex.	Plates	S. Hex.
New: none (SFC)	0.00E+00 (0.00E+00%)	3.30E-01 (2.34E+01%)	1.68E-01 (1.07E+01%)	1.56E-01 (9.86E+00%)	8.75E-02 (5.29E+00%)	1.54E-02 (8.93E-01%)
New: none (TOA)	0.00E+00 (0.00E+00%)	2.70E+00 (3.37E+01%)	1.56E+00 (1.71E+01%)	1.07E+00 (1.11E+01%)	9.69E-01 (9.93E+00%)	1.18E-01 (1.11E+00%)
New: β_e (SFC)	0.00E+00 (0.00E+00%)	1.76E-01 (1.25E+01%)	9.09E-02 (5.78E+00%)	8.33E-02 (5.26E+00%)	5.56E-02 (3.36E+00%)	1.00E-04 (5.80E-03%)
New: β_e (TOA)	0.00E+00 (0.00E+00%)	2.04E+00 (2.54E+01%)	1.22E+00 (1.33E+01%)	8.39E-01 (8.69E+00%)	8.75E-01 (8.97E+00%)	9.18E-02 (8.66E-01%)
New: β_a (SFC)	0.00E+00 (0.00E+00%)	9.21E-02 (6.53E+00%)	4.91E-02 (3.12E+00%)	5.02E-02 (3.17E+00%)	1.50E-03 (9.07E-02%)	-2.20E-03 (-1.28E-01%)
New: β_a (TOA)	0.00E+00 (0.00E+00%)	5.66E-01 (7.06E+00%)	4.22E-01 (4.61E+00%)	1.71E-01 (1.77E+00%)	1.27E-01 (1.30E+00%)	-6.42E-02 (-6.05E-01%)
New: g (SFC)	0.00E+00 (0.00E+00%)	4.12E-01 (2.92E+01%)	2.02E-01 (1.28E+01%)	1.83E-01 (1.15E+01%)	1.20E-01 (7.26E+00%)	3.34E-02 (1.94E+00%)
New: g (TOA)	0.00E+00 (0.00E+00%)	2.84E+00 (3.54E+01%)	1.48E+00 (1.62E+01%)	1.13E+00 (1.17E+01%)	9.37E-01 (9.61E+00%)	2.03E-01 (1.92E+00%)
New: β_e, β_a (SFC)	0.00E+00 (0.00E+00%)	-6.59E-02 (-4.67E+00%)	-2.90E-02 (-1.84E+00%)	-2.34E-02 (-1.48E+00%)	-3.08E-02 (-1.86E+00%)	-1.76E-02 (-1.02E+00%)
New: β_e, β_a (TOA)	0.00E+00 (0.00E+00%)	-1.11E-01 (-1.39E+00%)	7.06E-02 (7.71E-01%)	-5.93E-02 (-6.14E-01%)	3.22E-02 (3.30E-01%)	-9.04E-02 (-8.53E-01%)

proven to be the most effective SSP at decreasing the cirrus shape error in the infrared. It decreases the aggregate shape error to 0.6 to 3.3 (4.1% to 4.7%) for CS and 0.1 to 0.6 W m^{-2} (6.5% to 7.1%) for TC. However, it is the combination of the new parameterization absorption and extinction coefficients (New: β_e, β_a) that reduces the error the most. Using the new parameterizations for these two SSPs and the original parameterizations for all the rest, the absolute value of error is approximately at or below 0.4 W m^{-2} (5%) for aggregates, 2.0 W m^{-2} (3%) for bullet rosettes, 0.0 W m^{-2} (2%) for hollow hexagonal columns, 2.7 W m^{-2} (4%) for hexagonal plates, and 0.1 W m^{-2} (1%) for solid hexagonal columns. This is the optimal combination of original and new parameterizations for infrared that provides good accuracy, yet uses the fewest new SSPs possible.

CHAPTER 5: CONCLUSION

Within this study, the most accurate simulation of cirrus forcing is accomplished with the new parameterizations. The single-scattering properties (SSPs) are derived explicitly from aggregate, bullet rosette, hollow hexagonal columns, hexagonal plates, and solid hexagonal columns. The obvious trade-off is the need for SSP parameterizations for each shape, which can be too complicated for some applications. It also restricts the simulations to the pre-existing five shapes or requires the development of additional parameterizations for other shapes.

The original parameterizations are the least accurate, especially for hexagonal plates in the solar bands and aggregates in the infrared bands. However, solar cirrus shape error can be significantly reduced by using the asymmetry factor or the asymmetry factor and delta-function transmission from the new parameterizations. Similarly, the infrared cirrus shape error can be significantly reduced by using the absorption coefficient or the absorption and extinction coefficients from the new parameterizations. Depending on the configuration chosen, anywhere from one to four SSPs would still require parameterizations for each shape and the simulations would still be restricted to the pre-existing five shapes. However, it would be a little less complicated than using all SSPs from the new parameterization.

The modified parameterizations offer improved solar accuracy over the original parameterizations for aggregates and hexagonal plates, similar accuracy as the original for bullet rosettes and hollow hexagonal columns, and worse accuracy than the original for solid hexagonal columns. The poor correspondence of the solid hexagonal shapes is due to the difference in aspect ratio definition between it and the Fu solid hexagonal columns. The advantage of this parameterization scheme is that it is nearly as simple as the original parameterizations, but it does partially model the differences due to particle shape. Best of all, new shapes can be used simply by constructing new parameterizations that calculate AR as a function of D_{ge}.

There is certainly more work that could be done on this topic. The modified parameterizations show great potential in modeling multiple ice particle shapes, but in its current state, the solar error is larger than when using the original parameterizations with the asymmetry factor and delta-function transmission from the new parameterizations. It would be useful to explore the reasoning behind the differences between the Fu (2007) parameterization and the shape calculations from Yang et al. (2000), especially for hexagonal plates and solid hexagonal columns. An alteration of either the original geometry definitions or the Fu (2007) parameterizations could significantly reduce this error.

The feasibility of developing a parameterization of infrared extinction and absorption coefficients as a function of AR or some other shape parameter should be explored. If such a relationship exists, then the infrared error could be reduced, while not being forced to use different parameterizations for each shape. A shape-independent parameterization that only requires inputs of D_{ge}, IWC, and AR would be the best possible outcome, provided it is accurate. It would be simple and more easily allow different shapes to be used in future cirrus simulations.

REFERENCES

Anderson, G.P., J.H. Chetwynd, S.A. Clough, E.P. Shettle, F.X. Kneizys, 1986: AFGL atmospheric constituent profiles (0-120km). *Environmental Research Papers, 954, Air Force Geophysics Laboratory*.

Fu, Q., 1991: Parameterization of radiative processes in vertically nonhomogeneous multiple scattering atmospheres. Ph.D. dissertation, University of Utah, 259 pp.

Fu, Q., and K.N. Liou, 1992: On the correlated k-distribution method for radiative transfer in nonhomogeneous atmospheres. *J. Atmos. Sci.*, 49, 2139-2156.

Fu, Q., and K.N. Liou, 1993: Parameterization of the radiative properties of cirrus clouds. *J. Atmos. Sci.*, 50, 2008-2025.

Fu, Q., 1996: An accurate parameterization of the solar radiative properties of cirrus clouds for climate models. *J. Climate*, 9, 2058–2082.

Fu, Q., P. Yang, W.B. Sun, 1998: An accurate parameterization of the infrared radiative properties of cirrus clouds for climate models. *J. Climate*, 11, 2223-2237.

Fu, Q., 2007: Generalized parameterization of asymmetry factor of cirrus clouds for climate models. *J. Atmos. Sci.* (accepted).

Gosse, S., D. Labrie, and P. Chylek, 1995: Refractive index of ice in the 1.4 to 7.8 μm spectral range. *Appl. Opt.*, 34, 6582-6586.

Heymsfield, A.J., 1975: Cirrus uncinus generating cells and the evolution of cirriform clouds. J. Atmos. Sci., 32, 799-808.

Liou, K.N., 1986: Influence of cirrus clouds on weather and climate processes: A global perspective. *Mon. Wea. Rev.*, 114, 1167-1199.

Liou, K.N., Q. Fu, and T.P. Ackerman, 1988: A simple formulation of the delta-four-stream approximation for radiative transfer parameterizations. *J. Atmos. Sci.*, 45, 1940-1947.

Liou, K.N., 2002: *An Introduction to Atmospheric Radiation Second Edition*. Academic Press, 583 pp.

Mitchell, D.L., and W.P. Arnott, 1994: A model predicting the evolution of ice particle size spectra and radiative properties of cirrus clouds. Part II: Dependence of absorption and extinction on ice crystal morphology. *J. Atmos. Sci.*, 51, 817-832.

Mitchell, D.L., 2002: Effective diameter in radiation transfer: General definition, applications, and limitations. *J. Atmos. Sci.*, 59, 2330-2346.

Pruppacher, H.R., and J.D. Klett, 1978: *Microphysics of clouds and precipitation*. D. Reidel, Boston, Mass, 714 pp.

Robinson, S.S., and Q. Fu, 2006: *Parameterization of Infrared Radiative Properties of Cirrus Containing Small Ice Particles: Task III Report to Boeing, Version 2*.

Stephens, G.L., S.-C. Tsay, P.W. Stackhouse, Jr., P.J. Flatau, 1990: The relevance of the microphysical and radiative properties of cirrus clouds to climate and climate feedback. *J. Atmos. Sci.*, 47, 1742-1753.

Warren, S.G., 1984: Optical constants of ice from the ultraviolet to the microwave. *Appl. Opt.*, 23, 1206-1225.

Wendisch, M., P. Pilewskie, J. Pommier, S. Howard, P. Yang, A. J. Heymsfield, C. G. Schmitt, D. Baumgardner, and B. Mayer, 2005: Impact of cirrus crystal shape on solar spectral irradiance: A case study for subtropical cirrus. *J. Geophys. Res.*, 110, D03202, doi:10.1029/2004JD005294.

Wendisch, M., P. Yang, P. Pilewskie, 2007 (Submitted): Effects of ice crystal habit on thermal infrared radiative properties and forcing of cirrus. *J. Geophys. Res.*.

Yang, P., and K.N. Liou, 1998: Single-scattering properties of complex ice crystals in terrestrial atmosphere. *Contr. Atmos. Phys.*, 71, 223-248.

Yang, P., K.N. Liou, K. Wyser, and D. Mitchell, 2000: Parameterization of the scattering and absorption properties of individual ice crystals. *J. Geophys. Res.*, 105, 4699-4718.

Yang, P., H. Wei, H.-L. Huang, B.A. Baum, Y.X. Hu, G.W. Kattawar, M.I. Mishchenko, and Q. Fu, 2005: Scattering and absorption property database for nonspherical ice particles in the near- through far-infrared spectral region. *Appl. Opt.*, 44, 5512-5523.

APPENDIX A: ROBINSON AND FU (2006) PARAMETERIZATION COEFFICIENTS

Below are the regression coefficients for each single-scattering property of the small D_{ge} parameterization from Robinson and Fu (2006). The first column shows the Fu-Liou Radiation Model band number, as defined in Table 2.1.

Table A.1: Original parameterization coefficients for β_e*D_{ge}/IWC (small D_{ge})
Coefficients for the infrared extinction coefficient*D_{ge}/IWC small D_{ge} parameterization, Equation [2.41].

#	a_0	a_1	a_2	a_3	a_4
7	-2.005187E+00	1.887870E+00	-2.394987E-01	1.226004E-02	-2.176747E-04
8	-1.221428E+00	1.190519E+00	-1.081918E-01	3.207774E-03	-7.790185E-06
9	-5.522210E-01	5.556264E-01	1.350808E-02	-5.182503E-03	1.854760E-04
10	-2.411192E-01	2.109769E-01	7.588264E-02	-9.103300E-03	2.678349E-04
11	-1.485194E-02	4.630892E-03	8.989527E-02	-8.569112E-03	2.290338E-04
12	4.292661E-02	-7.619363E-04	5.089112E-02	-4.101744E-03	9.917537E-05
13	-1.257657E-03	3.840350E-01	-2.336758E-02	5.263245E-04	9.536367E-07
14	-2.482977E-01	5.149985E-01	-1.086854E-02	-1.909389E-03	8.220600E-05
15	1.130811E-01	-7.663294E-02	9.961269E-02	-8.920452E-03	2.325299E-04
16	1.477471E-01	-1.276555E-01	5.889066E-02	-3.637540E-03	7.242738E-05
17	2.778228E-02	9.410452E-03	7.771632E-03	-1.847559E-05	-7.178001E-06
18	2.954018E-03	1.254725E-01	-3.265442E-03	2.270727E-04	-6.365789E-06

Table A.2: Original parameterization coefficients for β_a*D_{ge}/IWC (small D_{ge})
Coefficients for the infrared absorption coefficient*D_{ge}/IWC small D_{ge} parameterization, Equation [2.42].

#	b_0	b_1	b_2	b_3	b_4
7	-8.768658E-03	8.493330E-02	-3.632126E-03	6.987413E-05	2.703965E-07
8	-7.762272E-03	1.653825E-01	-1.242696E-02	4.813596E-04	-6.987702E-06
9	-1.103846E-02	1.880946E-01	-1.320780E-02	4.530029E-04	-5.384886E-06
10	-1.240034E-02	1.353184E-01	-6.773254E-03	1.353446E-04	4.783046E-07
11	-9.834148E-03	1.045283E-01	-3.714625E-03	9.185834E-06	2.434297E-06
12	-4.989783E-03	9.761852E-02	-3.464011E-03	1.681863E-05	1.990612E-06
13	5.524896E-02	3.828618E-01	-4.868927E-02	2.788080E-03	-5.893696E-05
14	-1.102297E-01	4.983548E-01	-5.947312E-02	3.147713E-03	-6.196981E-05
15	-3.705134E-02	1.612865E-01	-4.132244E-03	-2.863781E-04	1.374847E-05
16	5.730367E-03	3.433887E-02	3.147511E-03	-3.044807E-04	7.929481E-06
17	3.126666E-03	3.533685E-02	5.299923E-04	-6.735890E-05	1.687872E-06
18	9.549627E-03	1.140347E-01	1.223725E-03	-4.282989E-04	1.343652E-05

Table A.3: Original parameterization coefficients for g (small D_{ge})
Coefficients for the infrared asymmetry factor small D_{ge} parameterization, [2.43].

#	c_0	c_1	c_2	c_3	c_4
7	-1.592086E-01	5.165795E-01	-8.889665E-02	6.133364E-03	-1.466832E-04
8	-2.780309E-01	5.589181E-01	-9.294043E-02	6.316572E-03	-1.501642E-04
9	-4.146218E-01	6.015844E-01	-9.714942E-02	6.513667E-03	-1.539503E-04
10	-4.644106E-01	5.861063E-01	-9.087172E-02	5.917403E-03	-1.371181E-04
11	-4.848736E-01	5.552414E-01	-8.183047E-02	5.147920E-03	-1.164374E-04
12	-5.056360E-01	5.240870E-01	-7.278649E-02	4.395703E-03	-9.639759E-05
13	-4.991806E-01	4.601579E-01	-5.805338E-02	3.236112E-03	-6.615910E-05
14	-4.382576E-01	3.812485E-01	-4.268756E-02	2.088357E-03	-3.689533E-05
15	-3.094784E-01	2.406058E-01	-1.477957E-02	2.970087E-05	1.421683E-05
16	-9.731071E-02	4.088258E-02	2.106015E-02	-2.364895E-03	6.892137E-05
17	7.192725E-02	-8.649291E-02	3.621089E-02	-2.888238E-03	7.087982E-05
18	6.792641E-02	-5.575384E-02	1.319878E-02	-4.919461E-04	8.543384E-07

APPENDIX B: NEW PARAMETERIZATION COEFFICIENTS

Below are the regression coefficients for each single-scattering property of the shape-explicit parameterizations from Chapter 3. The first column shows the Fu-Liou Radiation Model band number, as defined in Table 2.1.

Table B.1: New parameterization coefficients for solar $\beta_e * D_{ge}/IWC$
Coefficients for the solar extinction coefficient*D_{ge}/IWC parameterization, Equation [2.26].

	Aggregates	
#	**a_0**	**a_1**
1	-1.221479E-05	2.526803E+00
2	-1.315761E-04	2.539327E+00
3	3.938411E-04	2.466628E+00
4	-6.543706E-04	2.607284E+00
5	3.285796E-04	2.470166E+00
6	-1.142100E-03	2.670826E+00
	Bullet Rosettes	
#	**a_0**	**a_1**
1	-6.622196E-05	2.517402E+00
2	-1.026914E-04	2.525905E+00
3	1.203918E-04	2.510053E+00
4	1.396384E-03	2.441136E+00
5	-9.044611E-04	2.560413E+00
6	-1.265991E-03	2.581517E+00
	Hollow Hexagonal Columns	
#	**a_0**	**a_1**
1	-1.537232E-04	2.531941E+00
2	-1.650199E-04	2.528779E+00
3	2.602851E-04	2.500845E+00
4	3.694898E-04	2.489560E+00
5	1.632094E-03	2.367719E+00
6	-2.674984E-04	2.544728E+00
	Hexagonal Plates	
#	**a_0**	**a_1**
1	-1.982412E-04	2.527507E+00
2	2.940946E-04	2.503624E+00
3	-6.087278E-04	2.554862E+00
4	1.139734E-04	2.504253E+00
5	4.759122E-04	2.468444E+00
6	2.290504E-03	2.392892E+00

	Solid Hexagonal Columns	
#	**a_0**	**a_1**
1	-1.854168E-04	2.538082E+00
2	-2.112206E-04	2.539520E+00
3	1.418997E-04	2.516366E+00
4	-2.119758E-05	2.519440E+00
5	6.128750E-04	2.458676E+00
6	-7.305097E-04	2.590841E+00

Table B.2: New parameterization coefficients for solar 1-ω
Coefficients for the solar single-scattering co-albedo parameterization, Equation [2.27].

	Aggregates			
#	**b_0**	**b_1**	**b_2**	**b_3**
1	-1.699287E-07	9.434425E-08	-2.597443E-11	6.989548E-14
2	-5.904292E-06	2.074792E-05	-6.963391E-09	1.866910E-11
3	-1.302551E-03	1.385106E-03	-4.886602E-06	1.283261E-08
4	-1.875633E-03	2.440072E-03	-1.103619E-05	2.689676E-08
5	2.235512E-01	2.413991E-03	-1.570465E-05	4.052428E-08
6	6.948047E-02	6.968828E-03	-5.062532E-05	1.296363E-07
	Bullet Rosettes			
#	**b_0**	**b_1**	**b_2**	**b_3**
1	-2.675511E-07	1.117245E-07	-3.289326E-10	2.511199E-12
2	-3.383383E-06	2.127277E-05	1.253537E-08	-8.120800E-11
3	-3.791859E-04	1.438235E-03	-6.183462E-06	3.710934E-08
4	1.551406E-03	2.729474E-03	-1.783837E-05	9.845328E-08
5	2.074242E-01	5.003521E-03	-7.101582E-05	4.328209E-07
6	5.035874E-02	1.174586E-02	-1.742915E-04	1.063481E-06
	Hollow Hexagonal Columns			
#	**b_0**	**b_1**	**b_2**	**b_3**
1	-2.859713E-07	1.019446E-07	-1.304386E-10	4.188946E-13
2	2.948255E-06	2.064350E-05	4.770819E-09	-7.255979E-11
3	2.497130E-03	1.175140E-03	-4.736470E-07	-1.142825E-08
4	7.729300E-03	2.139964E-03	-4.721441E-06	-8.843249E-09
5	2.568349E-01	1.637477E-03	-8.344041E-06	1.547735E-08
6	1.235677E-01	6.747023E-03	-5.799019E-05	1.802146E-07
	Hexagonal Plates			
#	**b_0**	**b_1**	**b_2**	**b_3**
1	-8.204181E-08	9.320594E-08	-2.621574E-10	6.564815E-13
2	-2.827315E-06	2.136549E-05	-8.383658E-08	3.886724E-10
3	1.828629E-05	1.362005E-03	-9.421316E-06	3.880879E-08
4	5.397538E-03	2.315133E-03	-1.720595E-05	6.502890E-08
5	2.204155E-01	3.825986E-03	-5.584753E-05	3.309221E-07
6	1.422570E-01	5.343726E-03	-5.560321E-05	2.823297E-07
	Solid Hexagonal Columns			
#	**b_0**	**b_1**	**b_2**	**b_3**
1	1.799650E-07	8.262126E-08	1.478349E-10	-7.021003E-13
2	-7.631685E-07	2.075943E-05	1.366995E-09	-2.719056E-11
3	2.870829E-03	1.166533E-03	-5.405968E-07	-7.064876E-09
4	8.535759E-03	2.105971E-03	-4.147420E-06	-4.753265E-09
5	2.535829E-01	1.675785E-03	-8.101588E-06	1.585619E-08
6	1.341521E-01	6.297658E-03	-4.677142E-05	1.251789E-07

Table B.3: New parameterization coefficients for solar g
Coefficients for the solar asymmetry factor parameterization, Equation [2.28].

	Aggregates			
#	**c_0**	**c_1**	**c_2**	**c_3**
1	7.605610E-01	9.870759E-05	-9.489491E-07	2.933044E-09
2	7.605314E-01	3.282699E-04	-3.081541E-06	9.495458E-09
3	7.565778E-01	1.209158E-03	-8.400393E-06	2.534937E-08
4	7.645339E-01	1.808754E-03	-1.267380E-05	3.613678E-08
5	8.486633E-01	1.852434E-03	-1.482007E-05	4.231379E-08
6	7.003525E-01	4.703117E-03	-3.478837E-05	9.046680E-08
	Bullet Rosettes			
#	**c_0**	**c_1**	**c_2**	**c_3**
1	7.315819E-01	4.140028E-03	-6.300760E-05	3.787902E-07
2	7.022171E-01	5.884385E-03	-9.298859E-05	5.566474E-07
3	7.067611E-01	5.833746E-03	-7.791993E-05	4.190400E-07
4	7.261233E-01	6.079660E-03	-8.282829E-05	4.534377E-07
5	8.237726E-01	4.924622E-03	-8.348968E-05	5.288946E-07
6	6.415427E-01	1.066267E-02	-1.634104E-04	9.865966E-07
	Hollow Hexagonal Columns			
#	**c_0**	**c_1**	**c_2**	**c_3**
1	8.007558E-01	1.560995E-04	6.232061E-06	-2.584035E-08
2	7.592446E-01	1.859092E-03	-1.440815E-05	5.804909E-08
3	7.671412E-01	1.773494E-03	-4.728381E-06	-5.704993E-09
4	7.856240E-01	2.021965E-03	-6.854855E-06	-4.401880E-09
5	8.690683E-01	1.759402E-03	-1.422714E-05	4.421788E-08
6	7.350087E-01	4.869509E-03	-3.951089E-05	1.113301E-07
	Hexagonal Plates			
#	**c_0**	**c_1**	**c_2**	**c_3**
1	7.542025E-01	6.842990E-03	-1.009599E-04	5.764375E-07
2	5.757408E-01	1.541660E-02	-2.446507E-04	1.396000E-06
3	6.119415E-01	1.092088E-02	-1.225276E-04	4.760237E-07
4	6.643511E-01	7.834623E-03	-5.948964E-05	6.938150E-08
5	8.080593E-01	5.255441E-03	-6.628331E-05	3.051311E-07
6	6.319924E-01	8.332237E-03	-6.635390E-05	1.373609E-07
	Solid Hexagonal Columns			
#	**c_0**	**c_1**	**c_2**	**c_3**
1	7.743151E-01	2.592777E-04	3.644844E-06	-1.376312E-08
2	6.906636E-01	2.887592E-03	-2.252208E-05	7.418582E-08
3	7.093217E-01	2.151442E-03	-5.403180E-06	-6.671247E-09
4	7.406592E-01	2.044261E-03	-3.846586E-06	-1.596443E-08
5	8.578058E-01	1.515721E-03	-9.128938E-06	1.946791E-08
6	6.945013E-01	4.893068E-03	-3.268974E-05	7.517560E-08

Table B.4: New parameterization coefficients for solar f_δ
Coefficients for the solar delta-function transmission parameterization, Equation [2.29].

	Aggregates			
#	**d_0**	**d_1**	**d_2**	**d_3**
1	1.666083E-04	5.415752E-06	-5.219050E-08	1.604002E-10
2	-1.385376E-05	9.018687E-06	-7.910603E-08	2.268507E-10
3	-5.891001E-05	8.115616E-06	-5.986653E-08	1.422914E-10
4	-6.835128E-05	7.965470E-06	-5.238227E-08	1.044092E-10
5	-4.776573E-05	5.049316E-06	-2.765683E-08	3.634069E-11
6	-2.180106E-05	1.783139E-06	-4.294116E-09	-8.527177E-12
	Bullet Rosettes			
#	**d_0**	**d_1**	**d_2**	**d_3**
1	2.192578E-02	4.641831E-03	-8.097206E-05	5.330901E-07
2	-3.956529E-02	7.204795E-03	-1.214432E-04	7.537812E-07
3	-3.421184E-02	4.776796E-03	-5.213578E-05	1.933049E-07
4	-2.576273E-02	3.354708E-03	-2.128794E-05	-2.954293E-08
5	-6.893736E-03	7.771527E-04	5.933413E-06	-1.188661E-07
6	-3.092551E-03	2.213534E-04	1.488863E-05	-1.801812E-07
	Hollow Hexagonal Columns			
#	**d_0**	**d_1**	**d_2**	**d_3**
1	6.680607E-02	3.527754E-04	-2.159458E-06	1.105072E-08
2	-2.849647E-02	3.508331E-03	-3.944695E-05	1.602200E-07
3	-1.984494E-02	1.832635E-03	-9.490264E-06	2.840097E-09
4	-1.137322E-02	8.986889E-04	3.322541E-06	-5.711139E-08
5	-2.373874E-03	1.463309E-04	4.373739E-06	-3.764774E-08
6	3.379599E-04	-5.075338E-05	2.678019E-06	-1.924303E-08
	Hexagonal Plates			
#	**d_0**	**d_1**	**d_2**	**d_3**
1	1.100062E-01	9.638038E-03	-1.381397E-04	7.843161E-07
2	-2.082869E-01	2.430592E-02	-3.789372E-04	2.138992E-06
3	-1.618716E-01	1.533958E-02	-1.392183E-04	3.331221E-07
4	-1.055549E-01	8.395499E-03	1.919593E-05	-7.568526E-07
5	-4.538848E-02	3.451841E-03	1.969677E-05	-4.446824E-07
6	-2.806875E-02	1.324095E-03	7.993434E-05	-9.337392E-07
	Solid Hexagonal Columns			
#	**d_0**	**d_1**	**d_2**	**d_3**
1	1.127613E-01	4.926724E-04	-2.915718E-06	1.265923E-08
2	-4.792108E-02	4.916534E-03	-4.653149E-05	1.584999E-07
3	-3.304531E-02	2.544802E-03	-1.143982E-05	5.385309E-09
4	-1.857399E-02	1.215074E-03	3.774286E-06	-5.328379E-08
5	-3.608024E-03	1.791787E-04	4.918597E-06	-3.445180E-08
6	6.047752E-04	-7.357206E-05	3.093613E-06	-1.835231E-08

Table B.5: New parameterization coefficients for infrared β_e*D_{ge}/IWC
Coefficients for the infrared extinction coefficient*D_{ge}/IWC parameterization, Equation [2.30].

	Aggregates		
#	**a_0**	**a_1**	**a_2**
7	-1.293637E-03	2.720978E+00	-2.593457E+00
8	-7.378176E-04	2.657056E+00	-4.261471E+00
9	-2.893095E-04	2.606376E+00	-4.953266E+00
10	1.681266E-04	2.546385E+00	-5.947297E+00
11	1.135199E-03	2.425672E+00	-7.345571E+00
12	3.183084E-03	2.128258E+00	-8.207944E+00
13	2.934800E-03	2.052180E+00	-5.281899E+00
14	4.146424E-04	2.478481E+00	-4.763979E+00
15	1.183598E-03	2.424293E+00	-7.303867E+00
16	3.306482E-03	2.145682E+00	-9.624768E+00
17	6.864574E-03	1.619715E+00	-9.149433E+00
18	6.394714E-03	1.675526E+00	-7.757332E+00
	Bullet Rosettes		
#	**a_0**	**a_1**	**a_2**
7	-7.568689E-03	3.034080E+00	-1.691345E+00
8	-6.635854E-03	2.993905E+00	-3.399125E+00
9	-4.868828E-03	2.906535E+00	-4.153586E+00
10	-4.101108E-03	2.884890E+00	-5.372456E+00
11	-1.317611E-03	2.739495E+00	-6.836966E+00
12	5.150726E-03	2.322403E+00	-7.551147E+00
13	6.124689E-03	2.191012E+00	-4.462595E+00
14	-2.716139E-03	2.859262E+00	-4.519703E+00
15	-1.833208E-03	2.867011E+00	-7.415873E+00
16	7.514887E-03	2.393408E+00	-9.565993E+00
17	2.063875E-02	1.445050E+00	-7.439283E+00
18	1.912470E-02	1.533661E+00	-6.020565E+00
	Hollow Hexagonal Columns		
#	**a_0**	**a_1**	**a_2**
7	-9.205483E-04	2.673497E+00	-7.994386E-01
8	-8.258682E-04	2.643240E+00	-1.772499E+00
9	-1.423913E-03	2.712784E+00	-2.680742E+00
10	-1.898341E-03	2.760329E+00	-3.534520E+00
11	-1.620908E-03	2.726754E+00	-5.019395E+00
12	5.556283E-04	2.504474E+00	-7.618618E+00
13	2.173974E-03	2.237230E+00	-4.905364E+00
14	-1.511701E-03	2.711549E+00	-3.092513E+00
15	-2.977585E-03	2.939231E+00	-5.965101E+00
16	-1.850785E-03	2.885482E+00	-1.106683E+01

Table B.5 continued

17	6.164482E-03	2.108110E+00	-1.269669E+01
18	5.870628E-03	2.076448E+00	-1.033761E+01
	Hexagonal Plates		
#	**a_0**	**a_1**	**a_2**
7	-4.200991E-03	2.939382E+00	8.717572E-01
8	-5.354830E-03	2.923979E+00	-4.113366E-01
9	-6.074562E-03	2.991459E+00	-1.769008E+00
10	-6.855174E-03	3.035276E+00	-3.062242E+00
11	-7.519880E-03	3.087922E+00	-6.212404E+00
12	-4.733934E-03	2.943107E+00	-1.095639E+01
13	2.659242E-03	2.356513E+00	-5.200637E+00
14	-4.983851E-03	2.992210E+00	-3.595466E+00
15	-8.747486E-03	3.419265E+00	-8.714011E+00
16	-9.067615E-03	3.528430E+00	-1.715925E+01
17	1.608027E-02	1.990152E+00	-1.336767E+01
18	1.238166E-02	1.868471E+00	-9.052213E+00
	Solid Hexagonal Columns		
#	**a_0**	**a_1**	**a_2**
7	-4.041682E-04	2.593521E+00	2.039653E+00
8	-1.701170E-03	2.762626E+00	2.765287E-01
9	-2.041594E-03	2.805616E+00	-8.891914E-01
10	-2.733232E-03	2.891649E+00	-1.843538E+00
11	-2.734130E-03	2.879859E+00	-3.847340E+00
12	-2.361952E-03	2.946585E+00	-9.533230E+00
13	8.012731E-04	2.507632E+00	-6.038515E+00
14	-2.284803E-03	2.918994E+00	-2.468737E+00
15	-4.311229E-03	3.173622E+00	-5.355440E+00
16	-3.965646E-03	3.244878E+00	-1.284285E+01
17	2.916403E-03	2.476800E+00	-1.673727E+01
18	3.684946E-03	2.399298E+00	-1.384673E+01

Table B.6: New parameterization coefficients for infrared β_a*D_{ge}/IWC
Coefficients for the infrared absorption coefficient*D_{ge}/IWC parameterization, Equation [2.31].

	Aggregates			
#	**b_0**	**b_1**	**b_2**	**b_3**
7	1.534300E-01	1.960628E-02	-1.642088E-04	4.895959E-07
8	2.992090E-01	1.900213E-02	-1.666460E-04	5.022892E-07
9	4.887941E-01	1.672285E-02	-1.538798E-04	4.719987E-07
10	3.772898E-01	1.876190E-02	-1.691380E-04	5.139852E-07
11	2.495955E-01	2.041179E-02	-1.788068E-04	5.365249E-07
12	2.436831E-01	2.058145E-02	-1.794992E-04	5.373076E-07
13	8.598906E-01	9.323346E-03	-9.069481E-05	2.844071E-07
14	9.698402E-01	8.248345E-03	-8.779303E-05	2.827773E-07
15	4.395911E-01	2.032924E-02	-1.910980E-04	5.853152E-07
16	6.701097E-02	2.124536E-02	-1.759886E-04	5.239212E-07
17	3.711234E-02	2.019544E-02	-1.617307E-04	4.792432E-07
18	3.803981E-01	2.224197E-02	-2.053680E-04	6.194111E-07
	Bullet Rosettes			
#	**b_0**	**b_1**	**b_2**	**b_3**
7	1.480938E-01	2.897019E-02	-3.833716E-04	2.107136E-06
8	2.961061E-01	3.206998E-02	-5.021289E-04	2.988480E-06
9	4.960929E-01	3.264699E-02	-5.969783E-04	3.816793E-06
10	3.692880E-01	3.511066E-02	-6.048956E-04	3.746628E-06
11	2.383568E-01	3.418346E-02	-5.261237E-04	3.081855E-06
12	2.328201E-01	3.452389E-02	-5.258605E-04	3.049352E-06
13	9.416914E-01	1.712845E-02	-3.836674E-04	2.703576E-06
14	1.070339E+00	1.647146E-02	-4.518323E-04	3.434313E-06
15	4.403512E-01	3.776799E-02	-7.318046E-04	4.809088E-06
16	6.004678E-02	3.049273E-02	-4.166467E-04	2.315483E-06
17	4.770149E-02	2.693333E-02	-3.191219E-04	1.628948E-06
18	3.488218E-01	4.422169E-02	-7.858849E-04	4.712176E-06
	Hollow Hexagonal Columns			
#	**b_0**	**b_1**	**b_2**	**b_3**
7	3.009813E-01	1.865557E-02	-1.687251E-04	5.616809E-07
8	4.871107E-01	1.770327E-02	-1.849032E-04	6.886114E-07
9	7.307478E-01	1.514304E-02	-1.877206E-04	7.790541E-07
10	6.050148E-01	1.773686E-02	-2.079421E-04	8.328959E-07
11	4.417594E-01	1.974756E-02	-2.095114E-04	7.846283E-07
12	4.258975E-01	1.973210E-02	-2.040300E-04	7.512679E-07
13	1.038338E+00	6.356741E-03	-9.079306E-05	4.027868E-07
14	1.240753E+00	3.362724E-03	-8.527572E-05	4.513195E-07
15	7.422814E-01	1.826486E-02	-2.467474E-04	1.058419E-06
16	2.093054E-01	2.145883E-02	-1.966154E-04	6.526304E-07

Table B.6 continued

17	1.416760E-01	2.074017E-02	-1.626140E-04	4.562539E-07
18	6.238514E-01	2.380054E-02	-2.995214E-04	1.210949E-06
	Hexagonal Plates			
#	**b_0**	**b_1**	**b_2**	**b_3**
7	2.423219E-01	2.328759E-02	-3.207025E-04	1.850895E-06
8	4.184272E-01	2.524025E-02	-3.896874E-04	2.307514E-06
9	6.591692E-01	2.361856E-02	-4.140701E-04	2.545631E-06
10	5.169974E-01	2.648419E-02	-4.376412E-04	2.634740E-06
11	3.536179E-01	2.711672E-02	-4.066715E-04	2.374554E-06
12	3.416532E-01	2.767777E-02	-4.086578E-04	2.358676E-06
13	1.068253E+00	8.203625E-03	-1.810340E-04	1.220874E-06
14	1.275178E+00	3.786838E-03	-1.722225E-04	1.391090E-06
15	6.556454E-01	2.584982E-02	-4.968130E-04	3.195100E-06
16	1.500865E-01	2.523224E-02	-3.661821E-04	2.103909E-06
17	8.457901E-02	2.519918E-02	-3.335658E-04	1.815249E-06
18	5.311048E-01	3.248218E-02	-6.046569E-04	3.739365E-06
	Solid Hexagonal Columns			
#	**b_0**	**b_1**	**b_2**	**b_3**
7	3.744155E-01	1.766150E-02	-1.395062E-04	3.937884E-07
8	5.981836E-01	1.719213E-02	-1.643031E-04	5.318323E-07
9	8.734564E-01	1.330341E-02	-1.527669E-04	5.517845E-07
10	7.258148E-01	1.641442E-02	-1.745009E-04	6.026929E-07
11	5.280428E-01	1.948111E-02	-1.847145E-04	5.910864E-07
12	5.063256E-01	1.991670E-02	-1.835622E-04	5.737566E-07
13	1.172751E+00	4.006231E-03	-5.778535E-05	2.274234E-07
14	1.404503E+00	6.603225E-04	-4.641584E-05	2.334732E-07
15	8.810097E-01	1.559426E-02	-1.871443E-04	6.849558E-07
16	2.641048E-01	2.030976E-02	-1.591513E-04	4.460374E-07
17	1.807304E-01	1.966696E-02	-1.295258E-04	3.010281E-07
18	7.337530E-01	2.087051E-02	-2.309565E-04	8.017940E-07

Table B.7: New parameterization coefficients for infrared g
Coefficients for the infrared asymmetry factor parameterization, Equation [2.32].

	Aggregates			
#	**c_0**	**c_1**	**c_2**	**c_3**
7	8.265107E-01	2.263326E-03	-1.704009E-05	4.977967E-08
8	8.562870E-01	2.443391E-03	-2.126668E-05	6.483441E-08
9	8.631608E-01	3.079702E-03	-3.021417E-05	9.582522E-08
10	8.399522E-01	3.323077E-03	-3.137873E-05	9.843080E-08
11	8.333067E-01	3.528244E-03	-3.375220E-05	1.074590E-07
12	8.383759E-01	4.144009E-03	-4.228161E-05	1.384028E-07
13	8.022425E-01	4.977005E-03	-5.114746E-05	1.664521E-07
14	7.530594E-01	5.175422E-03	-5.082812E-05	1.616137E-07
15	7.018285E-01	6.472677E-03	-6.134808E-05	1.910978E-07
16	6.770400E-01	5.969197E-03	-5.704225E-05	1.886926E-07
17	6.773402E-01	7.429877E-03	-7.695441E-05	2.612972E-07
18	5.151382E-01	1.247556E-02	-1.292331E-04	4.244470E-07
	Bullet Rosettes			
#	**c_0**	**c_1**	**c_2**	**c_3**
7	8.032536E-01	4.621815E-03	-5.306833E-05	2.238045E-07
8	8.362857E-01	4.199112E-03	-5.442889E-05	2.642287E-07
9	8.353498E-01	5.634188E-03	-9.509052E-05	5.779449E-07
10	8.183019E-01	6.031766E-03	-9.948567E-05	5.965949E-07
11	8.084744E-01	6.574012E-03	-1.127431E-04	7.004574E-07
12	8.043149E-01	8.761745E-03	-1.745068E-04	1.178950E-06
13	7.607785E-01	1.182337E-02	-2.495764E-04	1.723151E-06
14	7.222896E-01	1.109144E-02	-2.175497E-04	1.446316E-06
15	6.764131E-01	1.273467E-02	-2.306867E-04	1.449795E-06
16	6.165814E-01	1.569429E-02	-2.854521E-04	1.796214E-06
17	5.839195E-01	1.956868E-02	-4.101060E-04	2.886065E-06
18	3.679288E-01	3.129128E-02	-6.721142E-04	4.744234E-06
	Hollow Hexagonal Columns			
#	**c_0**	**c_1**	**c_2**	**c_3**
7	8.217759E-01	3.580815E-03	-2.493446E-05	5.255664E-08
8	8.504549E-01	3.072912E-03	-2.379315E-05	6.004303E-08
9	8.642977E-01	3.287383E-03	-3.333444E-05	1.172201E-07
10	8.540617E-01	3.204191E-03	-2.988942E-05	9.756683E-08
11	8.569081E-01	2.491725E-03	-1.868416E-05	4.768750E-08
12	8.707200E-01	2.748684E-03	-2.692513E-05	9.513721E-08
13	8.292041E-01	4.718213E-03	-6.058234E-05	2.573603E-07
14	7.674696E-01	5.397353E-03	-6.482212E-05	2.648967E-07
15	7.242883E-01	5.484790E-03	-5.375491E-05	1.908109E-07
16	6.949312E-01	4.714484E-03	-3.941364E-05	1.336775E-07

Table B.7 continued

17	6.368954E-01	9.759444E-03	-1.210186E-04	5.182662E-07
18	3.452861E-01	1.992342E-02	-2.527442E-04	1.065340E-06
	Hexagonal Plates			
#	**c_0**	**c_1**	**c_2**	**c_3**
7	8.127028E-01	6.853432E-03	-1.083208E-04	5.929700E-07
8	8.419558E-01	5.038405E-03	-7.286783E-05	3.772538E-07
9	8.507595E-01	5.525325E-03	-9.389450E-05	5.501883E-07
10	8.391590E-01	5.054627E-03	-7.777356E-05	4.291994E-07
11	8.381581E-01	4.052591E-03	-5.428066E-05	2.781099E-07
12	8.417921E-01	5.172227E-03	-8.497864E-05	5.106947E-07
13	7.806677E-01	9.145212E-03	-1.724684E-04	1.096348E-06
14	7.263531E-01	1.034104E-02	-1.924513E-04	1.216181E-06
15	6.693999E-01	1.327899E-02	-2.423163E-04	1.508734E-06
16	5.795446E-01	1.802198E-02	-3.242659E-04	1.984471E-06
17	4.348729E-01	2.990264E-02	-5.901442E-04	3.803312E-06
18	8.795077E-02	4.437856E-02	-8.349740E-04	5.220230E-06
	Solid Hexagonal Columns			
#	**c_0**	**c_1**	**c_2**	**c_3**
7	8.128817E-01	1.918632E-03	-2.619734E-06	-2.531058E-08
8	8.613810E-01	2.137302E-03	-1.131898E-05	1.560062E-08
9	8.678549E-01	2.510340E-03	-1.967660E-05	5.357800E-08
10	8.587726E-01	2.201709E-03	-1.400708E-05	2.980269E-08
11	8.644988E-01	1.994458E-03	-1.003892E-05	1.249054E-08
12	8.809782E-01	2.653673E-03	-2.282338E-05	6.936123E-08
13	8.345503E-01	4.256196E-03	-4.523797E-05	1.580488E-07
14	7.722910E-01	4.591317E-03	-4.432202E-05	1.458626E-07
15	7.327241E-01	4.261233E-03	-3.158921E-05	8.445554E-08
16	7.075600E-01	3.227147E-03	-1.848190E-05	4.479106E-08
17	6.551716E-01	7.164876E-03	-7.293056E-05	2.615894E-07
18	3.691749E-01	1.562536E-02	-1.633726E-04	5.707556E-07

Table B.8: New parameterization coefficients for infrared β_e*D_{ge}/IWC (small D_{ge})
Coefficients for the infrared extinction coefficient*D_{ge}/IWC small D_{ge} parameterization, Equation [2.41].

	Aggregates				
#	**a_0**	**a_1**	**a_2**	**a_3**	**a_4**
7	6.469875E-02	-3.057697E-01	5.232124E-01	-1.037409E-01	6.376345E-03
8	7.627549E-02	-2.381198E-01	3.690856E-01	-6.682283E-02	3.887997E-03
9	4.324341E-02	-6.786856E-02	2.455349E-01	-4.282174E-02	2.383504E-03
10	3.102296E-02	-4.090587E-02	1.593556E-01	-2.016710E-02	6.932228E-04
11	2.333213E-02	-2.499419E-02	8.875967E-02	-5.127519E-03	-2.449389E-04
12	4.930556E-03	3.944997E-02	3.180885E-02	3.592546E-04	-2.788977E-04
13	-9.286024E-03	3.520269E-01	-7.274820E-03	-3.454534E-03	3.003323E-04
14	1.264591E-02	2.161016E-01	1.042081E-01	-1.940316E-02	9.689492E-04
15	2.760038E-03	4.134939E-02	5.563913E-02	2.919921E-04	-5.061076E-04
16	9.121170E-03	-7.766481E-03	2.767237E-02	-7.080099E-04	2.255580E-05
17	1.651955E-02	-2.411636E-02	3.900749E-02	-8.828186E-03	7.425138E-04
18	-1.421853E-02	1.190404E-01	-1.138062E-02	3.213021E-03	-2.530014E-04
	Bullet Rosettes				
#	**a_0**	**a_1**	**a_2**	**a_3**	**a_4**
7	1.242067E-01	-4.842123E-01	6.357414E-01	-1.199619E-01	6.856390E-03
8	1.423865E-01	-3.523879E-01	4.240249E-01	-7.079470E-02	3.664414E-03
9	1.639874E-01	-2.934489E-01	3.645800E-01	-6.143685E-02	3.259034E-03
10	1.603113E-01	-2.799563E-01	2.847095E-01	-4.205805E-02	2.003892E-03
11	1.351001E-01	-2.124081E-01	1.865270E-01	-2.311644E-02	9.385282E-04
12	8.726870E-02	-8.319684E-02	9.176189E-02	-9.960515E-03	3.670594E-04
13	2.908693E-02	3.470572E-01	1.124950E-02	-7.329624E-03	5.206410E-04
14	1.558165E-01	5.754300E-02	1.859897E-01	-3.290555E-02	1.727270E-03
15	-8.021997E-03	6.076479E-02	4.003207E-02	5.305934E-03	-8.414903E-04
16	-3.974851E-02	8.159070E-02	-2.480224E-02	1.116955E-02	-8.059224E-04
17	-7.692082E-02	1.349879E-01	-4.524283E-02	9.298756E-03	-5.513401E-04
18	4.311318E-02	-5.510769E-02	8.987939E-02	-1.589605E-02	9.344843E-04
	Hollow Hexagonal Columns				
#	**a_0**	**a_1**	**a_2**	**a_3**	**a_4**
7	-1.132540E+00	1.365697E+00	-1.130846E-01	-3.268721E-03	4.533605E-04
8	-4.315446E-01	4.566379E-01	1.211749E-01	-2.548049E-02	1.166896E-03
9	-2.874577E-01	3.518437E-01	1.119412E-01	-2.105127E-02	9.162421E-04
10	-7.222310E-02	3.122336E-02	1.763075E-01	-2.502155E-02	9.764302E-04
11	6.542224E-02	-1.320104E-01	1.667290E-01	-1.965354E-02	6.824294E-04
12	4.250276E-02	-3.314132E-02	7.811359E-02	-7.713545E-03	2.285223E-04
13	-1.042575E-01	5.038297E-01	-5.108600E-02	2.572046E-03	-4.777565E-05
14	-2.411967E-01	5.137328E-01	2.468697E-02	-9.129782E-03	4.329424E-04
15	1.588274E-01	-2.312949E-01	1.896441E-01	-2.132922E-02	7.256643E-04

Table B.8 continued

16	1.029911E-01	-1.360514E-01	6.893791E-02	-3.668004E-03	2.374678E-05
17	1.975936E-02	2.237995E-03	8.874821E-03	5.093555E-04	-4.298247E-05
18	1.514836E-02	7.715978E-02	9.796194E-03	-5.938804E-04	6.804388E-06
	Hexagonal Plates				
#	**a_0**	**a_1**	**a_2**	**a_3**	**a_4**
7	-1.127529E+00	9.504466E-01	8.240995E-02	-2.900979E-02	1.534916E-03
8	-2.297126E-01	7.467164E-02	2.463470E-01	-3.883508E-02	1.662897E-03
9	-2.868449E-01	2.622984E-01	1.367226E-01	-2.257149E-02	9.537761E-04
10	-5.900577E-02	-1.974464E-02	1.768590E-01	-2.348347E-02	9.014719E-04
11	8.812986E-02	-1.629297E-01	1.634491E-01	-1.885750E-02	6.756577E-04
12	1.901987E-02	-1.009867E-02	6.493808E-02	-6.331025E-03	1.955486E-04
13	4.595223E-02	3.631884E-01	-8.177591E-03	-2.321035E-03	1.431648E-04
14	8.033438E-02	1.379964E-01	1.298030E-01	-2.004898E-02	8.377832E-04
15	4.395813E-01	-5.278725E-01	2.694624E-01	-3.019470E-02	1.084460E-03
16	1.784764E-01	-1.879675E-01	7.477630E-02	-4.206267E-03	4.457330E-05
17	6.545062E-02	-3.596376E-02	1.874863E-02	-8.417712E-04	1.405394E-05
18	1.827415E-01	-7.498675E-02	5.157593E-02	-5.287864E-03	1.872741E-04
	Solid Hexagonal Columns				
#	**a_0**	**a_1**	**a_2**	**a_3**	**a_4**
7	-1.483263E+00	1.551498E+00	-1.412163E-01	1.111984E-03	1.832367E-04
8	-7.017028E-01	6.595573E-01	5.115094E-02	-1.354676E-02	5.561368E-04
9	-5.251308E-01	5.408510E-01	4.913052E-02	-1.122417E-02	4.401915E-04
10	-1.967475E-01	1.536358E-01	1.218294E-01	-1.577917E-02	5.304168E-04
11	3.230758E-02	-9.554246E-02	1.393689E-01	-1.452933E-02	4.378071E-04
12	2.997171E-02	-1.639908E-02	6.595304E-02	-5.749358E-03	1.509691E-04
13	-1.342664E-01	4.964842E-01	-4.116585E-02	1.489549E-03	-1.440469E-05
14	-3.141379E-01	5.268969E-01	1.868050E-02	-6.614415E-03	2.689310E-04
15	1.887790E-01	-2.460398E-01	1.698286E-01	-1.654673E-02	4.844476E-04
16	1.786807E-01	-2.032762E-01	7.978103E-02	-4.718053E-03	7.744767E-05
17	4.116541E-02	-1.369014E-02	1.043230E-02	2.594552E-04	-2.658934E-05
18	-4.121045E-03	1.030819E-01	9.037553E-04	2.320732E-04	-1.493810E-05

Table B.9: New parameterization coefficients for infrared β_a*D_{ge}/IWC (small D_{ge})
Coefficients for the infrared absorption coefficient*D_{ge}/IWC small D_{ge} parameterization, Equation [2.42].

	Aggregates				
#	**b_0**	**b_1**	**b_2**	**b_3**	**b_4**
7	-1.602685E-02	6.570007E-02	-5.724589E-03	1.101320E-03	-8.560465E-05
8	-3.552493E-04	6.773349E-02	1.204737E-02	-2.995366E-03	1.988982E-04
9	3.441025E-03	1.104275E-01	1.295250E-02	-3.768580E-03	2.485324E-04
10	-6.298474E-03	9.703507E-02	3.407840E-03	-1.200199E-03	7.192650E-05
11	-3.783607E-03	6.820470E-02	7.311277E-04	9.637968E-05	-3.611345E-05
12	-6.145942E-03	7.223797E-02	9.980834E-04	-4.446681E-04	2.524819E-05
13	-1.776424E-02	3.910663E-01	-6.168932E-02	4.667395E-03	-1.024410E-04
14	-1.728951E-02	3.306355E-01	-1.972661E-02	-2.550455E-03	3.073026E-04
15	-9.870943E-03	8.585633E-02	1.623200E-02	-3.786677E-03	2.567597E-04
16	1.133064E-03	1.675804E-02	8.730253E-03	-1.506162E-03	9.572048E-05
17	6.334129E-03	4.237852E-03	1.457844E-02	-3.037803E-03	2.161393E-04
18	-1.658358E-02	1.212367E-01	-1.223459E-02	2.538410E-03	-2.071811E-04
	Bullet Rosettes				
#	**b_0**	**b_1**	**b_2**	**b_3**	**b_4**
7	-1.297832E-03	3.933000E-02	1.144333E-02	-2.343633E-03	1.391891E-04
8	4.801500E-05	6.787678E-02	1.634417E-02	-3.614090E-03	2.139192E-04
9	1.122412E-02	9.873854E-02	2.616032E-02	-6.154729E-03	3.754535E-04
10	9.736016E-04	8.323416E-02	1.458862E-02	-3.023333E-03	1.643655E-04
11	7.816664E-03	5.087272E-02	1.269382E-02	-2.088466E-03	9.770634E-05
12	2.432521E-02	3.835486E-02	1.731345E-02	-2.923434E-03	1.499114E-04
13	-1.048625E-02	4.390844E-01	-7.014208E-02	5.319668E-03	-1.377009E-04
14	1.871644E-02	3.483736E-01	-2.284902E-02	-1.477190E-03	1.875592E-04
15	-7.515963E-02	1.908058E-01	-3.272282E-02	6.003489E-03	-3.962792E-04
16	-3.143393E-02	6.686738E-02	-1.287426E-02	2.380922E-03	-1.439279E-04
17	-5.487251E-02	9.853284E-02	-2.636243E-02	4.362967E-03	-2.496565E-04
18	2.801684E-02	-3.107825E-02	7.982810E-02	-1.526242E-02	9.196504E-04
	Hollow Hexagonal Columns				
#	**b_0**	**b_1**	**b_2**	**b_3**	**b_4**
7	-1.954318E-02	6.999704E-02	-9.163239E-04	-1.704801E-04	8.346945E-06
8	-3.092843E-02	1.211056E-01	-4.990664E-03	-1.103570E-04	1.195076E-05
9	-5.280131E-02	1.973560E-01	-1.321401E-02	2.760025E-04	5.188601E-06
10	-3.538541E-02	1.364181E-01	-3.479643E-03	-3.797950E-04	2.193260E-05
11	-2.096620E-02	8.953423E-02	4.042880E-04	-4.359367E-04	1.857559E-05
12	-1.123512E-02	8.421445E-02	6.614136E-04	-4.258351E-04	1.759678E-05
13	-5.408944E-02	4.707746E-01	-7.822258E-02	6.098403E-03	-1.788911E-04
14	-1.598608E-01	5.157164E-01	-6.884231E-02	4.124068E-03	-9.089545E-05
15	-2.353759E-02	1.015265E-01	1.478872E-02	-2.442306E-03	9.509020E-05

Table B.9 continued

16	4.292796E-03	1.621104E-02	8.142006E-03	-7.872551E-04	2.395047E-05
17	9.436244E-04	2.553443E-02	2.597743E-03	-2.215101E-04	5.605690E-06
18	6.222572E-03	8.595253E-02	8.436051E-03	-1.246929E-03	4.401802E-05
	Hexagonal Plates				
#	**b_0**	**b_1**	**b_2**	**b_3**	**b_4**
7	-2.314091E-02	6.915031E-02	-7.655426E-04	-2.362221E-04	1.236416E-05
8	-1.491662E-02	9.937071E-02	6.281360E-04	-6.855357E-04	3.261604E-05
9	-5.987181E-02	2.039162E-01	-1.559937E-02	5.477688E-04	-4.893706E-06
10	-5.064456E-02	1.507026E-01	-8.815539E-03	2.445717E-04	-1.886868E-06
11	-2.506102E-02	8.874775E-02	5.826717E-04	-5.638533E-04	2.773677E-05
12	-2.995428E-02	1.003524E-01	-3.938966E-03	-2.099111E-05	6.846132E-06
13	1.012264E-01	3.489980E-01	-4.224628E-02	2.085979E-03	-2.846954E-05
14	4.346912E-02	3.069350E-01	-8.744626E-03	-2.382598E-03	1.495439E-04
15	7.920089E-02	-1.909534E-02	5.256964E-02	-6.987079E-03	2.774747E-04
16	2.409325E-02	-1.238961E-03	1.225943E-02	-1.254597E-03	4.194910E-05
17	2.333892E-02	6.385259E-03	7.666595E-03	-8.137357E-04	2.854021E-05
18	1.538023E-01	-4.902680E-02	4.547592E-02	-5.304991E-03	1.962611E-04
	Solid Hexagonal Columns				
#	**b_0**	**b_1**	**b_2**	**b_3**	**b_4**
7	-3.080952E-02	7.873839E-02	-2.863248E-03	6.743768E-05	-6.052928E-07
8	-6.007711E-02	1.389228E-01	-8.581973E-03	3.420432E-04	-6.006720E-06
9	-1.073102E-01	2.355672E-01	-2.058675E-02	1.023606E-03	-2.107476E-05
10	-5.815056E-02	1.531891E-01	-6.966574E-03	5.497565E-05	4.428850E-06
11	-2.791827E-02	9.328022E-02	-2.947087E-04	-2.964779E-04	1.198483E-05
12	-1.859692E-02	8.969497E-02	-4.960234E-04	-2.479087E-04	1.008513E-05
13	-5.818511E-02	4.481003E-01	-6.153582E-02	3.862748E-03	-9.047320E-05
14	-1.731229E-01	4.853304E-01	-5.165925E-02	2.258409E-03	-3.151807E-05
15	-1.865449E-02	9.199565E-02	1.473205E-02	-1.968271E-03	6.397612E-05
16	1.542239E-02	4.983399E-03	9.928624E-03	-8.386379E-04	2.245220E-05
17	8.193657E-03	2.030140E-02	3.003110E-03	-1.968456E-04	3.797989E-06
18	-1.645932E-02	1.121512E-01	-4.268048E-04	-2.154034E-04	6.613982E-06

Table B.10: New parameterization coefficients for infrared g (small D_{ge})
Coefficients for the infrared asymmetry factor small D_{ge} parameterization, [2.43].

	Aggregates				
#	**c_0**	**c_1**	**c_2**	**c_3**	**c_4**
7	-2.897524E-01	1.243719E+00	-5.188197E-01	9.362723E-02	-6.064771E-03
8	-2.467341E-01	1.129208E+00	-4.552424E-01	8.088956E-02	-5.192422E-03
9	-3.709556E-01	1.177537E+00	-4.525294E-01	7.761237E-02	-4.843930E-03
10	-1.004096E-01	6.064369E-01	-1.394967E-01	1.218884E-02	-2.110745E-04
11	-3.667504E-01	9.674771E-01	-3.211932E-01	4.896660E-02	-2.770571E-03
12	-2.865027E-01	6.806582E-01	-1.518392E-01	1.281209E-02	-1.832139E-04
13	-1.531511E-01	3.389655E-01	3.112390E-02	-2.391568E-02	2.313170E-03
14	-7.309168E-02	1.089638E-01	1.487542E-01	-4.650984E-02	3.784494E-03
15	4.382573E-02	-1.832980E-01	2.771443E-01	-6.815095E-02	5.045512E-03
16	4.784849E-02	-1.288551E-01	1.645955E-01	-3.310100E-02	2.029000E-03
17	-6.107929E-03	4.421833E-03	2.413717E-02	2.726745E-03	-6.658580E-04
18	-3.102148E-03	8.225736E-03	2.025611E-03	3.050175E-03	-3.186599E-04
	Bullet Rosettes				
#	**c_0**	**c_1**	**c_2**	**c_3**	**c_4**
7	1.470332E-01	5.184327E-01	-1.458266E-01	1.836846E-02	-8.789247E-04
8	-1.060699E-01	7.906262E-01	-2.564891E-01	3.757367E-02	-2.034753E-03
9	-3.603185E-01	1.064442E+00	-3.691656E-01	5.674866E-02	-3.162531E-03
10	-5.482622E-01	1.252024E+00	-4.475007E-01	7.028598E-02	-3.972470E-03
11	-6.587888E-01	1.330526E+00	-4.760676E-01	7.496755E-02	-4.245000E-03
12	-7.180249E-01	1.340650E+00	-4.728841E-01	7.383753E-02	-4.152001E-03
13	-7.336385E-01	1.212913E+00	-3.888747E-01	5.590903E-02	-2.928919E-03
14	-6.025091E-01	9.201989E-01	-2.464894E-01	2.983872E-02	-1.322589E-03
15	-3.616926E-01	4.664663E-01	-4.455583E-02	-4.848179E-03	7.200295E-04
16	8.581022E-02	-2.763081E-01	2.689528E-01	-5.603264E-02	3.577053E-03
17	1.798350E-01	-3.594028E-01	2.347437E-01	-4.028868E-02	2.201087E-03
18	-1.810452E-02	2.163589E-02	-4.149724E-03	5.122899E-03	-5.003441E-04
	Hollow Hexagonal Columns				
#	**c_0**	**c_1**	**c_2**	**c_3**	**c_4**
7	-3.066654E-01	8.103399E-01	-1.925154E-01	1.861769E-02	-6.286832E-04
8	-3.738609E-01	8.115386E-01	-1.839354E-01	1.728031E-02	-5.729649E-04
9	-4.312111E-01	7.936341E-01	-1.728384E-01	1.590765E-02	-5.210807E-04
10	-4.548161E-01	7.424648E-01	-1.524577E-01	1.346082E-02	-4.282512E-04
11	-4.416650E-01	6.652154E-01	-1.260465E-01	1.047077E-02	-3.180049E-04
12	-4.086811E-01	5.696842E-01	-9.494628E-02	7.036957E-03	-1.926126E-04
13	-3.230694E-01	4.092948E-01	-4.866504E-02	2.156480E-03	-1.875236E-05
14	-2.704597E-01	3.159042E-01	-2.371070E-02	-4.285059E-04	7.287613E-05
15	-1.341855E-01	1.231959E-01	2.735971E-02	-5.498706E-03	2.436588E-04
16	3.945386E-02	-8.642962E-02	7.367909E-02	-9.288650E-03	3.486239E-04

Table B.10 continued

17	5.735358E-02	-9.610566E-02	5.338498E-02	-5.446836E-03	1.720817E-04
18	1.342702E-02	-1.733102E-02	9.121119E-03	-1.513542E-04	-1.679064E-05
	Hexagonal Plates				
#	**c_0**	**c_1**	**c_2**	**c_3**	**c_4**
7	-3.828923E-01	7.815214E-01	-1.765660E-01	1.693472E-02	-5.828497E-04
8	-6.019036E-01	9.158628E-01	-2.065711E-01	1.998799E-02	-6.985339E-04
9	-7.196168E-01	9.567095E-01	-2.134079E-01	2.065758E-02	-7.240759E-04
10	-7.623652E-01	9.082534E-01	-1.922661E-01	1.796254E-02	-6.148980E-04
11	-6.997473E-01	7.653544E-01	-1.440679E-01	1.219048E-02	-3.843768E-04
12	-6.212021E-01	6.301607E-01	-1.015046E-01	7.322937E-03	-1.953511E-04
13	-3.593231E-01	3.132257E-01	-1.201563E-02	-2.388314E-03	1.681460E-04
14	-2.147943E-01	1.505099E-01	2.914056E-02	-6.522195E-03	3.142292E-04
15	-2.968447E-02	-5.269016E-02	7.927534E-02	-1.135253E-02	4.763920E-04
16	1.428219E-01	-1.945536E-01	9.329081E-02	-1.067197E-02	3.882935E-04
17	1.300378E-01	-1.500741E-01	5.712257E-02	-5.227623E-03	1.533541E-04
18	8.155680E-03	-7.280538E-03	2.403861E-03	6.257613E-04	-4.398688E-05
	Solid Hexagonal Columns				
#	**c_0**	**c_1**	**c_2**	**c_3**	**c_4**
7	-2.323335E-01	6.261244E-01	-1.220726E-01	9.675404E-03	-2.689580E-04
8	-3.671335E-01	6.798654E-01	-1.293357E-01	1.022139E-02	-2.853323E-04
9	-4.327353E-01	6.831374E-01	-1.267833E-01	9.896510E-03	-2.740682E-04
10	-4.287885E-01	6.239355E-01	-1.092096E-01	8.187940E-03	-2.205019E-04
11	-4.229517E-01	5.650839E-01	-9.191447E-02	6.531285E-03	-1.687907E-04
12	-3.971539E-01	4.905242E-01	-7.124631E-02	4.616883E-03	-1.102921E-04
13	-3.422543E-01	3.755421E-01	-4.265252E-02	2.058108E-03	-3.353554E-05
14	-2.958782E-01	3.045674E-01	-2.658863E-02	6.443280E-04	8.829261E-06
15	-1.814035E-01	1.590242E-01	6.121432E-03	-2.095206E-03	8.648653E-05
16	1.090539E-03	-3.270416E-02	4.421403E-02	-4.936104E-03	1.590976E-04
17	6.969791E-02	-9.156647E-02	4.250948E-02	-3.787625E-03	1.048168E-04
18	8.774616E-03	-1.031518E-02	5.949384E-03	-1.600970E-05	-1.200265E-05

Table B.11: Parameterization coefficients for AR

Coefficients for the mean effective aspect ratio parameterization, Equation [3.6].

	e_0	**e_1**	**e_2**	**e_3**
Fu Hex.	1.236816E+00	-1.524095E-02	9.918982E-05	-2.677644E-07
Aggr.	6.752900E-01	0.000000E+00	0.000000E+00	0.000000E+00
B. Ros.	1.119560E+00	-3.314140E-02	5.585801E-04	-3.570439E-06
H. Hex.	7.011092E-01	4.513991E-04	-6.852536E-05	3.063654E-07
Plates	7.051960E-01	1.965452E-01	5.764983E-04	-2.614669E-06
S. Hex.	7.011106E-01	3.763452E-04	-4.766206E-05	1.777195E-07